CORA Cork Open Research Archive
Cartlann Taighde Oscailte Chorcaí

Title	X-ray and optical studies of soft x-ray transients in M31
Authors	Nooraee, Nakisa
Publication date	2014
Original Citation	Nooraee, N. 2014. X-ray and optical studies of soft x-ray transients in M31. PhD Thesis, University College Cork.
Type of publication	Doctoral thesis
Rights	© 2014, Nakisa Nooraee - http://creativecommons.org/licenses/by-nc-nd/3.0/
Download date	2026-11-04 21:11:09
Item downloaded from	https://hdl.handle.net/10468/1514



UCC
University College Cork, Ireland
Coláiste na hOllscoile Corcaigh

X-ray And Optical Studies Of Soft X-Ray Transients In M31

A dissertation submitted to National University of Ireland, Cork

for the degree of Doctor of Philosophy

Nakisa Nooraee

Supervisor: Prof. Paul Callanan

Head of Department: Prof. John McInerney

February 2014



Department of Physics
University College Cork

School of Cosmic Physics
Dublin Institute for
Advanced Studies



Contents

Contents i

List of Figures viii

List of Tables x

List of Acronyms xi

I Basics 1

1 Introduction to X-Ray Binaries 2

1.1 Historical Notes 2

1.2 Basics of Stellar Evolution 4

1.3 X-Ray Binaries and Classifications 6

1.4 Radiation Processes in High Energy Astrophysics 17

1.4.1 Photoelectric absorption 19

2 Accretion Power 22

2.1 Standard Accretion Disc Model 23

2.1.1 Disc Black Body Models in XSPEC 29

2.2 Advection-Dominated Accretion Flow (ADAF) 31

2.3 The Emission States of Black Hole Binaries 34

3 Instrumentation & X-ray Data 43

3.1 X-Ray Telescopes 43

3.1.1 Chandra . . . 44
3.1.2 XMM-Newton . . . 46
3.1.3 Swift . . . 48
3.2 X-Ray Data . . . 48
3.2.1 X-ray data from Chandra . . . 50
3.2.2 X-ray data from XMM-Newton . . . 51
3.2.3 X-ray data from Swift (XRT) . . . 51
3.2.4 Pileup Effect . . . 52

II X-ray Transients in M31 54

4 Soft X-ray Transients in M31 and Optical Follow up 55
4.1 Estimating the X-Ray Position of an XRT in M31 . . . 57
4.2 Optical Analysis . . . 59
4.3 Estimating Orbital Period . . . 61
4.4 Study of a Very Bright SXT in M31 . . . 62
4.4.1 Discovery . . . 62
4.4.2 X-ray Observations with Chandra . . . 63
4.4.3 X-ray Observations with Swift . . . 63
4.4.4 Optical Observations with HST . . . 64
4.4.5 Results . . . 66
4.4.6 X-ray Light curve . . . 67
4.4.7 Orbital period Determination . . . 69
4.5 Period Distribution of SXTs in M31 . . . 70

5 The Light Curves of X-Ray Transients in M31 75
5.1 The Outburst of an Irradiated Disc . . . 78
5.2 Light Curve of Bright Transients in M31 . . . 81
5.3 Discussion . . . 85
Outburst Lightcurves . . . 85
Comparison with Theory . . . 87

6 Conclusion & Future Work 91

Appendices **95**

A Python Scripts for Analysing X-Ray Data **96**

A.1 Python - CIAO Script to Extract Spectrum 96

A.2 Python - SAS Script 98

A.2.1 Extract the Spectrum from PN Data 100

A.3 Python Script for SWIFT Data 102

A.3.1 Extract an Image 103

A.3.2 Extract Spectrum 104

B PyXspec script **108**

C Python-IRAF script **111**

Bibliography **114**

Declaration

I hereby declare that this thesis has not been submitted as an exercise for a degree at this or any other University and that, except where otherwise stated, it is entirely my own work.

I agree that the Library may lend or copy this thesis upon request.



Nakisa Nooraee

February 4, 2014.

Publications

Referred Papers

The results of research of my PhD have been published in 4 papers, listed below. The first paper, is totally my own idea and my research. I wrote and published this paper independently. I have been the first author in the second paper. I contributed partially in the X-ray study of the two last papers.

- **Nooraee, N.**
  Light Curves of Six Bright Soft X-ray Transients in M31. 2013 MNRAS 428, 205
- **Nooraee, N.**; Callanan, P. J.; Barnard, R.; Garcia, M. R.; Murray, S. S.; Moss, A. Chandra, Swift, and HST studies of the CXOM31 J004253.1+411422. Very bright X-ray transient in M 31. 2012A&A...542A.120N
- Barnard, R.; Galache, J. L.; Garcia, M.; **Nooraee, N.**; Callanan, P. J.; Zezas, A.; Murray, S. S. A period distribution of X-ray binaries observed in the central region of M31 with Chandra and HST. 2012ApJ...756...32B
- Barnard, R.; Garcia, M.; Murray, S.; **Nooraee, N.**; Pietsch, W.
  Observations of the recurrent M 31 transient XMMU J004215.8+411924 with Swift, Chandra, HST, and Einstein. 2011A&A...526A..50B

The Astronomer's Telegram

- **Nooraee, N.**; Callanan, P.; Garcia, M.Chandra detection of outburst from M31 binary CXOM31 J004321.1+411751. Atel #2294
- **Nooraee, N.**; Barnard, Robin; Pietsch, Wolfgang; Callanan, Paul; Garcia, Michael. Re-outburst of M31 source XMMU J004215.8+411924. Atel #2682
- Garcia, M.; Murray, S.; Primini, F.; Callanan, P.; **Nooraee, N.**
  Optical ID of CXOM31 J004253.1+411422, a bright Black Hole X-ray Nova in M31. Atel #2474

Acknowledgments

Before thanking people whose help brought this thesis to completion, I want to thank my Irish colleagues who made DIAS my home very far from my homeland. I would like to express my deepest gratitude to Phyllis Daly, Eileen Flood, Anne Grace and Patricia McDonald. They provided emotional support on very gray, rainy, depressing days in Dublin. Their efforts to improve my English are not forgotten, especially Eileen's help with my thesis.

I am profoundly thankful to my Irish friends Dr. Lisa Fallon and Dr. Grainne Costigan, for their friendship and all they thought me. What I have learned about Ireland and Irish culture would undoubtedly have been impossible without them.

Words in any language, be it English or my mother language, can not express my gratitude to Prof. Luke Drury. His inspiration far exceeded a supervisory role to me. When I was overwhelmed and about to quit, he was the one who faithfully told me you can.

I thank Dr. Robin Barnard and Dr. Patrik Kavangah for all of the helps they gave me in both software and physics. Also, I thank Prof. Paul Callanan for accepting the supervision of my thesis and allowing me to work within a collaboration with Dr. Micheal Garica in Harvard-Smithsonian center for astrophysics. I thank the internal and external referees who read and gave advices on my thesis.

At last, but not least, I want to thank my parents and Rostam, my spouse.

Summary

Soft X-ray transients (SXTs) are a subgroup of low-mass X-ray binaries consisting of a neutron star or a black hole and a companion low-mass star. SXTs exhibit a sudden outburst by increasing the luminosity from $\sim 10^{33}$ to $\sim 10^{36-38}$ergs^1. After spending a few months in outburst, SXTs switch back to quiescence. Optical study of the binary system during the quiescence state of SXTs provides an opportunity to discriminate between BH binaries and neutron star binaries. The first part ot this research is composed of result of 10 years joint project between Hubble space telescope and Chandra, to study SXTs in M31.

The other part of this thesis focused on the light curve of bright SXTs in M31. Disc irradiation is thought to be capable of explaining the global behaviour of the light curves of SXTs. Depending on the strength of the central X-ray emission in irradiating the disc, the light curve may exhibit an exponential or a linear decay. The model predicts that in brighter transients a transition from exponential decline to a linear one may be detectable. In this study, having excluded super-soft sources and hard X-ray transients, a sample of bright SXTs in M31 ($L_{peak} > 10^{38}$ergs^1) has been studied. The expected change in the shape of the decay function is only observed in two of the light curves from the six light curves in the sample. Also, a systematic correlation between the shape of the light curve and the X-ray luminosity has not been seen.

List of Figures

1.1 Stellar evolution paths 4

1.2 Evolutionary scenario for LMXB formation (taken from Tauris & van den Heuvel (2006)) 5

1.3 Evolutionary scenario for HMXB formation (taken from Tauris & van den Heuvel (2006)) 7

1.4 Coordinate configuration for the binary system 7

1.5 Equipotential contours of a binary system 8

1.6 The different accretion disc feeding mechanisms 9

1.7 Spatial distribution of Galactic LMXBs and HMXBs 10

1.8 Classification of X-ray binaries 11

1.9 Outburst (left panel) versus quiescence (right panel) in a dwarf nova 12

1.10 S-curve shape in temperature-Surface density plane 13

1.11 Light curve of a dwarf nova 14

1.12 Z and Atoll colour diagrams 15

1.13 Galactic black hole binaries 16

1.14 Light curve of A0620-00 18

1.15 Schematic illustration of the different radiation mechanisms. 19

1.16 Schematic illustration of photoelectric absorption 20

2.1 GRO J0422+32 in the hard state 32

2.2 The spectrum of V404 Cygni in quiescence 34

2.3 RXTE observation of BHB during thermal-dominant (HS) state 36

2.4 RXTE observation of BHBs during the hard state 37
2.5 Artist impression of BH and NS transient 38
2.6 Eddington-scaled luminosities versus orbital period 39
2.7 BHBs during steep power law emission state 40
2.8 Spectrum in the intermediate states 41
2.9 Configuration of the different spectral states in BHBs 42

3.1 Wolter type I mirror used in Chandra. 44
3.2 Configuration of ACIS/Chandra 46
3.3 Configuration of HRC/Chandra 47
3.4 Schematic configuration of Swift 48
3.5 Pileup caused the center of source rejected in ACIS observation. 52

4.1 A ROSAT map of M31 56
4.2 The X-ray and LGS images are displayed in DS9 58
4.3 Using IRAF to subtract the two HST images 60
4.4 The spectrum of r2-75 67
4.5 The X-ray light curve of r2-75. 68
4.6 Position of SXTs in M31 71
4.7 Period distribution of 12 SXTs in M31 73

5.1 Different morphological light curves types 77
5.2 X-ray Light curve of bright XRTs in M31 86

List of Tables

1.1 Comparison of LMXB and HMXB systems. 10

2.1 Summary of implemented various MCD models in XSPEC 31

3.1 General information of three X-ray telescopes which have been used in this thesis. 45

3.2 A summary of tasks for data processing. 51

4.1 Details of our Chandra ACIS-I and SWIFT observations. 62

4.2 The count rate per frame on the pileup map from each ACIS observation 63

4.3 Spectral fits and unabsorbed 0.2-10.0 keV luminosities of r2-75 65

4.4 Summary of transient sources in M31 72

5.1 List of the bright sources 82

5.2 Best fit results 90

List of Acronyms

ACIS	**A**dvanced CCD **I**maging **S**pectrometer
ADAF	**A**vdection **D**ominated **A**ccretion **F**low
ARF	**A**ncillary **R**esponse **F**ile
BH	**B**lack **H**ole
BHB	**B**lack **H**ole **B**inary
BHC	**B**lack **H**ole **C**andidate
BH XRB	**B**lack **H**ole **X**-**R**ay **B**inary
BH XRT	**B**lack **H**ole **X**-**R**ay **T**ransient
CV	**C**ataclysmic **V**ariable
DIM	**D**isk **I**nstability **M**odel
DN	**D**warf **N**ova
HST	**H**ubble **S**pace **T**elescope
HMXB	**H**igh **M**ass **X**-**R**ay **B**inary
ISCO	**I**nnermost **S**table **C**ircular **O**rbit
LMXB	**L**ow **M**ass **X**-**R**ay **B**inary
MCD	**M**ulti **C**olor **D**isk
NS	**N**eutron **S**tar
NS XRT	**N**eutron **S**tar **X**-**R**ay **T**ransient
PDS	**P**ower **D**ensity **S**pectra
QPO	**Q**uasi **P**eriodic **O**scillation

RMF	**R**esponse **M**atrix **F**ile
XRB	**X**-**R**ay **B**inary
XRT	**X**-**R**ay **T**ransient
XRN	**X**-**R**ay **N**ova
WD	**W**hite **D**warf

Part I

Basics

1

Introduction to X-Ray Binaries

About 90% of strong Galactic X-ray sources are binary systems, composed of a main-sequence star and a compact companion. The compact object can be a white dwarf, a neutron star or a black hole.

This Chapter starts with short historical notes in section 1.1. Stellar evolution is concisely reviewed in section 1.2. Section 1.3 is devoted to a review of the classification of **X-ray binaries (XRBs)**. In the last section, section 1.4, the physics of different radiation processes is briefly discussed.

1.1 Historical Notes

The year 2012 was the 50th anniversary of the birth of X-ray astronomy. In an attempt to detect X-ray emission from solar wind particles striking the lunar surface, Giacconi et al. (1962) discovered

the first extra-solar X-ray source, **Scorpius X-1 (Sco X-1)**. In the half a century since then, X-ray observations have opened up a new window in astronomy.

The story of XRBs started with the discovery of **Cygnus X-1**; two research groups, Webster & Murdin (1972) and Bolton (1972), independently discovered that the position of the X-ray source was coincident with the position of a radio source which was found to be the counterpart of a 9th magnitude O-type blue supergiant (called HDE 226868). The Doppler shift of the spectrum of HDE 226868 revealed that this source belonged to a binary system with a period of 5.6 days, despite the fact that the other member was invisible. From this information, the lower limit for the mass of the invisible member of the binary system is more than the maximum mass that a stable neutron star can have. Therefore, Cygnus X-1 was considered a strong candidate system for containing a black hole in a binary system and was the first demonstration that a binary system was involved in producing X-ray sources.

In addition, Giacconi et al. (1971) and Schreier et al. (1972) with the help of the Uhuru observations discovered the binary nature of **Centaurus X-3**. From the regular periodicity of 4.84 seconds in the X-ray flux, it became clear that there is a rotating neutron star in the binary system. From the Doppler shift of these X-ray pulses, the orbital period of the binary system was determined to be 2.09 days.

A large fraction of XRBs are X-ray transient sources. These sources suddenly brighten in the X-ray sky and after a few weeks/months fade away to quiescence. The first of these was detected on April 1967: During a rocket observation Harries & McCracken (1967) found a very bright source, named **Centaurus X-2**, that had not been detected previously. By the end of September 1967, the intensity of the source decreased by a factor of 50 and it was again undetectable (Francey & Fenton 1967). Two years later, in June 1969, a second transient source, **Centaurus X-4**, was discovered by Evans et al. (1970).

With the discovery of **A0620-00** (light curve is shown in Fig. 1.14), the story of transient sources became more interesting (Elvis et al. 1975). Observations of the optical counterpart, named V616 Mon, in quiescence indicated that the binary has an orbital period of 7.8 hours and that one binary member is a late-type star. McClintock & Remillard (1986) concluded that the mass of the compact object in the binary system must be $> 3.2 M_{\odot}$ (for an inclination angle of $\leq 90^{\circ}$) . This mass is above the upper limit for mass of a stable neutron star, so this transient system was assumed to contain a black hole. Finding more transients showed that a large fraction (17 from

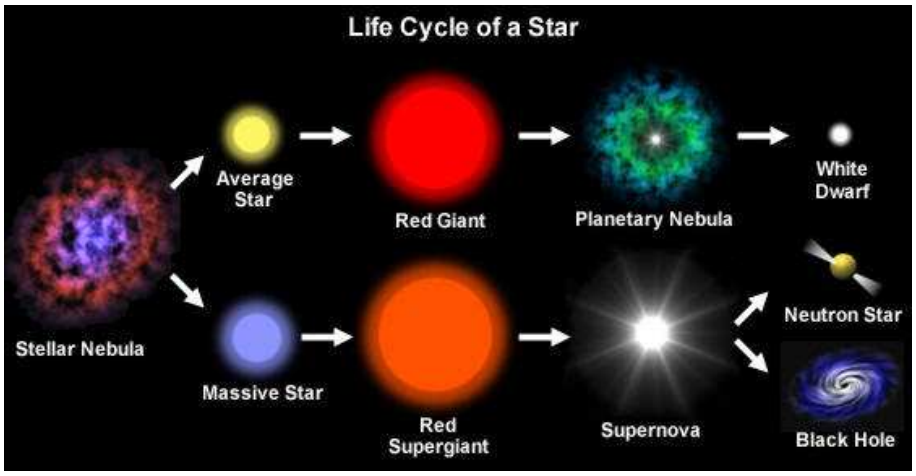


Figure 1.1: *Two different paths in stellar evolution.*

20) of black hole candidate systems are transient (Remillard & McClintock 2006b). Therefore, transient XRBs seem a promising place to look for black holes.

1.2 Basics of Stellar Evolution

The key determining factor for the end point of a star's life is its mass. Fig 1.1 [1] schematically shows the two different possible paths.

Once all the hydrogen fuel in the core of the star is exhausted and nuclear fusion stops in an average-mass star (0.6-10 $M_{\odot}$), the star contracts and heats up until fusion starts around the helium core. The star expands whilst the temperature of its photosphere reduces and it appears as a red giant. Once hydrogen fusion in the shell has ended, the star contracts again and the helium nuclei fuse to form carbon. Since the mass of the star is not sufficient to shrink the core to achieve the temperature needed for carbon fusion, the star throws off its outer atmospheric layers to form a planetary nebula. The remains of the stellar core is a White Dwarf (WD).

The Chandrasekhar limit, named after S. Chandrasekhar in honour of his discovery in 1930, determines the maximum mass for a stable WD. In a stable star, two forces must be in balance: gravity and pressure. Chandrasekhar noticed in a WD that the electron degeneracy pressure is the main force resisting gravitational collapse, but that this is only effective as long as the electrons remain non-relativistic. His calculations showed that 1.44 $M_{\odot}$ (=2.86×10^{30} kg) is the mass of the most massive WD.

More massive stars travel a different path becoming red supergiants. For these stars fusion in

[1] Taken from http://www.seasky.org/celestial-objects/stars.html

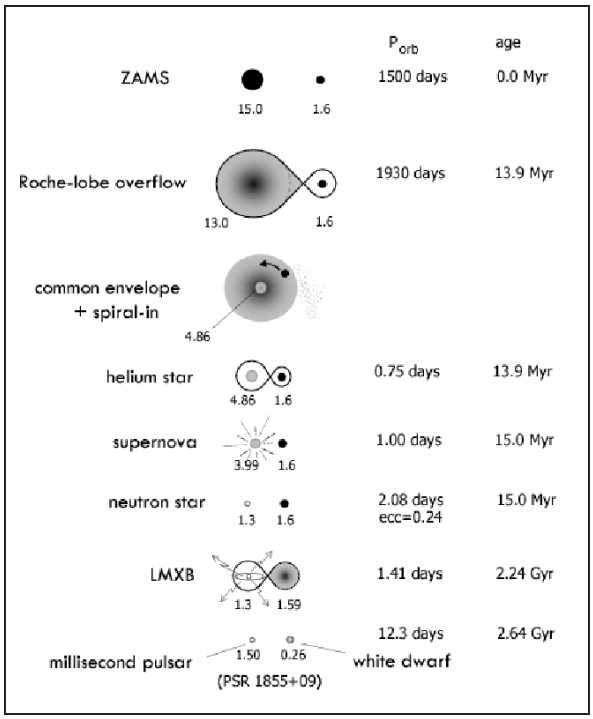


Figure 1.2: *Evolutionary scenario for LMXB formation (taken from Tauris & van den Heuvel (2006))*

the core continues up to iron. Fusion of lighter elements than iron releases energy while fusion of heavier elements requires energy. Therefore the fusion chain stops at iron and gravity causes the star to collapse. The core collapse of a massive star is called a type II supernova. This supernova can produce a neutron star or a black hole.

In a Neutron Star (NS), the electron repulsive force is not sufficient to resist the pressure of gravity. The electrons are pushed into the atomic nuclei and neutrons are produced. This allows a neutron star to stabilize by balancing the force due to gravity and neutron degeneracy pressure.

A Black Hole (BH) forms when the mass of the collapsed star is $>3M_{\odot}$. In this case, the force of gravity is stronger than even neutron degeneracy pressure. Thus, the dominant force is gravity and the remnant collapses and forms a BH. The space-time around a BH is dominated by an extreme gravitational field within the event horizon. The event horizon is the border around the black hole from which no particle can escape, not even a photon.

Stellar evolution in a binary system depends on the mass of stars and the distance between them. Here we are interested in the stellar evolution of a close binary system, in which the stars are close enough to allow matter to be transferred from one to the other. Kippenhahn & Weigert (1967) classified three cases of mass transfer based on the nuclear evolutionary state of the star: case A (the star is on the main sequence burning hydrogen), case B (the star has finished hydrogen

burning, but helium is still burning in the core) and case C (the star has completed the helium burning in the core). Also, mass transfer in a binary system can be stable or unstable, depending on the mass ratio of the system. For example, if the mass of the accretor is less than that of the mass losing star, the conservation of angular momentum implies that the stars will be driven closer together, and mass transfer occurs in a dynamically unstable way.

The evolutionary scenario for the formation of X-ray binaries with a low mass companion, or secondary star (called Low Mass X-ray binary, or LMXB) is shown in Fig. 1.2. As will be explained later in more detail (see page 7), the more massive star fills its Roche lobe first and the system enters a common envelope phase, resulting in a binary with an orbital period of 1 day. The more massive star then becomes a supernova, resulting in an LMXB where mass transfer between the stars occurs via an accretion disk.

The formation of X-ray binaries with more massive secondary stars (the so called High Mass X-ray Binaries, or HMXBs) is different (see Fig. 1.3). Initially, the heavier star evolves first and becomes a giant, and transfers matter to its companion via Roche lobe overflow. Most of its mass is transferred in this way, and the remaining star undergoes a supernova explosion, leaving a neutron star remnant. This results in a neutron star orbiting a massive star in a moderately eccentric orbit. As the orbital period decreases to a few years, mass transfer via a stellar wind onto the neutron star creates a HMXB. These binaries do not last for very long. Soon a common envelope with the neutron star forms and the orbital period shrinks to a few hours. Eventually a second supernova event occurs, leaving a pair of neutron stars (an example being the Hulse-Taylor pulsar system PSR B1913+16).

A detailed classification scheme for all types of X-ray binary (and related systems) is discussed in more detail in section 1.3.

1.3 X-Ray Binaries and Classifications

To describe a binary system, consider two spheres with masses M_1 and M_2, located on the x-axis and separated by a distance a, as shown in Fig. 1.4. The center of mass is at $\mathbf{X}_{cm}$. The force, $\mathbf{F}$, acting on a test mass particle with mass m, located at r can be formulated as

$$\mathbf{F} = -m\boldsymbol{\nabla}\Phi_R,$$

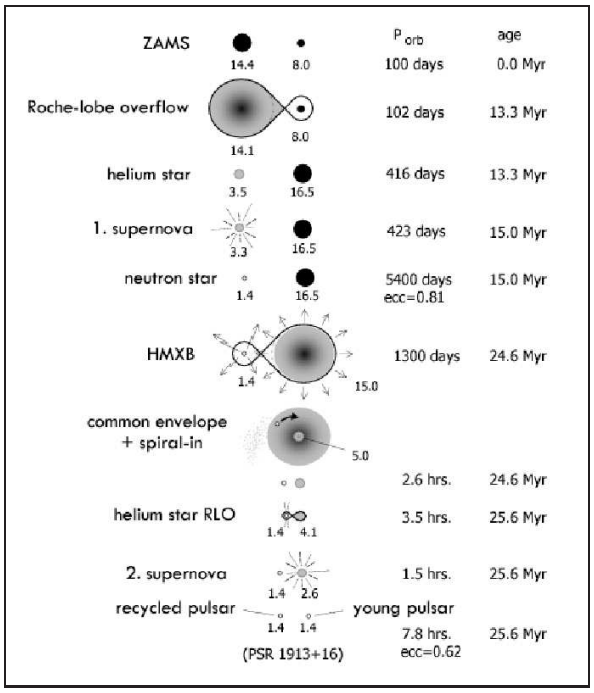


Figure 1.3: *Evolutionary scenario for HMXB formation (taken from Tauris & van den Heuvel (2006))*

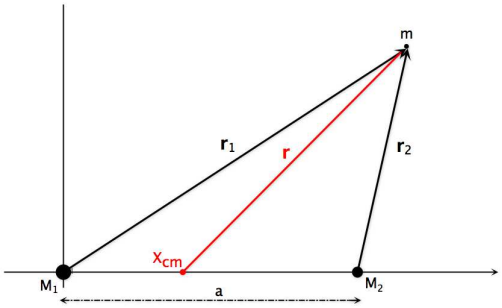


Figure 1.4: *Coordinate configuration for the binary system.*

where Φ_R is the Roche potential and equal to

$$\Phi_R(\mathbf{r}) = -\frac{GM_1}{|\mathbf{r}-\mathbf{r}_1|} - \frac{GM_2}{|\mathbf{r}-\mathbf{r}_2|} - \frac{1}{2}(\boldsymbol{\omega}\times(\mathbf{r}-\mathbf{X}_{\rm cm}))^2. \tag{1.1}$$

The test mass is at rest in the rotating frame. Therefore, the centrifugal force (the last term in Eq. 1.1) vanishes.

As shown in Fig. 1.5 [2], the Roche equipotential contours close to each of the masses are approximately spherical. An important equipotential is the one which includes the inner Lagrangian point, L_1. This point is a saddle point of the curve where, by definition, $\frac{\partial\Phi}{\partial x} = \frac{\partial\Phi}{\partial y} = 0$. If one of the stars (called the secondary star) expands and fills its Roche lobe, any particle which passes

[2]Taken from https://www.e-education.psu.edu/astro801/content/l6_p6.html

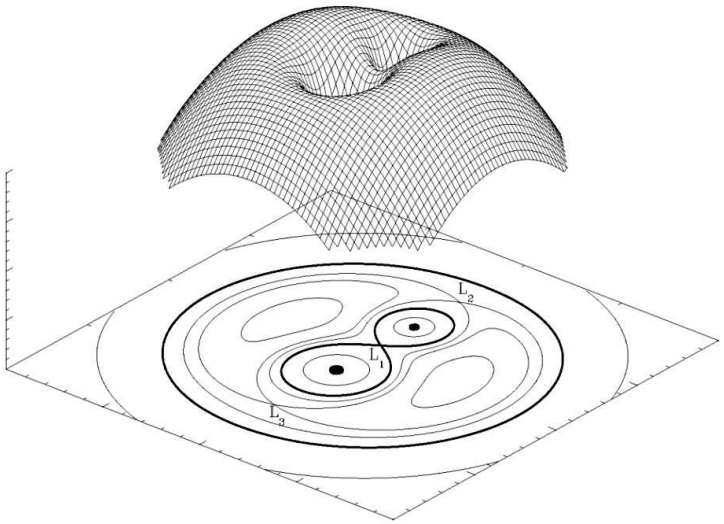


Figure 1.5: *Equipotential contours of a binary system and Lagrangian points.*

through L_1 will move in the direction of decreasing values of Φ_R. In other words, the particles will be under the gravitational field of the other star (known as the primary). This mechanism is called Roche-lobe overflow.

The matter which flows through L_1 possesses angular momentum, and hence does not directly fall on the primary. Instead, it starts to rotate in a Keplerian orbit around the primary star with velocity

$$\mathrm{v_k} = \sqrt{\frac{GM}{r}} \tag{1.2}$$

where r is the distance between the particle and the center of the primary star. This material forms a disc around the star. The disc is called an accretion disc and the primary star is alternatively recognized as the accretor.

Orbiting in the accretion disc, the viscosity between the adjacent layers dissipates the kinetic energy of the particle. Therefore, the particle moves in a circle of gradually decreasing radius. Assuming an accretor with mass M and radius R, the difference in the gravitational potential energy for a test particle with mass m moving from infinity to the surface of the accretor is

$$\triangle E_{\mathrm{GR}} = \frac{GMm}{R} \tag{1.3}$$

So if the matter falls through the disc with a constant rate of $\dot{M}$, the amount of the matter accreted during time Δt is $\dot{M}\Delta t$. Thus, the total gravitational potential difference is $G\frac{M\Delta M}{R}$. Due to this

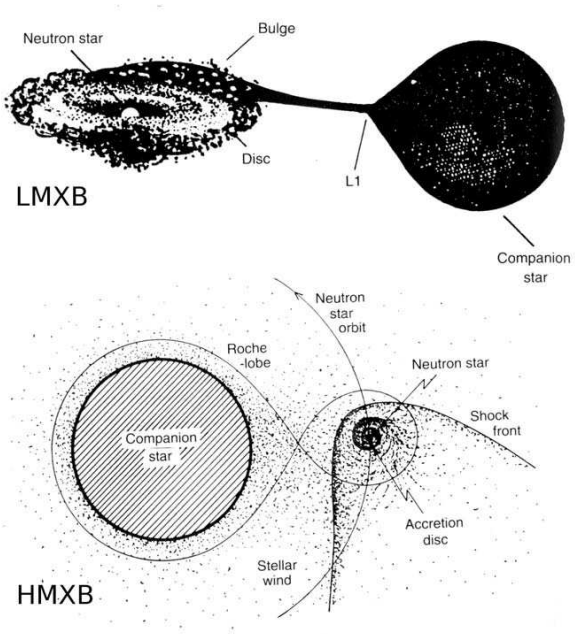


Figure 1.6: *Accretion feeding mechanisms in LMXB versus HMXB (Seward & Charles 2010).*

fact, the accretion luminosity is

$$L_{\rm acc} = \frac{\Delta E_{\rm grav}}{\Delta t} = \frac{GM\Delta M}{R\Delta t} = \frac{GM\dot{M}}{R}.$$

Taking into account the fact that all of the gravitational potential will not be radiated away immediately, and introducing a dimensionless efficiency factor, $\eta_{\rm acc}$, the luminosity of the accretion disc can be written as

$$L_{\rm acc} = \eta_{\rm acc}\frac{GM\dot{M}}{R} \tag{1.4}$$

The Roche lobe over-flow mechanism explained above is responsible for X-ray emission from binary systems known as **Low Mass X-ray Binaries (LMXBs)**. Accretion will be discussed in more detail in Chapter 2. LMXBs are a subgroup of compact binary systems where the binary is composed of a compact object and a low mass main-sequence companion star ($< 1M_{\odot}$).

In the case where the companion in the compact binary is more massive (O or B star), the binary is called a **High Mass X-ray Binary (HMXB)**. The accretion disc in a HMXB is fed by stellar winds. Fig. 1.6 illustrates the two different mechanisms which feed the accretion discs in HMXB (stellar wind) and LMXB (Roche lobe overflow).

The energy generated due to the accretion of matter onto an object cannot be infinite. The luminosity of the accretor exerts radiation pressure on the accreted material. The radiation energy

	LMXB	HMXB
Companion Star	M$\leq 1M_{\odot}$	- M $> 10M_{\odot}$
Lifetime	$\sim 10^7 - 10^9$	$\sim 10^5 - 10^7$yr
Accretion Process	Roche-lobe overflow	wind/atmospheric Roche-lobe flow
Orbital Period	11.4 m -33.5 days	0.2-580 days
Spatial Distribution	Galactic center/globular clusters	Galactic center/plane & young stellar population

Table 1.1: *Comparison of LMXB and HMXB systems.*

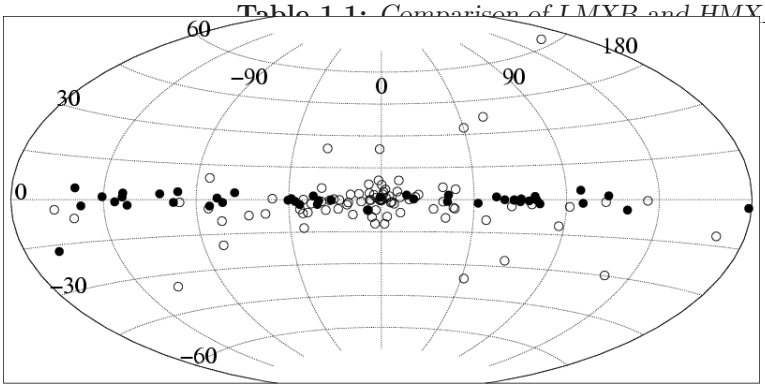


Figure 1.7: *Spatial distribution of LMXBs (open circles) and HMXBs (filled circles) within the Galaxy (Grimm et al. 2002).*

flux on the surface dA at distance r from a source with luminosity L is

$$\frac{dE}{dt\,dA} = \frac{L}{4\pi r^2}.$$

The momentum of a photon with energy E is $p = \dfrac{E}{c}$. Therefore, the momentum flux is given by

$$\frac{dp}{dtdA} = \frac{L}{4\pi c r^2}.$$

The radiation force on a free electron is given by

$$F_{\rm rad} = \sigma_T \frac{L}{4\pi r^2 c}, \tag{1.5}$$

where σ_T is Thomson scattering cross-section. Now, the gas is assumed to be neutral, with the electron and proton bound by the Coulomb force. The gravitational force on a proton is given by

$$F_{\rm grv} = \frac{GMm_{\rm p}}{r^2} \tag{1.6}$$

where M is the mass of the accretor (the mass of electron is negligible compared to the mass of proton). At the luminosity threshold, $L_{\rm Edd}$, the two forces balance and from Eq. 1.5 and 1.6, one

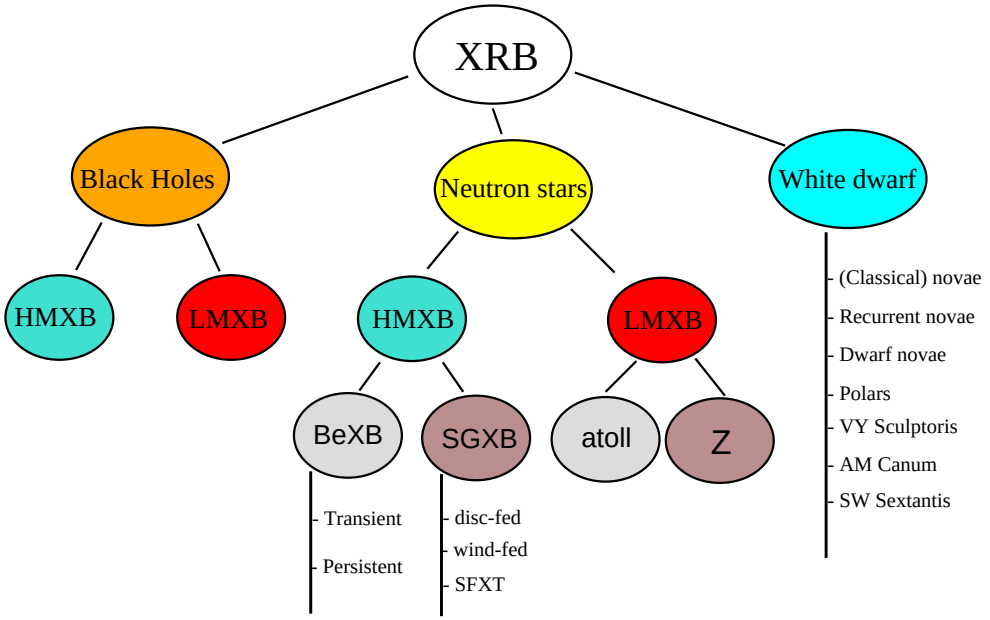


Figure 1.8: *Classification of XRBs versus on the compact component (from Reig (2011)).*

can derive the Eddington luminosity, $L_{\rm Edd}$, as

$$\mathrm{L_{Edd}} = 4\pi \mathrm{G}\frac{\mathrm{M m_p c}}{\sigma_\mathrm{T}} = 1.3 \times 10^{38}(\frac{\mathrm{M}}{\mathrm{M_\odot}})\mathrm{erg\,s^{-1}} \tag{1.7}$$

Even though calculations of $L_{\rm Edd}$ are based on many assumptions (e.g. symmetrical accretor, steady states, free electrons) and the luminosity is only a rough estimate, this limit provides astronomers with a useful upper limit to the luminosity of an accreting object.

The type and mass of the companion star determines the evolution and therefore the lifetime of the XRB: LMXBs have longer lifetimes ($\sim 10^7 - 10^9$ yr) than HMXBs ($\sim 10^5 - 10^7$yr). The spatial distribution of each type of binary system can be understood in terms of the lifetime, LMXBs are more likely to be found in the Galactic center and globular clusters, whereas HMXB are mostly found in the Galactic center, the Galactic plane and in young stellar populations (see Fig.1.7) (Grimm et al. 2002). Table 1.1 summarizes and compares the main differences between the two main types of XRBs.

The XRBs subdivide into another classification system which is based on the type of compact object. Fig. 1.8 depicts these subdivisions.

An interacting binary system is called a **Cataclysmic Variable (CV)** when the compact object is a white dwarf. Strong X-ray and UV emission has been observed from the accretion

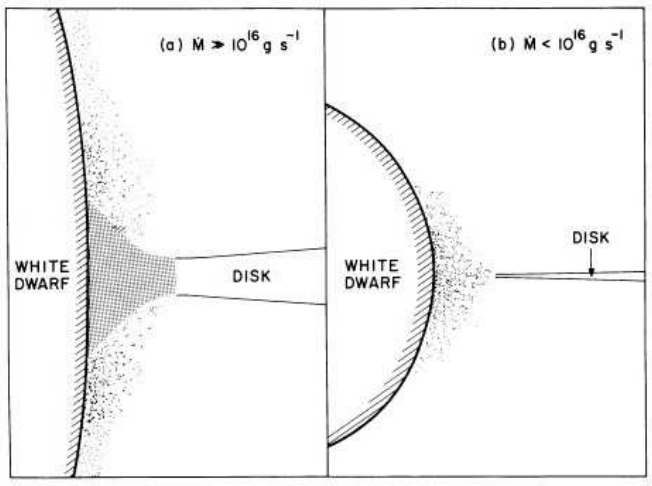


Figure 1.9: *Outburst versus quiescence in a dwarf nova (adapted from Patterson & Raymond (1985)).*

discs in CVs. Among the numerous subgroups of CV systems, a group called **Dwarf Novae (DNe)** undergo outbursts similar to those observed from X-ray transients (described earlier). The luminosity of DNe increases suddenly, sometimes in just a few hours, and outbursts can last from a few days to weeks. After the outburst, they return to quiescence.

Two theories have been proposed to explain the mechanism which governs the outburst: the mass transfer instability (MTI) and the disk instability model (DIM). The MTI model assumed that instabilities in the mass transfer rate from the secondary cause an outburst, but it proved difficult to identify a physical mechanism to generate the required instability. The DIM, on the other hand, proposes that an instability in the accretion disk caused an outburst and the subsequent return to quiescence. This model has become widely accepted. The DIM is usually described by a S-curve shape diagram in the surface density-disc temperature (T-Σ) plane . In a DN binary system, the disc is stable while the system is in quiescence (near point A in Fig. 1.10). The accumulation of accreted matter from the donor star in the disc increases the surface density of disc and correspondingly its temperature (point B). Increasing the temperature causes hydrogen to be ionized and therefore the disc becomes unstable. Outbursts start when the hydrogen atoms in the disc are fully ionized (point C). A new stability is established in the disc which corresponds to the upper branch of S-curve. However, because the rate of matter resupplied from the donor star is smaller than the rate of matter lost from the accretion disc to the accretor, this stability does not last long, the temperature and the surface density decrease and the disc which is half ionized becomes unstable (point D) and subsequently goes back to quiescence.

The sudden and huge increase in the X-ray luminosity is due to a change in the mass accretion

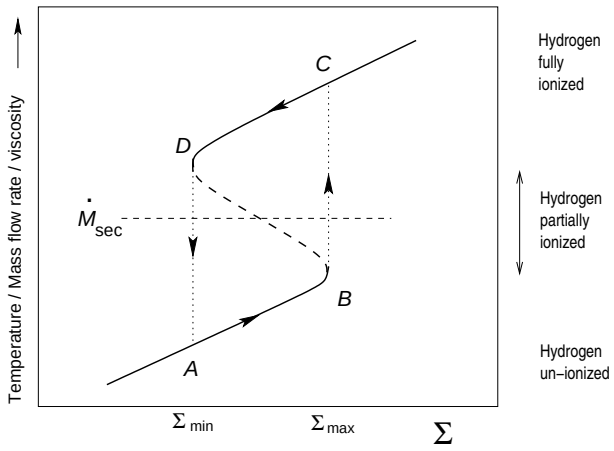


Figure 1.10: *S-curve shape in temperature-surface density (T-Σ) plane (adapted from Hellier (2001)).*

rate onto the compact object, as shown schematically in Fig.1.9. During the vast change in the rate of accretion (right panel of the figure), the X-ray luminosity increases by a factor of 100 and the visual magnitude by 2-5 mag. After spending a few days in outburst, the luminosity decays within a week and returns to quiescence as the mass accretion rate decreases noticeably. The most studied DN over a long period is SS Cygni which undergoes quasi-regular outbursts. The light curve is shown in Fig. 1.11.

Another group of white dwarf accreting binaries are the **Super Soft X-ray Sources (SSSs)** which were initially thought to contain a neutron star or a black hole due to the fact that they exhibit a very high luminosity in the X-ray sky ($\sim 10^{36-38}\mathrm{erg\,s^{-1}}$). Most of SSS sources have been detected in M31 and SMC. Due to high Galactic interstellar absorption these sources are expected to be observed at high Galactic latitudes only. Considering their extremely low temperature ($\mathrm{kT}\sim 10-75$ eV), van den Heuvel et al. (1992) showed that the size of accretor is only consistent with the size of white dwarf.

As we have seen, a compact binary with a neutron star as its compact object can be either a LMXB or a HMXB, depending on the mass of the companion. Depending on the luminosity class of the donor star, HMXBs consisting of a neutron star are divided into **Be X-ray Binaries (BeXBs)**, when the companion is of luminosity class III, IV or V, or **Super Giant XRBs (SGXBs)** if the system contains a star of luminosity class I-II. (The list of Roman numbers indicating the luminosity class are as follows. class I: supergiants, class II: blue giants, class III: giants, class IV: subgiants, class V: dwarf(main sequence stars), class VI:subdwarfs, class VII: white dwarfs). Though it has been believed that the accretion discs in HMXBs are fed by stellar winds, three SGXBs have been discovered which do not agree with this: Cen X-3, SMC X-1 and

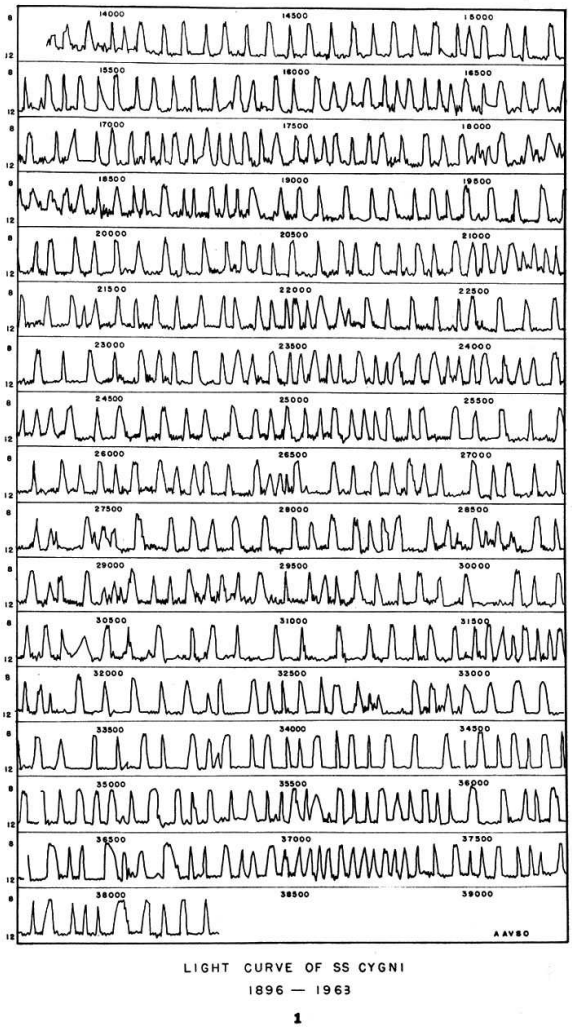


Figure 1.11: *Light curve of SS Cygni, a dwarf nova (Mattei et al. 1985)*

LMC X-4 are HMXBs with Roche lobe fed discs. Most BeXBs are transient while most SGXBs are persistent. An improvement in the sensitivity of the X-ray detectors was needed to discover more SGXBs. Before the launch of INTEGRAL in 2002, the rate of discovery was approximately four BeXBs for one SGXB (Reig 2011). INTEGRAL also revealed a subgroup of this category with a bright outburst that lasts for a few hours and a peak luminosity of $10^{36} - 10^{37}\mathrm{erg\,s^{-1}}$. This group is known as **Supergiant Fast X-ray Transients (SFXT)**.

LMXBs with a neutron star are placed in the subclasses as atoll and Z type, based on the shape of their X-ray colour-colour diagram. A sample is shown in Fig. 1.12.

The main characteristic which differentiates a neutron star from a black hole is that a neutron star has a physical surface while a black hole does not. Accumulating the accreted hydrogen on the surface of a neutron star can initiate a thermal instability which results in a sudden and short

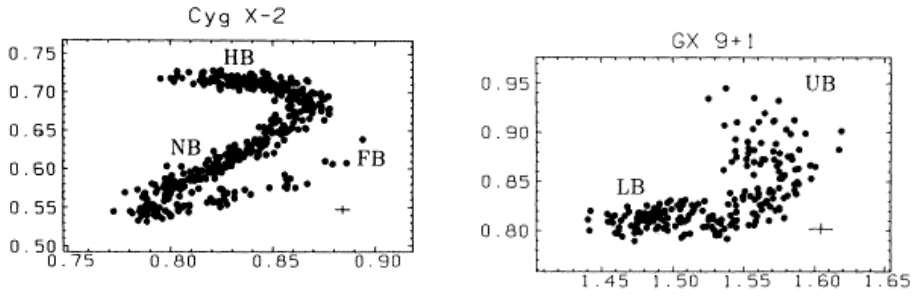


Figure 1.12: *Colour-colour diagram of Z source (left panel) and Atoll (right panel) (Hasinger & van der Klis 1989).*

outburst that lasts 10-100 seconds in X-ray band, known as an X-ray burst or more accurately a type I X-ray burst (Type II bursts happen as the result of a sudden increase in the rate of accretion onto the compact star. Its profile shows a sudden start and abrupt stop with no gradual decay from the peak).

The Schwarzschild radius of an object ($R_{\rm sch} = \frac{2GM}{c^2}$) confines the space around the object where theoretically any matter inside becomes a black hole. In other words, the Schwarzschild radius is the event horizon of a non-rotating black hole. Since the radius of a nominal neutron star (M = 1.4 $M_\odot$ and R = 10 km) is ~ 2.5 times its Schwarzschild radius, the accretion onto a neutron star cannot easily be distinguished from the accretion onto a black hole of comparable mass. The compactness (i.e.$\frac{M}{R}$) of a typical neutron star is 0.14 $\frac{M_\odot}{\rm km}$, whereas the compactness parameter for a nominal black hole (M $\sim$ 10 $M_\odot$ and R= $R_{\rm sch}$ $\sim$ 30 km) is 0.3 $\frac{M_\odot}{\rm km}$. Therefore, not finding evidence of a neutron star in a binary system does not necessarily prove that the binary hosts a black hole. For instance, it was thought that some X-ray characteristics, for example very soft spectra and fast variability could be used to reliably determine the nature of the binary system. Counterexamples were soon found, however, showing that just the X-ray spectrum cannot be used to prove the existence of a black hole in an XRB. For example Cir X-1, which has a very soft X-ray spectrum, was considered first to be a black hole binary (Samimi et al. 1979), but detection of type I X-ray outburst demonstrated this system could not contain a black hole (Tennant et al. 1986). Another counterexample is X 0331+53 which exhibited fast erratic variability (Terrell et al. 1983) and was assumed to be a BHB, but the subsequent detection of coherent pulsations with a period of 4.4 s classified it instead as a neutron star XRB (Stella et al. 1985). The term black hole candidate (BHC) comes from the uncertainty caused by classifying the compact object based on its X-ray properties alone.

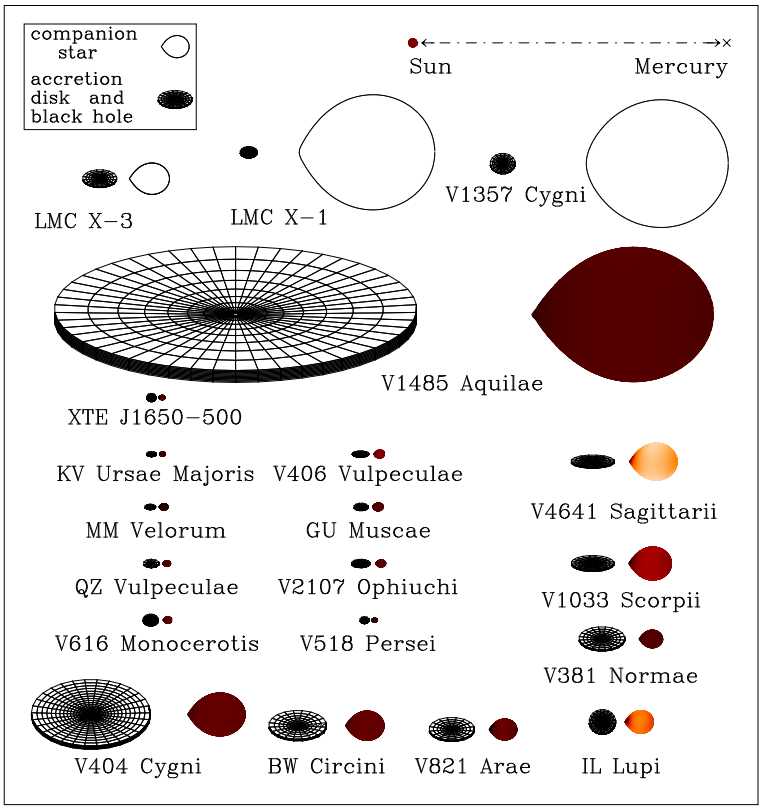


Figure 1.13: *Confirmed Galactic black hole binaries (Courtesy of Jerry Orosz).*

The optical study of binary systems is necessary to discriminate between systems which harbor neutron stars and black holes. As we have seen the possibility of mistakenly considering a neutron star XRB as a black hole XRB is not slim. An observer actually observes $a \sin i$ where i denotes the inclination angle between the orbital and the sky planes and a is the distance between the object and the center of mass of the binary system. Introducing K-velocity as

$$K = 2\pi a \frac{\sin i}{P} \tag{1.8}$$

where P is the orbital period of the binary system and the mass function, f_1, for the donor star with K-velocity, K_1, as

$$f_1 = \frac{PK_1^3}{2\pi G} \tag{1.9}$$

and rearranging Kepler's third law for a binary system

$$\frac{4\pi^2}{GP^2} = \frac{M}{a^3}$$

$$\begin{aligned} \mathrm{f}_1 &= \frac{P}{2\pi G}(2\pi a_1 \frac{\sin i}{P})^3 \\ &= \frac{M}{a^3}(a_1 \sin i)^3 \end{aligned} \tag{1.10}$$

for the configuration shown in Fig 1.4 in which M_1 is located on the center of the coordinate, and assuming its distance toward the mass center, $x_{\rm cm}$, is a_1 one can write $a_1 = a\frac{M_2}{M}$ and substitute in Eq.1.10 to get

$$\mathrm{f}_1 = \frac{(\mathrm{M}_2 \sin \mathrm{i})^3}{\mathrm{M}^2} \tag{1.11}$$

Eq. 1.11 states that measuring K_1 and calculating f_1 (Eq. 1.9) can yield an estimate for the mass of the accretor in a binary system.

It is believed that a neutron star with a mass greater than $3M_\odot$ is not stable and should be a black hole. Historically, A0620-00 was the first BHC where optical studies proved the binary system was harbouring a black hole (McClintock & Remillard 1986). Fig. 1.13 shows twenty confirmed Galactic black hole XRBs. The distances are scaled to the distance between the Sun and Mercury.

Seventeen XRBs of these 20 black hole binary systems exhibit outbursts and are known as **X-ray Transients (XRTs)** or **X-Ray Novae (XRN)**. XRTs appear in the X-ray sky with a sudden outburst from quiescence ($\mathrm{L_x} \sim 10^{31-33}\mathrm{erg\,s^{-1}}$) to a bright luminosity of $\sim 10^{37-38}\mathrm{erg\,s^{-1}}$ and after spending a few months in outburst return to quiescence. A0620-00, whose light curve is shown in Fig. 1.14, was the first transient discovered. Later, studies showed that about one third of known Galactic XRBs (200 sources) are transients (Tanaka & Shibazaki 1996). Extra-galactic XRTs which are the subject of this thesis are studied in detail in Chapters 4 and 5.

1.4 Radiation Processes in High Energy Astrophysics

The dominant radiation processes which produce X-rays can be divided into two classes: Thermal and non-thermal. For thermal processes the rate at which energy is radiated depends on the temperature of the emitter, whilst for the non-thermal process it does not.

- **Thermal emission**

  1. **Bremsstrahlung radiation**

     Bremsstrahlung radiation (literally; braking radiation), schematically shown in Fig.

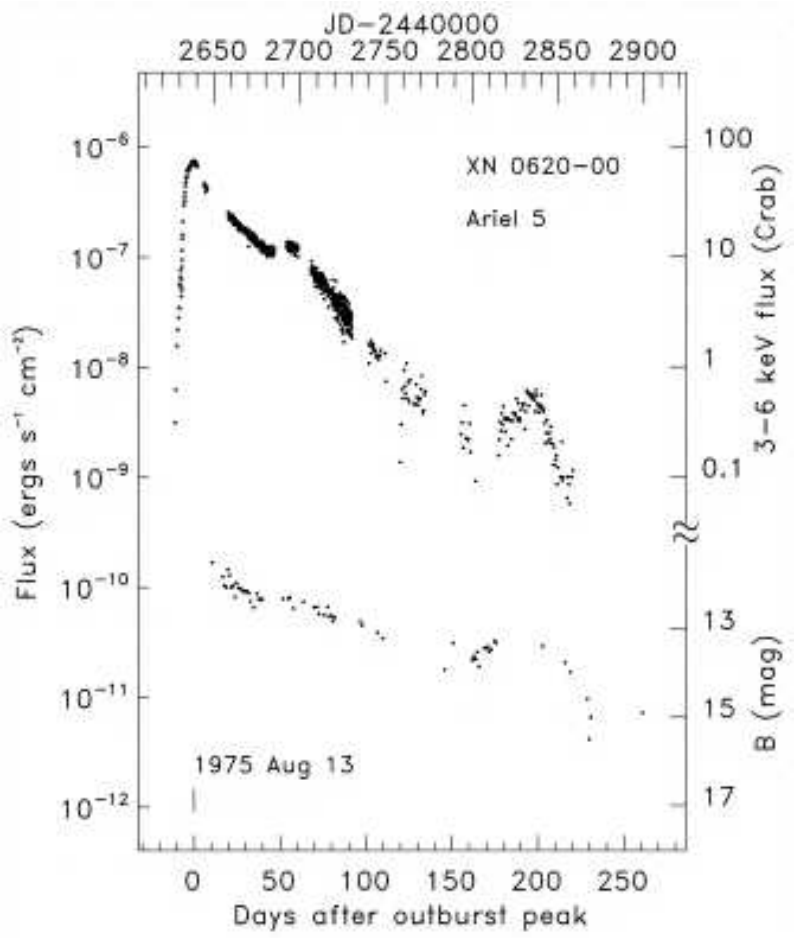


Figure 1.14: *Light curve of A0620-00 (Chen et al. 1997).*

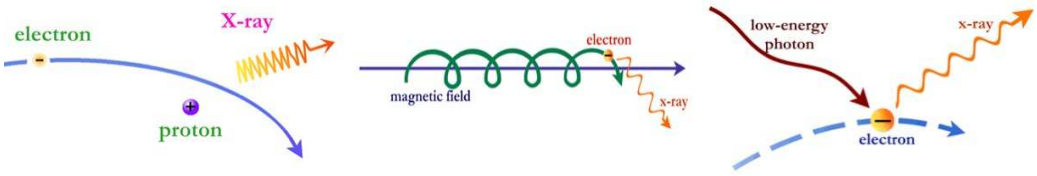
1.15a[3], happens when an electron is scattered by the electric field of another charged particle, either an ion or another electron. The electrostatic force between the two particles causes a change in the trajectory of the electron and it radiates X-rays.

2. **Black body radiation**

   A perfect blackbody is an idealized object that absorbs any radiation incident upon it, regardless of frequency and angle of incidence. A black body in thermal equilibrium is an ideal emitter and the spectrum has a peak at an energy dependent only on the temperature. The spectral distribution of black body radiation is given by the Planck function (Eq. 2.16). This function can be used as an approximation for the spectra of stars, accretion discs, etc (see section 2.1).

- **Non-Thermal emission**

[3]Taken from http://www.astro.wisc.edu/ bank/img



(a) bremsstrahlung radiation (b) Synchrotron radiation (c) inverse Compton

Figure 1.15: *Schematic illustration of the different radiation mechanisms.*

Although most of the emission from XRBs is thermal, non-thermal emission plays an important role too:

1. **Synchrotron emission**

   Synchrotron or *magnetic bremsstrahlung* emission, schematically shown in Fig. 1.15b, is radiation due to a fast moving electron in a magnetic field. The perpendicular force exerted from the magnetic field changes the trajectory of the electron and therefore, it emits an electromagnetic wave.

2. **Inverse Compton scattering**

   An ultra-relativistic electron traveling and colliding with a photon can produce X-rays. In the electron frame, this is Compton scattering, but in the laboratory frame the scattered photons are Doppler shifted to higher energies and the process is called *Inverse Compton scattering*. It is schematically shown in Fig. 1.15c.

1.4.1 Photoelectric absorption

When a beam of X-rays passes through a slab of material, an X-ray photon may interact with an atom. If during the collision, the atom absorbs the X-ray photon and an electron is removed (shown schematically in Fig. 1.16 [4]) the phenomenon is called photoelectric absorption. During this process, some photons disappear from the beam and the intensity of the transmitted beam is reduced. Photoelectric absorption occurs only when the energy of the X-ray photon transfered to an electrons exceeds the binding energy of the electron in the atom. Therefore, the electron is ejected from the atom with energy equal to $E_{\rm photon} - E_{\rm binding}$ and there are sharp absorption edges in the spectrum corresponding to the binding energies of the inner electronic shells of the elements. In the energy range 0.1-10 keV, the X-ray interstellar absorption curves show edges corresponding to the binding energies of electrons in the K and L shells of light element, such as C and O (Seward

[4] Taken from http://chandra.harvard.edu/graphics/resources/illustrations/x-absorp-72.gif

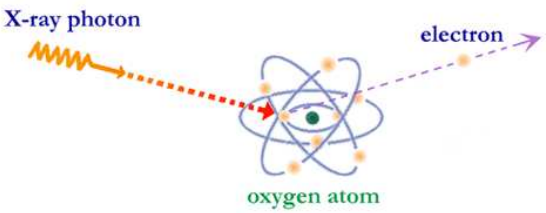


Figure 1.16: *Schematic illustration of photo-electric absorption*

& Charles 2010).

If the intensity of the X-ray beam is $I(x)$ as a function of distance traveled, and the cross-section for absorption by a species with number density $n(x)$ is σ, then

$$\frac{dI}{dx} = -n\sigma I(x)$$

and thus integrating

$$I = I_0 \exp(-\int n\sigma dx)$$

The integral of the number density along the line of sight is usually called the column density in astronomy.

Strictly this applies to each different atomic species, each of which has a different absorption cross-section and column density, but if the chemical composition is fixed and uniform, then all the column densities are proportional to that of the most abundant element, hydrogen, and the total absorption can be expressed as a reduction of the intensity by a factor of $\exp(-N_H\sigma_{\rm total})$ where N_H is the hydrogen column density and $\sigma_{\rm total}$ is a weighted sum of absorption coefficients for all the common elements.

In order to take the photoelectric absorption effect into account in spectral fitting, several models are implemented in XSPEC, e.g. **phabs** which is the simplest function and the redshifted variant **vphabs** [5].

In this Chapter, we started with a brief history of X-ray astronomy, and the first detection of bright X-ray binaries. We then followed this with an overview of the basics of stellar evolution, the Roche potential for interacting binary systems, and the process of accretion. X-ray binaries can

[5] http://heasarc.gsfc.nasa.gov/xanadu/xspec/manual/XSmodelPhabs.html

be classified depending on the mass of the donor star into two main subclasses, low mass X-ray and high mass X-ray binaries, and we have presented their main observational characteristics.

We next discussed binary X-ray sources in the context of the mass of the compact object - i.e. white dwarf, neutron star or black hole. We highlighted the similarities between the outbursting behavior of some LMXBs and the subclass of accreting white dwarfs (CV) known as dwarf novae. Furthermore, the use of optical spectroscopy employed to study both CVs and LMXBs was presented to show how the mass of the compact object can be constrained. We finished with a very brief overview of thermal and non-thermal radiative processes thought to be important for X-ray binaries.

Several of these topics will be discussed in more detail in the following Chapters.

2

Accretion Power

Accretion onto a compact object is the most efficient process known for converting matter into energy. Accreting a particle with mass m onto an object with mass M and radius R_* releases $\triangle E_{\rm acc} = \dfrac{GMm}{R_*}$ (Eq. 1.3). In the case where a neutron star acts as the accretor ($M \sim M_\odot$ and $R_* \sim 10$ km) the energy released is about $\triangle E_{\rm acc} \sim 10^{20}{\rm erg\,g^{-1}}$. The other powerful energy producer is nuclear fusion reaction. For comparison, one can consider the maximum nuclear energy from mass m is $\triangle E_{\rm nuc} = 0.007{\rm mc}^2$ and is approximately $10^{18}{\rm erg\,g^{-1}}$. In this example, the accretion energy is about 100 times larger than the released nuclear energy. Since the liberated energy from accretion depends on the compactness of the accretor (i.e. $\dfrac{M}{R_*}$), stronger accretion is expected from Black Hole Binaries (BHBs); Accretion onto a black hole is capable of converting ten percent of rest mass to energy.

As has been explained in section 1.3, the matter is accreted from a companion star. In general, matter cannot land directly on the surface of the compact accretor, or disappear directly through

the event horizon in the case of BHBs, due to its angular momentum.

The earliest efforts to study the accretion mechanism were performed by von Weizsäcker (1951) and Lüst (1952). Among the different descriptions (Pringle & Rees 1972; Shakura & Sunyaev 1973; Lynden-Bell & Pringle 1974; Eardley & Lightman 1975), the model known as standard or $\alpha-$disc suggested by Shakura & Sunyaev (1973) has became widely accepted as the simplest one. A more detailed description is given in section (2.1).

In the standard accretion disc model, the efficiency of viscous transportation and radiation is very high, which makes it difficult to explain some facts such as the existence of X-ray emission in the quiescence state of X-ray transients. Narayan & Yi (1994) proposed a new mechanism with less efficiency in radiating dissipated energy, known as Advection-Dominated Accretion Flow (ADAF). The ADAF model is discussed in section 2.2.

From the early days of X-ray binary studies, it was discovered that the emission states of BHBs switch between distinct spectral states. The most important states are the thermal state (or High/soft state), low/hard state and quiescence. Reviewing this topic and the efforts to find explanations are the subject of section 2.3.

2.1 Standard Accretion Disc Model

Accretion discs are expected to form in an astrophysical system whenever matter with significant angular momentum tends to accrete towards an accretor. In an accretion disc, a mechanism(s) is needed to transport angular momentum outwards. This mechanism is usually called *viscosity*.

The tangential stress inside a disc can be connected to four quantities: magnetic field, turbulence, molecular and radiation viscosity. The contribution of the molecular viscosity and the radiation viscosity (which is the result of accretion) to angular momentum transportation is not large enough to be able to form an efficient accretion disc. Shakura & Sunyaev (1973) identified either magnetic field or turbulence, as the most likely mechanisms.

Shakura & Sunyaev (1973) suggested that an accretion disc can be modeled using Newtonian mechanics, regardless of the physics of the responsible mechanism that transports angular momentum and produces effective viscosity, by introducing a dimensionless parameter, α, to formulate the kinematic viscosity of the disc

$$\nu_{\rm vis} = \alpha H c_s \tag{2.1}$$

where c_s is the local sound speed, and H the scale height at radius R is

$$H \sim \frac{c_s}{v_\phi} R,$$

and v_ϕ is the azimuthal velocity. In a thin disc (i.e. $H \ll R$), the azimuthal velocity is close to the Kepler velocity

$$v_\phi \sim v_k = \sqrt{\frac{GM}{R}}.$$

This model ($\alpha-$disc model) is named after choosing parameter α to accommodate all of the unknown parameters. Theoretically, the only criterion is $\alpha \leqslant 1$ but observations and numerical simulations (using the $\alpha-$disc assumptions) have shown that α varies in the range of $\simeq$ 0.1-0.4 (King et al. 2007).

It should be noted that the $\alpha-$disc model is incomplete. Due to the unknown physics of viscosity in this model, the physical explanation for $\alpha(\mathbf{r}, t)$ is poorly understood.

The simplest approach to describe an accretion disc is to consider **steady-state discs** in which the accretion pattern does not change with time (*derivations for this section are obtained from Kolb (2010)).* Mathematically speaking, the partial derivative of any parameter with respect to time vanishes (i.e. $\dfrac{\partial}{\partial t} = 0$). The assumption that the disc is **geometrically thin** allows for the reduction of the three dimensional equation to a two dimensional one and defines the surface density for the accretion disc in a cylindrical coordinate system, (r, ϕ, z), as

$$\Sigma(r) = \int_{-\infty}^{+\infty} \rho(r, z) dz \tag{2.2}$$

The disc mid-plane is assumed to be located in the z = 0 plane and ρ is the density of the disc fluid. Thus, the vertical disc scale height, H, is defined as $\Sigma = H\rho$.

The viscous torque in the accretion disc rotating with the angular speed ω at r from the rotation axis, is given by

$$G_{\text{vis}} = -F \times r, \tag{2.3}$$

where F is the viscous force and can be derived by multiplying the surface area (A) by viscous stress (σ_s). Thus

$$F = A\sigma_s = 2\pi r H \sigma_s \tag{2.4}$$

Viscous stress can be written as $-\nu_{\rm vis}\rho\dfrac{\partial v}{\partial r}$. The orbital speed of the gas in the ring is $v = r\omega$, therefore

$$\frac{\partial(r\omega)}{\partial r} = r\frac{\partial\omega}{\partial r} + \omega$$

since viscous stresses exist only in the presence of shearing motion, only the first term, $r\dfrac{\partial\omega}{\partial r}$, contributes to the sheer stress. So, replacing these values in Equations 2.3 and 2.4, one can derive the viscous torque as

$$G_{\rm vis} = 2\pi rH(\nu_{\rm vis}\rho r\frac{\partial\omega}{\partial r})r$$

replacing $\Sigma = H\rho$ leads to

$$G_{\rm vis} = 2\pi r\nu_{\rm vis}\Sigma r^2\frac{\partial\omega}{\partial r},$$

assuming a Keplerian orbit and therefore using $\omega = \left(\dfrac{GM}{r^3}\right)^{1/2}$ yields:

$$G_{\rm vis} = -3\pi\nu_{\rm vis}\Sigma(GMr)^{1/2} \tag{2.5}$$

To quantify the amount of the heat energy liberated, consider three concentric adjacent gas rings, named A, B and C ordered by the smallest radius first. The inner and outer radii of the middle ring (ring B) are r and r + Δ r, respectively. The innermost ring (ring A) rotates faster than ring B and therefore a positive torque $|G_{\rm vis}(r)|$ is exerted on ring B from ring A. On the other side, ring C rotates slower than ring B, so a negative torque $-|G_{\rm vis}(r+\Delta r)|$ is on B from C. Due to the dependence of the torque on r, the net torque on ring B is non-zero, i.e .

$$|G_{\rm vis}(r)| - |G_{\rm vis}(r+\Delta r)| \neq 0.$$

The rate of work is given by

$$\frac{dW}{dt} = G_{\rm vis}\times\omega.$$

Therefore, viscous dissipation deposits energy into a ring at a rate of

$$G_{\rm vis}\times\Delta\omega$$

where $\Delta\omega$ is the difference between the angular speeds at the outer and inner edges of the ring.

One can write $\Delta\omega$ as

$$\Delta\omega \approx \frac{\partial\omega}{\partial r}\Delta r$$

if the width of the ring, Δr, is small. Therefore, the viscous dissipation in the disc ring occurs at a rate

$$\frac{dW}{dt} = G_{\rm vis}\Delta r\frac{\partial\omega}{\partial r}.$$

Normalizing this to the surface area of the disc ring ($2\pi r\Delta r$) yields to the dissipation rate per unit surface area

$$D(r) = \frac{G_{\rm vis}\Delta r\dfrac{\partial\omega}{\partial r}}{2\times 2\pi r\Delta r} = \frac{1}{2}\nu_{\rm vis}\Sigma(r\frac{\partial\omega}{\partial r})^2. \tag{2.6}$$

A disk has two sides, thus a factor 2 in the denominator has been added. Assuming the content of the disc is moving with Keplerian velocity means that the energy liberated as heat is equal to

$$D(r) = \frac{9}{8}\nu_{\rm vis}\Sigma\frac{GM}{r^3} \tag{2.7}$$

To obtain a value for $\nu_{\rm vis}\Sigma$, one needs to derive the conservation of angular momentum. When the angular momentum is in balance (i.e. $\frac{\partial G_{\rm vis}}{\partial r} = 0$), the angular momentum J in a disc, between radii r and r+Δr can be written as

$$\Delta J = [j(r+\Delta r,t) - j(r,t)]\times\Delta t \approx \Delta r\frac{\partial j}{\partial r}\times\Delta t.$$

An imbalance only happens in a ring when the angular momentum that flows into the ring, and the angular momentum leaving the ring are not equal. The angular moment of the flow can be calculated by $r^2\omega\times\dot{M}$ where $\dot{M}(r,t) = -2\pi r v_r\Sigma$. Therefore, the local flow rate of angular momentum is

$$j = -2\pi r v_r\Sigma r^2\omega,$$

thus

$$\begin{aligned}\frac{\Delta J}{\Delta t} &= \Delta r\frac{\partial(-2r\pi v_r\Sigma r^2\omega)}{\partial r}\\ &= -2\pi\Delta r\frac{\partial(r v_r\Sigma r^2\omega)}{(\partial r)}\end{aligned}$$

One the other hand, the total angular momentum, J, in the disc ring is calculated by multiplying

mass in the ring by the specific angular momentum (i.e. $2\pi r\Delta r \times \Sigma \times r^2\omega$). Therefore, one can write

$$\frac{\partial J}{\partial t} = 2\pi r\Delta r \frac{\partial}{\partial t}(\Sigma r^2\omega)$$

For small time intervals, one can equate the right hand side of the two previous equations and cancel $2\pi\Delta r$ as follows:

$$r\frac{\partial}{\partial t}(\Sigma r^2\omega) + \frac{\partial(rv_r\Sigma r^2\omega)}{\partial r} = 0 \tag{2.8}$$

Assuming angular momentum is balanced, Eq. 2.8 is derived. But for the general case, one can write the net viscous torque as

$$G_{\mathrm{vis(r+\Delta r)}} - G_{\mathrm{vis}}(r) \simeq \Delta r\frac{\partial G_{\mathrm{vis}}}{\partial r}.$$

Eq. 2.8 is derived by canceling factor $2\pi\Delta r$, so thus the right hand side of equation above must be normalized to this factor to be able to write the conservation of angular momentum as

$$r\frac{\partial}{\partial t}(\Sigma r^2\omega) + \frac{\partial}{\partial r}(rv_r\Sigma r^2\omega) = \frac{1}{2\pi}\frac{\partial G_{\mathrm{vis}}}{\partial r} \tag{2.9}$$

Considering the assumption of a steady-state disc and therefore, ignoring the first terms on the left hand side of the conservation laws above, integrating the angular momentum conservation gives

$$rv_r\Sigma r^2\omega = \frac{G_{\mathrm{vis}}}{2\pi} + C \tag{2.10}$$

where C is an integration constant. The left hand side of the equation above can be connected to mass accretion rate, $\dot{M}$, bearing in mind that the disc fluid is drifting inwards with velocity $(-\mathrm{v_r} > 0)$

$$\dot{M} = \frac{\delta M}{\Delta t} = \frac{2\pi r\delta r\Sigma}{\Delta t} = 2\pi r(-\mathrm{v_r})\Sigma \tag{2.11}$$

thus, rewriting the left hand side of Eq. 2.10 as $\dot{M}\dfrac{-r^2\omega}{2\pi}$ yields

$$-\dot{M}(GMr)^{1/2} = G_{\mathrm{vis}} + C \tag{2.12}$$

To determine the value of the integration constant, one needs to set an assumption for the boundary

condition. The assumption can be that the torque at the innermost radius, $R_{\rm in}$, of disc is zero, i.e.

$$G_{\rm vis}(r = R_{\rm in}) = 0 \tag{2.13}$$

Therefore,

$$C = -\dot{M}(GMR_{\rm in})^{1/2}.$$

By having the value of C determined, rewriting Eq.2.12 and replacing the value of $G_{\rm vis}$ from Eq. 2.5, one can write

$$\begin{aligned} -\dot{M}(GMr)^{1/2} &= -3\pi\nu_{\rm vis}\Sigma(GMr)^{1/2} - \dot{M}(GMR_{\rm in})^{1/2} \\ \nu_{\rm vis}\Sigma &= \frac{\dot{M}}{3\pi}[1 - (\frac{R_{\rm in}}{r})^{1/2}] \end{aligned} \tag{2.14}$$

Replacing the value of $\nu_{\rm vis}\Sigma$ from Eq.2.14 in Eq. 2.7, power dissipated per unit disk area can be written as a function of the accretor mass and the accretion mass rate:

$$D(r) = \frac{3GM\dot{M}}{8\pi r^3}\Big[1 - (\frac{R_{\rm in}}{r})^{1/2}\Big] \tag{2.15}$$

In astronomy, the electromagnetic radiation from an ideal object (an object in thermal equilibrium at fixed temperature T) is often modelled as a black body spectrum. Black body radiation, as a local approximation, is a good starting point to estimate the temperature of the object using the Planck function:

$$B_\nu(T) = (\frac{2h\nu^3}{c^2})\frac{1}{\exp(h\nu/kT) - 1} \tag{2.16}$$

where B_ν is the emitted power per unit area per unit frequency per unit solid angle, k and h are the Boltzmann constant and the Plank constant, respectively. The thermal flux from a ring in an accretion disc is $\sigma T^4_{\rm eff}(r)$, where σ and $T_{\rm eff}$ are the Stefan-Boltzmann constant and the effective temperature, respectively. Therefore, the effective temperature of a ring in a geometrically thin optically thick, steady state accretion disc is

$$T^4_{\rm eff}(r) = \frac{3GM\dot{M}}{8\pi\sigma r^3}\Big[1 - (\frac{R_{\rm in}}{r})^{1/2}\Big] \tag{2.17}$$

An accretion disc can be considered as a composition of annuli at different radii where the

temperature of each one might be determined by T(r) = $T_{\rm eff}(r)$ derived in Eq. 2.17. Therefore, the total flux, F_ν, received by an observer located at distance d from the accretion disc is equal to:

$$F_\nu = \frac{1}{d^2}\int_{R_{\rm in}}^{R_{\rm out}} (\frac{2h\nu^3}{c^2})\frac{1}{\exp(h\nu/kT_{\rm eff})-1} r dr d\phi \tag{2.18}$$

accordingly, the thermal emission of the accretion disc which has a multi-temperature profile is called a **Multi-Color Disc (MCD)**.

The total luminosity of the disc is, thus, determined by an integration over the surface of the disc ring between the radii $R_{\rm in}$ and r:

$$\begin{aligned} L(r) &= 2\int_{R_{\rm in}}^{r} D(r) r dr d\phi \\ &= \frac{3GM\dot{M}}{2}\int_{R_{\rm in}}^{r}\Big[1-(\frac{R_{\rm in}}{r})^{1/2}\Big]\frac{1}{r^2}dr \end{aligned} \tag{2.19}$$

The factor 2 in front of the integration comes form the fact that disc has two faces.

Different developments of the MCD models are presented and implemented in XSPEC (X-Ray Spectral Fitting Package, (Arnaud 1996)) to allow it to fit observational data. These models with their assumptions are reviewed in subsection 2.1.1.

2.1.1 Disc Black Body Models in XSPEC

Assuming the black body emission is from the surface of the accretion disc, various models have been proposed to fit the X-ray spectrum of the accretion discs. The models are concisely studied below and summarized along with the references in table 2.1.

- **diskbb**

  The first and the simplest model for standard accretion disc, *diskbb*, has two parameters: $T_{\rm in}$, the effective temperature at the innermost radius of disc ($R_{\rm in}$) in units of keV and the normalization factor, $(R_{\rm in}/d)^2\cos i$, where i is the inclination angle of the disc (i=0 is face-on) and d is the distance. In the diskbb model, the effective temperature as a function of r is assumed $T_{\rm eff}(r) \propto r^{-3/4}$. For $r \geqslant R_{\rm in}$, this can be easily shown by rewriting Eq. 2.17 as

$$T_{\rm eff}(r) \propto r^{-3/4}\Big(1-\sqrt{\frac{R_{\rm in}}{r}}\Big)^{1/4} \tag{2.20}$$

- **diskpbb**

  The *diskpbb* model assumes a power-law dependence for the effective temperature to r:

$$T(r) \propto r^{-\mathrm{p}}, \tag{2.21}$$

  where p is a free parameter. Therefore, this model has one additional parameter, p, comparing to *diskbb*. p = 3/4 simplifies this model to *diskbb*.

- **diskpn**

  In order to take into account the temperature distribution near the black hole, the *diskpn* model useing the pseudo-Newtonian potential $\Phi(R) = \frac{-GM}{R-2R_g}$ where $R_g \equiv \frac{GM}{c^2}$ (Paczyński & Wiita 1980) has been proposed. The model assumes that the disc expands from $r_{\rm in} \equiv \frac{R_{\rm in}}{R_g}$ to infinity. In the model, the two free parameters are: the maximum temperature and the inner disc radius.

- **ezdiskbb**

  It has been discussed in the standard accretion disc model that the boundary condition to obtain $T_{\rm eff}$ is assumed to be zero torque at the inner radius of the disc (Eq. 2.13), but *diskbb* and *diskpn* do not take this into account. Model *ezdiskbb* takes it into account. Introducing T_* as

$$T_* = \Big(\frac{3GM\dot{M}}{8\pi\sigma R_{\rm in}^3}\Big)^{1/4},$$

  one can rewrite Eq. 2.17 as

$$T_{\rm zt}(r) = T_*(\frac{R_{\rm in}}{r})^{3/4}\Big[1-(\frac{R_{\rm in}}{r})^{1/2}\Big]^{1/4}, \tag{2.22}$$

  (zt stands for zero torque). One can show the maximum value of effective temperature is $T_{\rm max} = 0.488T_*$ is at r = $\frac{49}{36}R_{\rm in}$. The maximum temperature and normalization are the only free parameters in *ezdiskbb* model.

  The noticeable difference between the ezdsikbb model and the *diskbb* model is that the estimated size of the $R_{\rm in}$ from *ezdiskbb* is ≈ 2.2 times smaller than the value given by the *diskbb* model.

- **kerrbb**

Model Name	Model parameters		Reference(s)
	T(r)	G(r = $R_{\rm in}$)	
Thin accretion disk (Shakura & Sunyaev 1973)			
diskbb	$\propto r^{-3/4}$	$\neq 0$	(Mitsuda et al. 1984; Makishima et al. 1986)
diskpbb	$\propto r^{-p}$	$\neq 0$	(Mineshige et al. 1994; Hirano et al. 1995) (Kubota & Makishima 2004; Kubota et al. 2005)
diskpn			(Gierliński et al. 1999)
ezdiskbb	Eq. 2.22	$= 0$	(Zimmerman et al. 2005)
Relativistically thin accretion disc (Novikov & Thorne 1973)			
kerrbb		$\neq 0$	(Li et al. 2005)
bhspec			(Davis & Hubeny 2006)

Table 2.1: *A summary of multi-colour disc models implemented in XSPEC, with the temperature and the torque.*

The fully relativistic version of MCD, based on a relativistic thin disc model, around a Kerr black hole with non zero torque at $R_{\rm in}$ and accounting for self-irradiation of the disc.

The innermost stable circle orbit (ISCO) around a Kerr black hole (a spinning black hole) is R_g. Thus, the accretion disc around a Kerr black hole can extend further inward. So, a brighter accretion disc is expected around a Kerr black hole (see Eq. 1.4 as a rough estimate).

- **bhspec**

  Davis & Hubeny (2006) proposed a relativistic disc model similar to *kerrbb*. The difference between these two models is in the approach to the emission at the disk surface. *kerrbb* considers isotropic emission or an analytic limb darkening profile where *bhspec* uses stellar atmosphere-like calculations.

2.2 Advection-Dominated Accretion Flow (ADAF)

In the α-disc model (section 2.1), the thermal energy produced by the viscous dissipation is locally converted to radiation and released. Therefore, the temperature of the disc remains lower than the virial temperature and the disc stabilizes. Narayan & Yi (1994) considered an accretion flow where the radiation efficiency is not high enough to cool the disc down to the virial temperature. As an explanation, Narayan & Yi (1994) examined the case where the bulk of the thermal energy is stored in the flow and advects inwardly. They coined the name **Advection-Dominated Accretion Flow (ADAF)** for this accretion regime. In an ADAF model, most of the energy dissipated via viscosity remains in the disc and advects with the flow rather than being released in the form of radiation. Therefore, the radiative efficiency of an ADAF is much less than in the standard

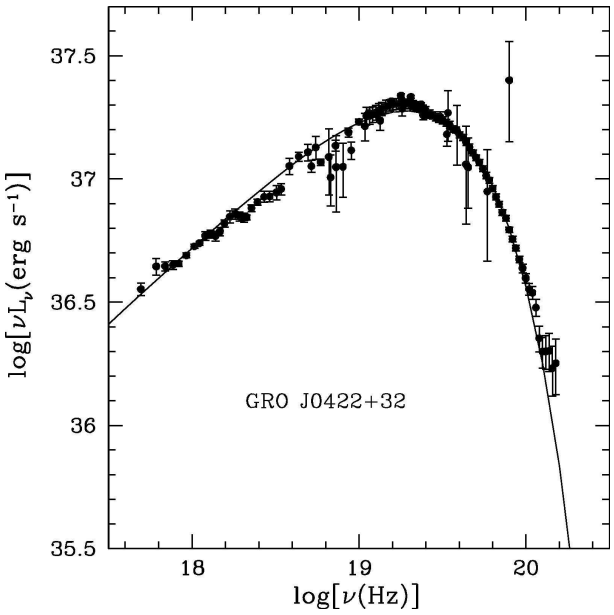


Figure 2.1: *GRO J0422+32 in the hard state emission and an ADAF model (the solid line) with* $\dot{M} \sim 0.1\dot{M}_{\rm Edd}$ *(adapted from (Narayan & McClintock 2008)).*

accretion disc model. The energy equation for an accretion disc can be written in the following compact form:

$$\rho \mathrm{T}\frac{\mathrm{dS}}{\mathrm{dt}} = \mathrm{q}_{+} - \mathrm{q}_{-} \tag{2.23}$$

where ρ and T are the density and the temperature of the flow, respectively. S is the entropy per unit mass, and q_+ and q_- are the heating and cooling rates per unit volume. Since any entropy stored in the flow is advected with the flow, the right hand side of Eq. 2.23 can be renamed as the effective advective cooling rate, $q_{\rm adv}$, and one can rewrite this equation as:

$$q_{+} = q_{-} + q_{\rm adv} \tag{2.24}$$

This new arrangement of Eq. 2.23 states that the heat energy released from the viscous dissipation is lost by the radiative and the advective cooling. In the case where the radiation is the efficient cooling process, i.e. $q_- \gg q_{\rm adv}$, the standard accretion disc model (section 2.1) is applicable and where the advective cooling forms the major portion of cooling rate, i.e. $q_{\rm adv} \gg q_-$, an (ADAF) model will be the corresponding regime.

While the thermal emission of neutron star XRBs and BHBs can be modeled very well by a geometrically thin, optically thick accretion disc, the emission of hard state was a mystery for many years. As a typical BHB in hard state, figure (2.1) shows the spectrum of GRO 4022+32 taken with TTM (2-20)keV and HEXE (20-200keV). The measured gas temperature from the observations

indicate that the gas is very hot, kT $\geq$ 100 keV. Assuming the standard thin accretion disc is the correct model for this spectrum then for any reasonable estimate of radiating area A, one can calculate $\mathrm{L} = \sigma \mathrm{T}^4 \mathrm{A} \geq 10^{46} \mathrm{erg\,s^{-1}}$. So, the accretion disc should be optically thin and it cannot be explained by the standard α-disc model. To explain the hard state of GRO J0422+32, employing an ADAF model with $\dot{M} \sim 0.1 \dot{M}_{\mathrm{Edd}}$ (the solid line in the Fig. 2.1) gives a satisfactory fit.

Advection dominated accretion has two distinct regimes:

1. **Radiatively Inefficient Accretion Flow (RIAF):** This model assumes that the cooling time is very long and the accreting gas is tenuous, i.e. $t_{\mathrm{cool}} \gg t_{\mathrm{acc}}$ where t_{cool} and t_{acc} are the cooling time of the gas and the accretion time, respectively.

2. **Slim disc**: In this model, the particles have no trouble cooling but the scattering optical depth is so large that the radiation cannot diffuse out of the system. The condition for this model is $t_{\mathrm{diff}} \gg t_{\mathrm{acc}}$ where t_{diff} is the diffusion time for photons and t_{acc} is the accretion time. This regime was discussed by Begelman (1979) and developed by Abramowicz et al. (1988).

Hereafter whenever ADAF is used it refers to the RIAF regime. Therefore, the defining characteristic of an ADAF model is that the gas is not radiatively efficient and the energy from the viscous dissipation is stored in the gas and advects with the flow.

Historically, it was the quiescence state of a transient XRB that was first connected to an ADAF model. Narayan (1996) showed that while a thin accretion disc model cannot be fitted to A0620-00 in quiescence, a model consisting of an ADAF at small radii and a thin disc at large radii can successfully explain the quiescent spectrum. Later, Narayan et al. (1997a) modeled the spectrum of V404 Cygni in quiescence and again showed that an ADAF model fits the spectrum very well. Figure 2.2 shows that an ADAF model (solid line) which corresponds to $\dot{M} \sim 0.005 \dot{M}_{\mathrm{Edd}}$ and a thin disc model (dashed line) which is adjusted to fit the optical data (the three dots on the left). The 2σ limits on the error box in the X-ray from ASCA is shown in the right side of the figure.

Narayan & Yi (1994) and Narayan & Yi (1995) discovered from the properties of ADAF solutions that the accreting gas in an ADAF model has a positive Bernoulli parameter which is defined as:

$$Be = \frac{v^2}{2} - \frac{GM}{R} + w \tag{2.25}$$

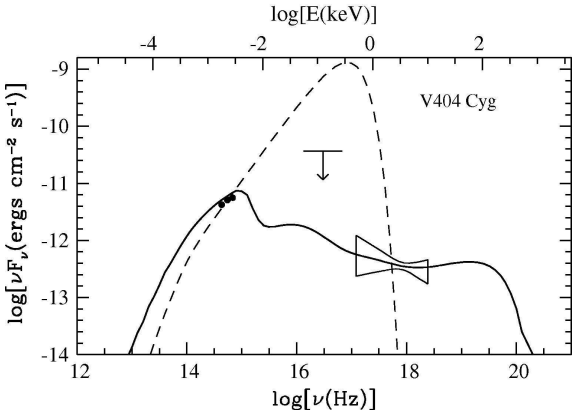


Figure 2.2: *The spectrum of V404 Cygni in quiescence, the dashed line is standard thin accretion disc and the solid line is an ADAF model with* $\dot{M} \sim 0.005\dot{M}_{\rm Edd}$ *(adapted from (Narayan & McClintock 2008)).*

and is the sum of the kinetic energy, potential energy and entropy. Having a positive Bernoulli parameters means the gas is not bound to the BH. Thus, there should be jet emission and strong winds if the ADAF model is viable. The numerical simulations support this discovery (Stone et al. 1999; Igumenshchev & Abramowicz 2000; Igumenshchev et al. 2000). The discovery of non-thermal relativistic jets with radio observations in the hard state of BHB support this theory (Corbel et al. 2000; Fender 2001; Fender & Belloni 2004; Fender et al. 2004). One can expect to observe jet emission from a BHB in quiescence since the dominant regime of accretion is ADAF. Radio observations of V404 Cyg (Gallo et al. 2005) and A0620-00 (Gallo et al. 2006) support this prediction.

2.3 The Emission States of Black Hole Binaries

While observing Cyg X-1 in spring 1971, Tananbaum et al. (1972) found a noticeable change in the X-ray state: the average soft flux (2-6 keV) decreased by a factor of 4, while the average hard flux increased by factor of 2 and simultaneously the radio counterpart brightened. Observation of a similar emission state change in A0620-00, suggested that a common mechanism is at work in both transient and permanent BHBs (Coe et al. 1976). These results suggested that the study of X-ray emission states from BHBs offers a promising place to find changes in the different accretion regimes.

Studying spectral and quasi-periodic oscillations (briefly described below) of Galactic BHBs in XRTE observations, McClintock & Remillard (2006) classified five distinct emission states which will be discussed below.

It is known from Fourier transformation that any function can be written as a summation of sine and cosine functions. In order to find any periodicity in a set of data I_j taken on t_j, one

should calculate the **Power Density Spectrum (PDS)** as

$$P(f_k) \sim \Big[\sum_{j=1}^{N} I_j \cos(2\pi f_k t_j)\Big]^2 + \Big[\sum_{j=1}^{N} I_j \sin(2\pi f_k t_j)\Big]^2, \tag{2.26}$$

The existence of a spike in the diagram PDS versus frequency shows an oscillation.

Analyzing EXOSAT observations of NS LMXB GX5-1, van der Klis et al. (1985) discovered an oscillation from the binary system at a frequency of about 19 Hz. Since the period is not stable, **Quasi-Periodic Oscillations (QPOs)** became the standard designation. The proposed scenario is that a neutron star in a binary system is old and its magnetic field is weak. Accretion discs therefore can penetrate through the magnetosphere and clumps of accreted matter can fall down on the surface of the neutron star from the magnetic poles. The Launch of the Rossi X-Ray Timing Explorer (RXTE) in 1995 and the study of QPOs from BHBs provided a new opportunity to gain a more detailed insight into the different emission states. For example, the presence of high frequency QPO (40-450 Hz) in a BH XRB gives information from the ISCO; the orbital frequency at ISCO around a Schwarzschild black hole is $\sim 220(M/10\dot{M})^{-1}$Hz (even higher for a Kerr black hole) (Remillard & McClintock 2006a).

The rest of this section is devoted to the emission states of BHBs. The first three states are the most frequently detected ones. The last two have been observed in some BH XRBs.

1. **Thermal dominant (High/Soft)**: The emission state in high luminosities has been referred as Thermal dominant. The Multi-color disc model (section 2.1) with $kT_{\rm in} \sim 1.0$ keV can be fitted successfully to the data of this state (see the explanation of $T_{\rm in}$ in the diskbb model in page 29). This state is also called the High/Soft state because of its high luminosity and soft X-ray emission.

   Studies of the spectrum of three Galactic BHB (GS1124-68, GS2000+25, LMC X-3; see more in Tanaka & Lewin (1995)) with Ginga showed that the value of $(R_{\rm in}/d)^2 \cos i$ remain notably constant over a wide range of accretion rates. This fact has been interpreted as the finger print of an optically thick geometrically thin accretion disc.

   Fig. 2.3 shows RXTE observations of five Galactic BHBs in the thermal dominant state. The energy spectrum (left panel) decomposed into two components: a thermal component (solid line) and a power law component (dashed line). The thermal component is dominant below ~ 10 keV and as explained above assumed to be originated from an accretion disc. The hard

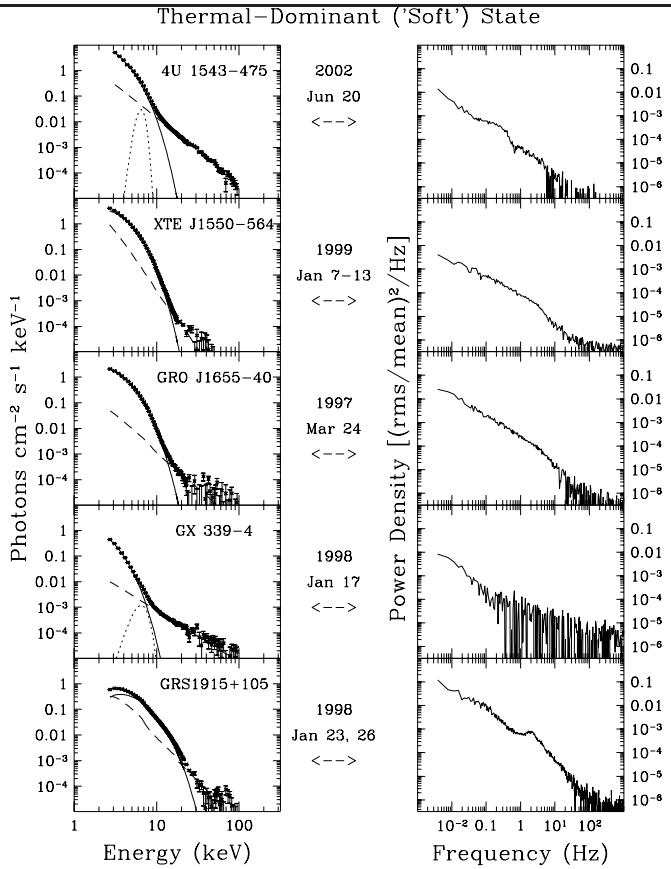


Figure 2.3: *RXTE observation of BHB during thermal-dominant (HS) state. The left panel shows the energy spectra which are decomposed into a thermal component (solid line), and a faint powerlaw component (dashed line). For two of the BHBs, an Fe line component (dotted line) is included in the model. The right panel is devoted to the corresponding power spectra of the BHBs which shows no spike. One of the characteristic features of the thermal dominant state is that there are no QPOs or very weak features (rms ≪ 1%) (McClintock & Remillard 2006).*

tail may be displayed in spectrum, however its contribution in the total flux is small.

The right panel of Fig. 2.3 shows the corresponding power spectra in the thermal dominant emission state. As can be seen there is no spike, and therefore no QPOs. One of the characteristic features of the thermal dominant state is that its PDS show no QPOs or very weak features (rms $\ll$ 1%).

2. **Low/Hard (LH)**: As noted previously, Cyg X-1 exhibits a non-thermal spectral state which is called Low/Hard (LH), after its lower luminosity when compared to the high state. The X-ray spectrum can be modeled in the range of 1-20 keV with a power law function with a Γ1.7.

   Fig. 2.4 presents the spectra of five BHBs taken with RXTE during the LH state. The existence of an accretion disc in this emission state is a controversial subject. Observations with ASCA in the range of 0.5 to 9 keV of GX 339-4 (Wilms et al. 1999) and Cyg X-1 (Takahashi et al. 2001) show that in addition to a power law component, the soft spectra can be modeled with $\sim$ 0.1-0.2 keV accretion disc. The observations with RXTE could not

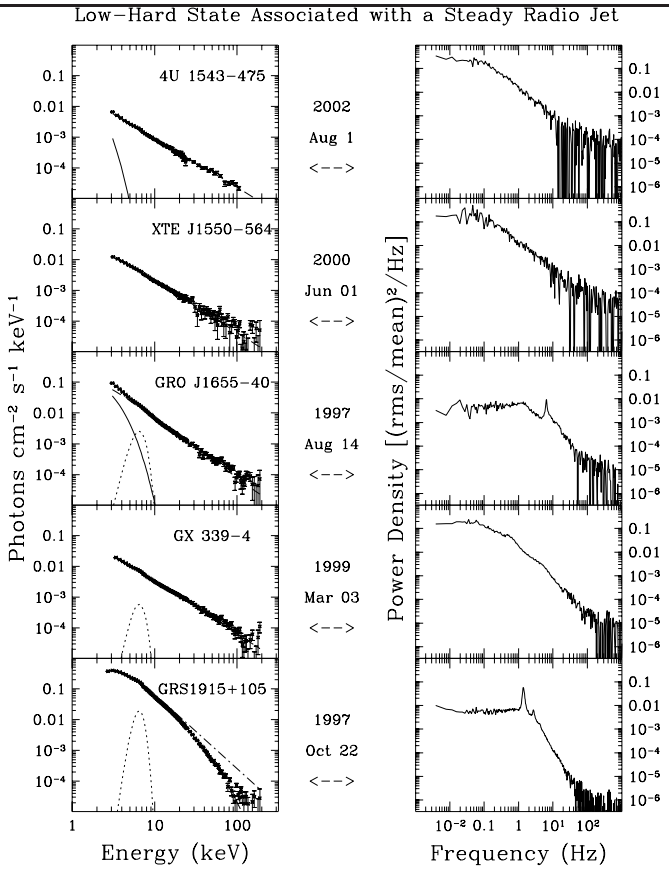


Figure 2.4: *RXTE observation of BHBs during the hard state. The left panel shows the individual spectral components which are included, the powerlaw (dashed line) and, if detected, the accretion disk (dotted line). A relatively flat powerlaw component ($\Gamma \sim 1.7$) that dominates the spectrum above 1 keV is one of main characteristics of the hard state. The right panel shows the corresponding power spectra. In this emission state, QPOs may be either present or absent (McClintock & Remillard 2006).*

improve this due to the lack of sensitivity of this detector to temperatures below 1 keV. With the simultaneous Hubble space telescope, Extreme Ultraviolet Explorer (EUVE) and Chandra observations, McClintock et al. (2001) showed that the inner radius and temperature of an accretion disc model in the hard state are $\geq 100\ R_{\rm g}$ and ≈ 0.024 keV, respectively. The physics of a truncated accretion disc at this distance from the accretor is still controversial.

The right panel of Fig.2.4 shows the corresponding power spectra. The total rms power (r) integrated over 0.1-10 Hz, in the hard state is in the range $0.1 < \mathrm{r} < 0.3$, which is significantly higher than that of the thermal dominant state.

The origin of the X-ray power law is another controversial subject. Generally, the power law fit is the fingerprint of a non-thermal mechanism. It has been shown that the spectrum of XTE J1118+480 can be fitted with an ADAF model (Esin et al. 2001), a synchrotron model (Markoff et al. 2001) and a thermal-comptonization model (Frontera et al. 2001).

3. **Quiescence**: Most of the life time of a transient system is spent in quiescence with very faint luminosity ($L_x = 10^{30.5} - 10^{33.5} \mathrm{erg\,s^{-1}}$) characterized by a non-thermal and hard spectrum

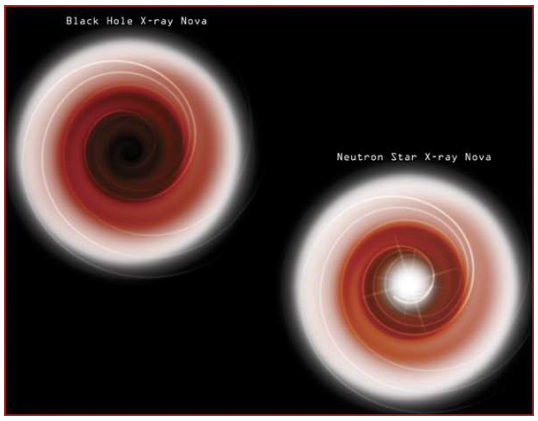


Figure 2.5: *Artist impression of the difference between brightness of BH transient versus a NS transient during quiescence.*

(Γ=1.5-2.1).

More sensitive measurement of the quiescence state of the Galactic transient systems become possible once Chandra and XMM-Newton were launched. Because they have a physical surface, it is expected that the quiescent of neutron star transients would be brighter than black hole transients. The residual thermal energy dissipated via viscosity disappears through the event horizon of the black hole, while in a neutron star binary system, this energy radiates away from the surface of the neutron star. An artist's impression of the difference in the brightness of these systems is shown in Fig. 2.5 [1].

By gathering the available observations of NS and BHB transients in quiescence, Narayan et al. (1997b) showed that indeed NS systems are consistently brighter than BHB transients. Later, Lasota & Hameury (1998) pointed out that only the quiescence of binary systems with similar mass should be compared. The best way to look at this comparison is to plot luminosity as a function of the orbital period of the binary system. A plot of the Eddington-scaled luminosities in 0.5-10.0 keV of BH transients (filled circles) and NS transients (open circles) versus the orbital period as shown in Fig. (2.6), provides an observational support for the comparison.

4. **Steep-Power Law (SPL)**: During the most luminous emission of some BHBs, when the luminosity becomes $> 0.2L_{\rm Edd}$, non-thermal emission with typical $\Gamma \gg 2.4$ is dominant. This state is called the Steep-Power Law (SPL) state because of the very steep power index or the **Very High (VH)** state due to its exceptional brightness.

   In the right panel of Fig.2.7, the corresponding power spectra is presented. A main feature

[1] Figure from http://www.astro.virginia.edu/ mnc3z/images/astro124/blackhole_illustration.jpg

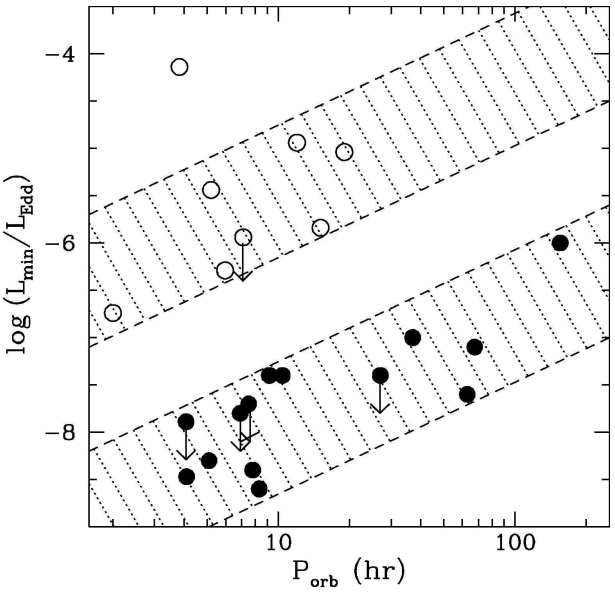


Figure 2.6: *Eddington-scaled luminosities of BH transients (filled circles) and NS transients (open circles) versus orbital period (Narayan & McClintock 2008).*

of the SPL emission state is either there are Xray QPOs present (0.130 Hz) while the power law contributes more than 20% of the total (unabsorbed) flux at 220 keV, or the powerlaw contributes more than 50% of the total flux without detections of QPOs.

By observing the spectra of several black hole candidates in the hard state with the Compton Gamma Ray Observatory (CGRO) (40-500 keV), Grove et al. (1998) found a steep cutoff near 100 keV. While the power index of the SPL state and hard state are similar, the SPL state did not show any cutoff in the higher energies. Thus, it is necessary to discriminate between the SPL state and the hard state.

The spectra of five Galactic BHBs shown in Fig. 2.7 in the SPL state shows a strong and steep power law component.

5. **Intermediate states**: Despite defining four distinct different emission states, there are some exceptions that cannot be perfectly placed in any of these states, e.g. XTE J1550-564 and GRS 1915+105 exhibit spectral properties consistent with the SPL state, but the PDS are characteristic of the hard state (see Fig. 2.8). In the lower panel of the figure, SAX J1819.3-2525 shows that its spectra does not coincide any of the mentioned states. These all necessitate the definition of a group of new states, called Intermediate states.

Based on the ADAF's solution properties, Narayan (1996) proposed a model for accreting BHBs to help understand the spectral states. Later, Esin et al. (1997) presented the schematic. Due to the mysterious nature of very high state (or SPL), in the more recent image, Narayan

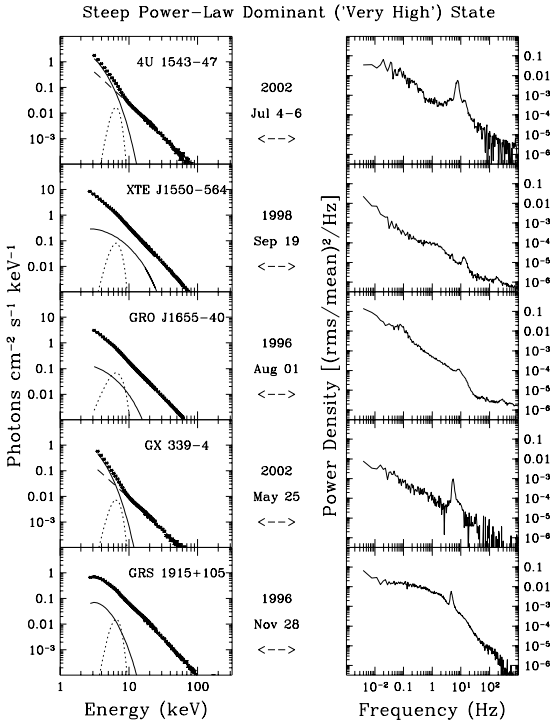


Figure 2.7: *RXTE observations of BHBs during Steep Power Law (SPL) state. The left panel shows the energy spectra decomposed to the thermal component (dotted) and the power law component (dashed). This state is characterized by a strong and steep power law component (typically* $\Gamma \geqslant 2.4$ *which is much steeper than the value of the power law in the low-hard emission state (*$\Gamma \sim 1.7$*). The right panel shows the corresponding power spectra. In some BHBs, QPOs have been detected (see text for more explanation). (McClintock & Remillard 2006).*

& McClintock (2008) removed that state from the image (shown in Fig. 2.9). The solid line depicts a standard accretion disc and the concentration of dots presents the intensity of ADAF flow. The key parameter in their model is $\dot{M}$. When $\dot{M} > \dot{M}_{\rm crit}$ the disc expands to the Innermost Stable Circular Orbit (ISCO). $\dot{M}_{\rm crit}$ denotes the critical mass accretion rate at which the ADAF solution becomes viable. In this case, the thermal emission state for the standard accretion disc is applicable. By decreasing the mass accretion rate to below $\dot{M}_{\rm crit}$, both the accretion disc and ADAF model become important. The accretion disc exists at larger radii, while the ADAF appears at smaller radii. The state of disc-plus-ADAF, the intermediate emission state, happens when $\dot{M}$ is just below $\dot{M}_{\rm crit}$. By decreasing $\dot{M}_{\rm crit}$, the ADAF expands more and BHB emission switches to the hard emission state.

Although this model is consistent with many observations, it has some limitations. For instance, it does not explain the SPL state. The model also does not account for strong flares, powerful low-frequency QPOs and radio emission from most BHBs.

Also recent observations, which provide evidence of existing accretion discs in the low-hard state (Miller et al. 2006; Rykoff et al. 2007; Tomsick et al. 2008; Wilkinson & Uttley 2009; Reis et al. 2009, 2010), contradict the ADAF model. Suggestion from these observations is that the existing accretion disc is not the main characteristic of the transition between low/hard state and

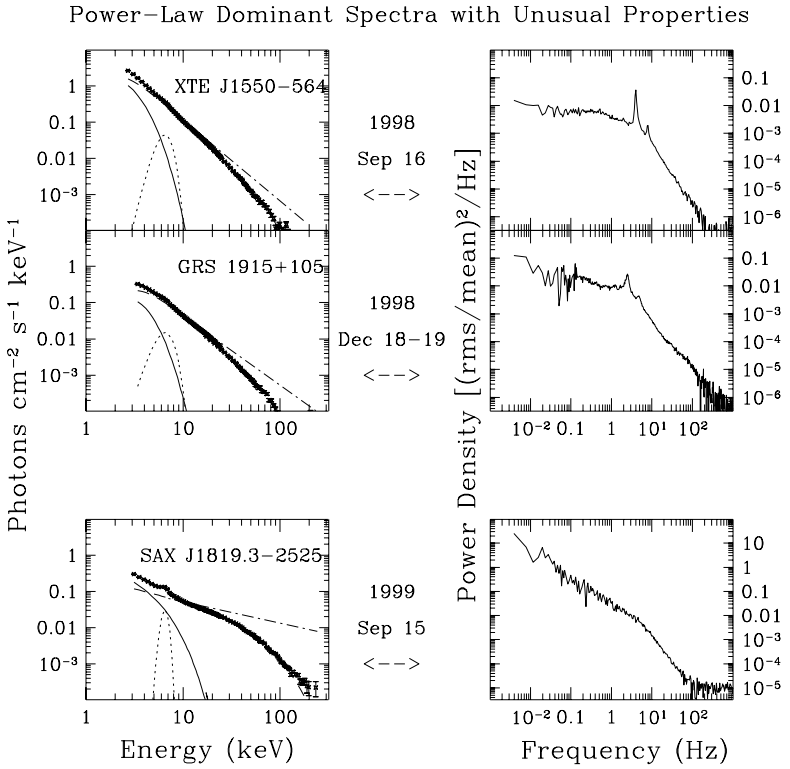


Figure 2.8: *Spectra of three BHBs that cannot be classified in the four distinct emission states and therefore must be grouped in the intermediate states.(McClintock & Remillard 2006).*

the high/soft one. Studying black hole GX 339 - 4 in the hard state by Suzaku and the Rossi X-ray Timing Explorer that extend iron line studies to 0.14% L_{Edd} , Tomsick et al. (2009) have shown that R_{in} increases by a factor of >27 over the value found when the source is bright.

The first section of this Chapter was devoted to a review of the standard accretion disc, or so called α-disc model. We showed how, when combined with the assumption that the disc radiates as a black body (with a temperature depending on radius), this model results in the Multi-Colour Disk (MCD) spectrum. We then discussed how this model is realized in the fitting of X-ray spectra, specifically using the XSPEC program.

However, it has become clear that the α-disc model is not able to successfully explain the physics of accretion observed in all cases. This motivated the development of the Advection-Dominated Accretion Flow (ADAF) model, first proposed in 1994, and which we discussed next. This model provides a superior fit to the spectra of many black hole systems, especially those in quiescence.

Furthermore, we have seen that the various emission states of black hole binaries can be characterized based on a combination of their spectral and timing properties: these range from the Quiescent to Very High states, as the accretion rate increases. Finally, We discussed the comparison

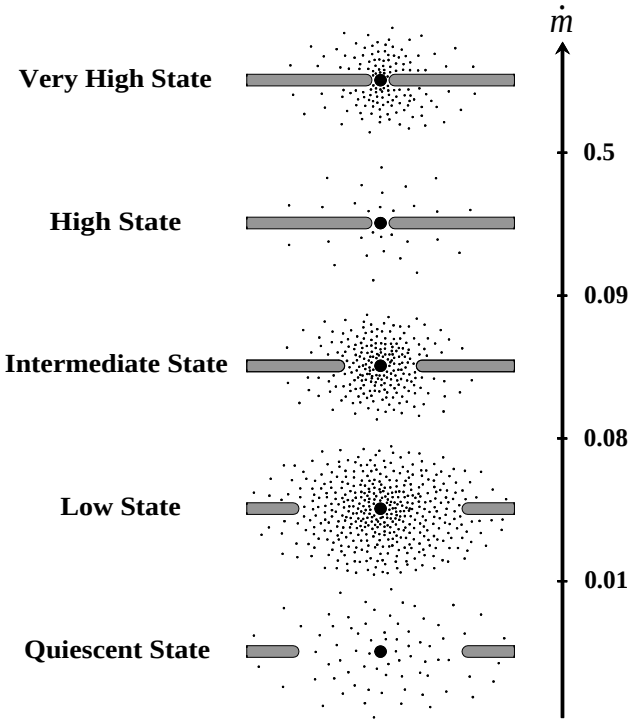


Figure 2.9: *Configuration of the different spectral states in BHBs. The abbreviations on the right panel are as follows: Thermal State (TS), Intermediate State (IS), Hard State (HS), Quiescence State (QS). Due to the mysterious nature of steep power law,Narayan & McClintock (2008) exclude this state from the model.*

between the quiescence of neutron star XRBs and black hole XRBs.

3

Instrumentation & X-ray Data

3.1 X-Ray Telescopes

It was a long time from November 1895 when Röntgen discovered X-rays, to December 1970 when the first X-ray satellite, *Uhuru*, was launched. The fact that X-rays are not able to penetrate even the thin layer of the Earth's atmosphere necessitates the launching of X-ray detectors beyond the atmosphere of the Earth, in order to detect X-rays from cosmic sources.

X-rays can be focused using grazing incidence mirrors. For a very smooth surface with an incidence angle $< 1°$, the reflection efficiency is close to 1. In 1952, Hans Wolter invented three possible configurations for X-ray telescopes which are named after him, **Wolter mirrors**. The most useful configuration for an X-ray telescope is the **Wolter type I**. In this type of mirror, an X-ray hitting a parabolic smooth surface reflects onto a hyperbolic mirror. Figure (3.1)[1] shows

[1]Taken from http://chandra.harvard.edu/graphics/resources/illustrations/cxcmirrors-72.jpg.

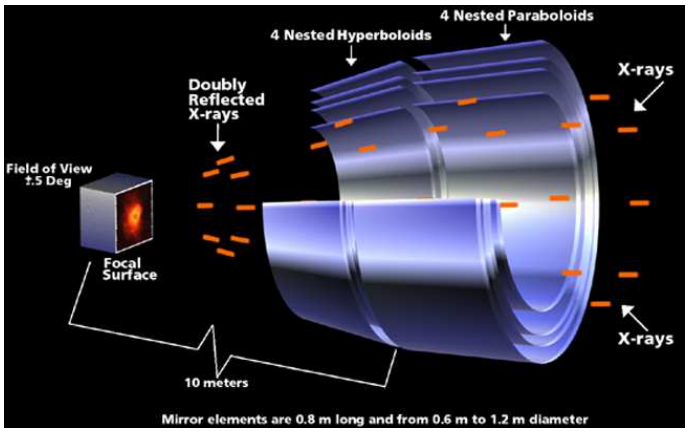


Figure 3.1: *Wolter type I mirror used in Chandra.*

the geometry of Chandra with its Wolter type I mirror. The X-ray mirrors in XMM-Newton and Swift (XRT) are also Wolter type I. The Wolter type II design consists of a paraboloid and a hyperboloid which is placed in the paraboloid mirror. The third type includes a paraboloid followed by an ellipsoid on the outside.

A short summery of the three X-ray telescopes whose data have been used in this thesis is given in the following subsections. General information is summarized in table 3.1.

3.1.1 Chandra

Chandra (formerly known as AXAF), launched in 1999 and is still in operation, is comprised of imaging and grating spectroscopy detectors.

The **Advanced CCD Imaging Spectrometer (ACIS)** consists of 10 CCD chips, four in the imaging array (ACIS-I) and six in a linear array for spectroscopy (ACIS-S). The configuration of ACIS is shown in Fig. 3.2[2]. Each of the ten CCD chips has 1024 × 1024 pixels and an image scale of $0.5''$ per pixel (for an on-axis source), therefore the field of view of ACIS-I and ACIS-S is $\sim 16' \times 16'$ and $\sim 8' \times 50'$, respectively. The energy range is 0.2-10.0 keV. ACIS-S can be used with a grating too.

The **High Resolution Camera (HRC)** is a microchannel camera for 0.1-10.0 keV. HRC includes an imaging camera, HRC-I, with a field of view of $\sim 30' \times 30'$ and spectroscopic detectors, HRC-S, which is designed for soft X-ray spectroscopy with $\sim 6' \times 100'$ field of view covers the Low Energy Transmission Grating (LETG) dispersion pattern from 0.08 to 2.0 keV. The configuration of the HRC cameras are shown in figure 3.3 [3] . The High Energy Transmission Grating (HETG)

[2]Image from http://cxc.harvard.edu/proposer/POG/html/chap6.html#chap:acis
[3]Taken from http://cxc.harvard.edu/proposer/POG/html/chap7.html#fg:hrc-layout

	Angular Resolution	Focal Length	Collecting Area	Sensitivity ($\mathrm{erg\,cm^{-2}\,s^{-1}}$)	Orbit Height (km)	Orbital Period	Launch Date	Weight (kg)
Chandra	$0.5''$	10 m	0.04 $\mathrm{m^2}$	9×10^{-16}	16,000 to 133,000	64.2 hrs	1999	4790
XMM-Newton	$6''$	7.5 m	4300 $\mathrm{cm^2}$	10^{-15}	7,000 to 114,000	48 hrs	1999	3800
Swift	$18''$	381 cm	110 $\mathrm{cm^2}$	2×10^{-14}	600	$\sim$ 90 min	2004	1470

Table 3.1: *General information of three X-ray telescopes which have been used in this thesis.*

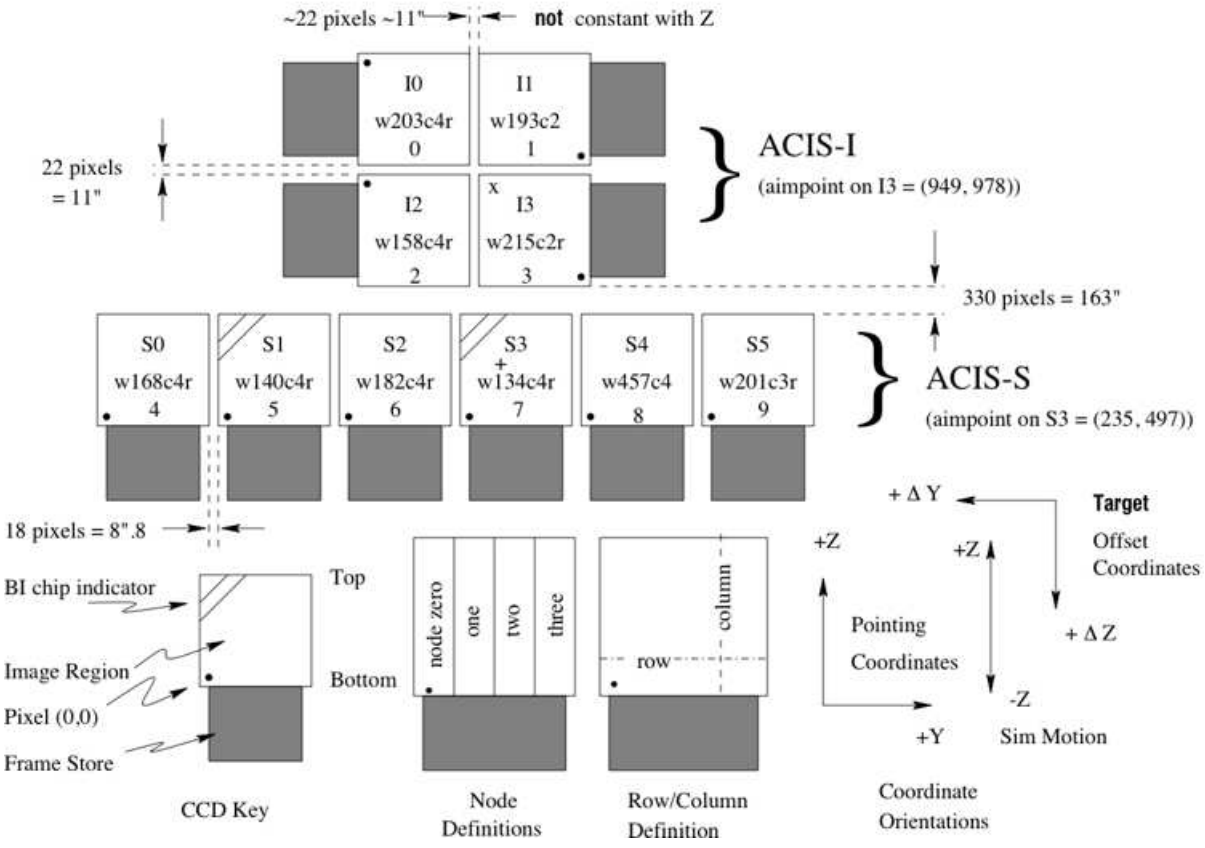


Figure 3.2: *Configurations of ACIS/Chandra.*

operated together with ACIS-S covers higher energy, 0.4 keV and 10.0 keV.

3.1.2 XMM-Newton

The **X-ray Multi-Mirror Mission - Newton (XMM-Newton)**, which was launched shortly after Chandra in 1999, is designed to maximize the effective area (3×1550 cm^2), particularly at higher energies. XMM-Newton consists of three separate co-aligned Wolter type I telescopes, each one has 58 nested coaxial mirrors (see Fig. 3.4a [4]). The configuration of XMM-Newton is shown in Fig. 3.4b[5].

The main detector is the **European Photon Imaging Camera (EPIC)**, consisting of two Metal-Oxide-Semiconductors (MOS) and one back-illuminated (PN) CCD. The first two are optimized for soft X-ray and the third is suitable for detecting hard X-rays. Using EPIC, the field of view of XMM-Newton is over $30'$.

[4]Taken from http://xmm.esac.esa.int/external/xmm_user_support/documentation/technical/Mirrors/
[5]Taken from http://heasarc.gsfc.nasa.gov/docs/xmm/xmmhp_gal_hard_schem.html

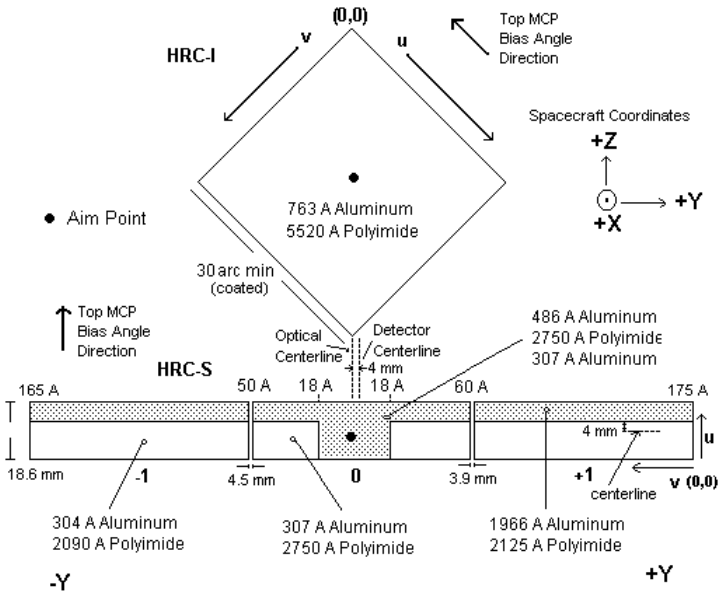
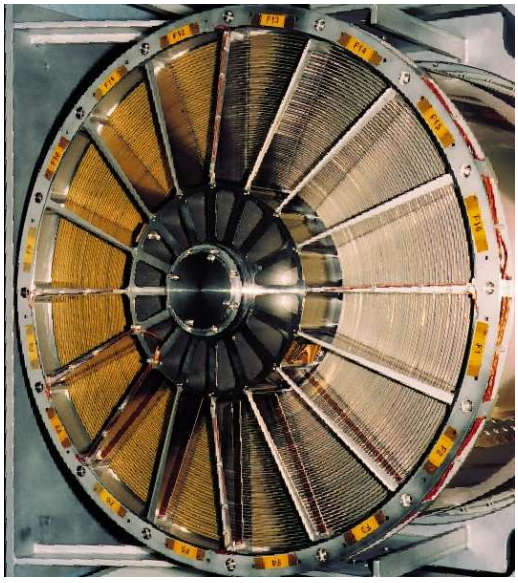
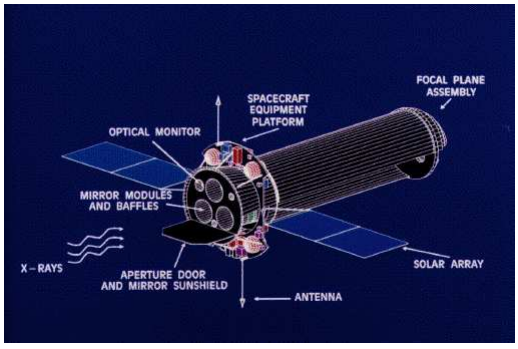


Figure 3.3: *Configuration of HRC/Chandra*



(a) 58 nested coaxial telescope in XMM-Newton



(b) Configuration of XMM-Netwon

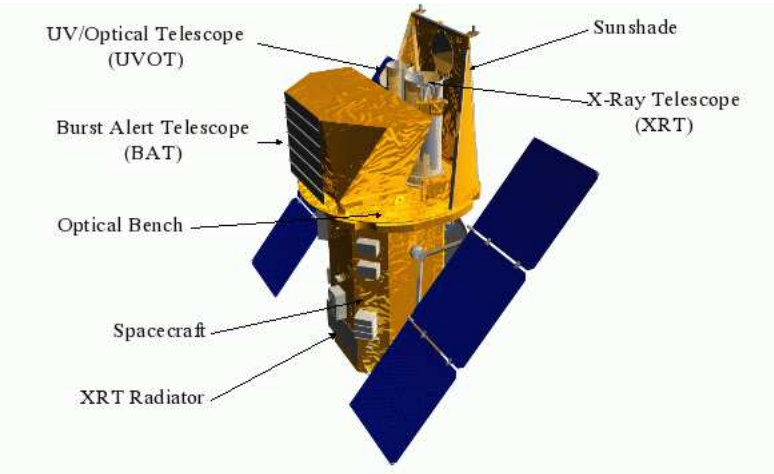


Figure 3.4: *Schematic configuration of Swift*

The EPIC-MOS cameras are equipped with Reflection Grating array (RGA) and provide simultaneous spectra.

3.1.3 Swift

The Swift observatory (shown in figure 3.4[6]) is designed to detect, observe and measure the flux and spectra of Gamma-Ray Bursts (GRBs) and their afterglow and was launched in 2004. The **X-Ray Telescope (XRT)** is used to rapidly point to the burst point which the **Burst Alert Telescope (BAT)** has found.

The mirror of the XRT is a Wolter type I mirror operating in 0.3 to 10 keV energy range, with angular resolution of $\sim 18''$ and $23.6' \times 23.6'$ field of view. It uses a copy of the 600 $\times$ 600 pixel EPIC camera in XMM-Newton.

Besides X-ray detectors, Swift has been equipped with the **UV/Optical Telescope (UVOT)**. UVOT has a 2048 $\times$ 2048 pixel ccd and is sensitive to wavelengths in the range of 170-600 nm.

3.2 X-Ray Data

In contrast to many instruments for longer wavelengths which measure integrated flux, X-ray detectors measure individual photons. Since X-ray photons have relatively large energies, they can be easily detected. Also, the low flux makes it easy to count them.

The number of observed counts, C(X, Y, PI), in a given pixel and PI bin comes from integrating the source flux, $S(X_S, Y_S, E, t)$ for a given position in the sky, $(\mathrm{X_S}, \mathrm{Y_S})$, at energy E and time t.

[6]Taken from http://www.swift.ac.uk/about/instruments.php

In equation (3.1), the source flux unit is photons/cm^2/s/keV/arcmin^2 and R is the instrumental response units of cm^2.

$$C(X, Y, PI) = \iiiint R(X, Y, PI, X_S, Y_S, E, t) \cdot S(X_S, Y_S, E, t) \cdot dX_s \cdot dY_s \cdot dE \cdot dt \tag{3.1}$$

Assuming that the flux of the source does not vary within the region or with time, one can calculate the spectra for the source:

$$C(PI) = \int \Big(\iint \iint\!\!\iint R(X, Y, PI, X_S, Y_S, E, t) \cdot dX_S \cdot dY_S \cdot dX \cdot dY \cdot dt \Big) \cdot S_{spec}(E) \cdot dE \tag{3.2}$$

The instrumental response is usually split between a vector (Ancillary Response File, ARF) with units of cm^2 and a unitless matrix (Response Matrix File, RMF):

$$\begin{aligned} RMF(PI, E) &= \iiint RMF(X, Y, PI, E, t) \cdot dX \cdot dY \cdot dt \\ ARF(E) &= \iint \iiint R(X, Y, X_S, Y_S, E, t) \cdot dX_S \cdot dY_S \cdot dX \cdot dY \cdot dt \end{aligned} \tag{3.3}$$

Therefore, Eq. 3.2 can be rewritten as:

$$C(PI) = T \int RMF(PI, E) \cdot ARF(E) \cdot S(E) \cdot dE, \tag{3.4}$$

where T is the total good exposure time.

Solving Eq. 3.4, a Fredholm integral equation of the first kind, is not easy. The normal approach in X-ray spectroscopy is to guess a possible model spectrum, S(E), and solve the integral. Then, the calculated count number should be compared with the observed count, i.e. C(PI). Statistical methods determine whether the chosen model is suitable or not. The goodness of the fit, χ^2, for N-1 degrees of freedom is defined by

$$\chi^2 = \sum_i^N \frac{(X_i - M_i)^2}{M_i} \tag{3.5}$$

where X_i and M_i are the observed and predicted count number. For low count sources, C-statistic,

named after Cash who introduced this statistic (Cash 1979), is usually used:

$$C = 2\sum_{i}^{N}(M_i - X_i \ln M_i). \quad (3.6)$$

If the goodness of the fit is not acceptable, another model should be investigated.

Data from an observatory is originally obtained in a basic format and needs to be reduced first. Then the spectrum can be extracted (C(PI) in Eq. 3.4). The relevant software for each telescope's data provides the specified tasks to enable the spectrum to be extracted. Furthermore, the ARF and the RMF can be produced using the software. In addition "ready-to-use" response files may also be available. The following subsections are devoted to a brief practical review of data reduction and spectrum extraction of a point source detected using Chandra, XMM-Newton and Swift observations.

XSPEC is an X-ray spectral fitting package which can be used to estimate the goodness of a proposed model. The software solves Eq. 3.4 and provides the user with the χ^2 or C-statistic of the fit. An object oriented Python version of XSPEC, called PyXspec [7], has been developed and recently released. PyXspec is used throughout this thesis. An example of a PyXspec script which has been used during this research is given in appendix B.

3.2.1 X-ray data from Chandra

Chandra data can be retrieved either from the Chandra data archive [8] or HEASARC website[9]. The **Chandra Interactive Analysis of Observations (CIAO)** (Fruscione et al. 2006) is the software package used to analyze data from Chandra (and other X-ray telescopes).

Even though data sets are reduced by the software prior to release, the user is advised to reduce the data again before any scientific use. In CIAO v 4.4, a fully automated script called **chandra_repro** [10] must be used to reprocess the Chandra dataset.

Using the reduced data, the spectrum of a point source in Chandra data can be extracted using **specextract** [11] task. Option **binspec** sets the minimum number of counts in each bin. This task produces binned spectrum, RMF and ARF files which on the next step, must be used as the input to XSPEC. My python script for this task is given in appendix A.1.

[7] http://heasarc.nasa.gov/xanadu/xspec/python/html/index.html
[8] http://cda.harvard.edu/chaser/
[9] http://heasarc.gsfc.nasa.gov/docs/archive.html
[10] http://cxc.harvard.edu/ciao/ahelp/chandra_repro.html
[11] http://cxc.harvard.edu/ciao/ahelp/specextract.html

Software / Task Name	CIAO	SAS	HeaSoft
Data Reduction	chandra_repro	epproc	xrtpipeline
Extract Spectrum	specextract	eveselect rmfgen arfgen	xselect - xrtmkarf
Detecting Pile up	pileup_map	epatplot	xselect

Table 3.2: *A summary of tasks for data processing.*

3.2.2 X-ray data from XMM-Newton

Observational data from XMM is obtainable from the XMM data archive [12] or HEASARC website .

The **Science Analysis System (SAS)** is the software package designed to work with XMM-Newton data. To reprocess raw data from EPIC, **emproc** and **epproc** are the appropriate tasks for MOS and PN data [13], respectively.

To extract the spectrum of a point source in PN data, **evselect** [14] is used. Two other tasks, **arfgen** and **rmfgen**, must be employed afterwards to generate the associated ARF and RMF. Before loading the spectrum data into XSPEC, data must be binned to a suitable minimum count number per bin using **grappha** [15].

The Python scripts which I wrote to reduce the data and extract spectrum are given in appendix A.2.

3.2.3 X-ray data from Swift (XRT)

Data from XRT observations are downloadable from the HEASARC website. To re-reduce data and generate event files from XRT, a task called **xrtpipeline** is available as a part of HEAsoft [16]. In the next step, an image must be made from the observations using **xselect**. The Python script used to generate an image is presented in appendix A.3.1.

Filtering the point source in the image again by using **xselect**[17] extracts spectra. **xrtmkarf** produces the ARF. RMF is ready in the software. Finally, data should be binned using **grappha**. My python script is given in appendix A.3.2.

[12] http://xmm.esac.esa.int/xsa/index.shtml
[13] http://xmm.esac.esa.int/sas/current/documentation/threads/EPIC_reprocessing.shtml
[14] http://xmm.esa.int/sas/current/documentation/threads/PN_spectrum_thread.shtml
[15] http://heasarc.nasa.gov/lheasoft/ftools/fhelp/grppha.txt
[16] http://heasarc.nasa.gov/lheasoft/
[17] http://www.swift.ac.uk/analysis/xrt/spectra.php

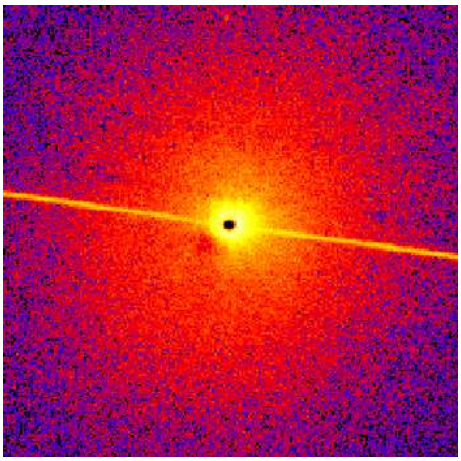


Figure 3.5: *pileup over the threshold (typically 15 keV) is rejected by the software and can be seen as a dark circle.*

3.2.4 Pileup Effect

Pileup may happen in CCD X-ray detectors while observing a source with a strong flux. It occurs when more than one photon arrives within the same detector region in a single frame time. Typically, the electric charge of a single photon is read out from a 3×3 pixel island (refereed to as a region). When pileup occurs, the electric charge of the arrived photons (more than one photon) are mistakenly detected and recorded as the charge of one photon. Therefore, the flux and the hardness of the photon are measured incorrectly.

In the case of very severe pileup, the software on board detects and rejects the piled up photons. As the result, the image contains a small black area where the pileup is particularly serious. Fig. 3.5 shows a Chandra image with piled up photons which are distinguished and rejected automatically [18]. For less severe cases but still very bright sources, the user must examine the data to check for pile up. Each software package has a task to help diagnose piled up pixels, as described bellow:

- Pileup in Chandra (ACIS) data

  A task named **pileup_map** [19] in CIAO is able to roughly distinguish piled up point sources. This task produces a pileup map with the number of counts per frame and any value <0.2 indicates pileup.

  To fix the pileup effect, a model called **pileup** [20] is implemented in XSPEC based on the work of Davis (2001).

- Pileup in XMM-Newton data

[18] Taken from http://cxc.harvard.edu/ciao4.2/why/pileup_intro.html
[19] http://cxc.harvard.edu/ciao/ahelp/pileup_map.html
[20] http://heasarc.nasa.gov/docs/xanadu/xspec/manual/XSmodelPileup.html

In SAS, task **epatplot**[21] is used to determine whether the target point source is affected by pileup or not. If the source is affected by pile up, then the central pixels of the source must be excluded and the spectrum must be extracted from an annulus.

- Pileup in SWIFT (XRT)

  As a rule of thumb, any source with a count rate of $\geq$0.6 count s^{-1} is likely to be affected by pileup in an XRT observations. To determine pileup in XRT data, the Point Spread Function (PSF) of the suspected piled up source must be compared with the expected PSF of a normal (not piled up) source. Moretti et al. (2005) modeled the Swift PSF in the absence of pileup by

  $$\mathrm{PSF(r)} = \left[1 + (\frac{\mathrm{r}}{\mathrm{r_c}})^2\right]^{-\beta} \tag{3.7}$$

  where $\mathrm{r_c} \sim 5.8$ and $\beta \sim 1.55$. This model has been implemented in HEAsoft (called the "king" model). Comparing the centre of the PSF of the point source with the one in the model determines whether the source is piled up or not [22].

  The method used to fix the pileup effect in an XRT observation is similar to the one used for XMM; the spectrum of the point source must be extracted from an annulus, in order to exclude the central pixels which are affected by pile up.

In this Chapter we first discussed the construction of X-ray telescopes, and three X-ray observatories that use this technology Chandra, XMM-Newton and Swift. After demonstrating, in theory, how the instrumental response relates the intrinsic source flux to the observed counts, we then presented a brief overview of the data reduction systems used to reduce the data from the three missions mentioned above. Finally the effect of pileup, which turns out to be significant in the analysis that follows, was discussed in the context of these three missions.

[21] http://xmm.esac.esa.int/sas/current/documentation/threads/epatplot.shtml
[22] http://www.swift.ac.uk/analysis/xrt/pileup.php

Part II

X-ray Transients in M31

4

Soft X-ray Transients in M31 and Optical Follow up

To find and study extra-Galactic XRTs, M31 (Andromeda) seems a very good target. It is the nearest spiral galaxy to us. The distance towards M31 is well determined (780 kpc; Holland (1998)) and therefore the uncertainty in converting flux to luminosity of the SXTs hosted by M31 is negligible. In comparison the distance towards many Galactic sources is more uncertain.

The first X-ray observation of M31 dates back to 1973. Using rocket-borne proportional counters, Bowyer et al. (1974) observed M31 in the energy range of 0.5-5 keV. Shortly after, Giacconi et al. (1974) performed an exposure of M31 with Uhuru. The first imaging X-ray observations of M31 with Einstein were presented by van Speybroeck et al. (1979). Later observations presented by Trinchieri & Fabbiano (1991) detected 108 individual X-ray sources brighter that $5 \times 10^{36}\,\mathrm{ergs\,s^{-1}}$

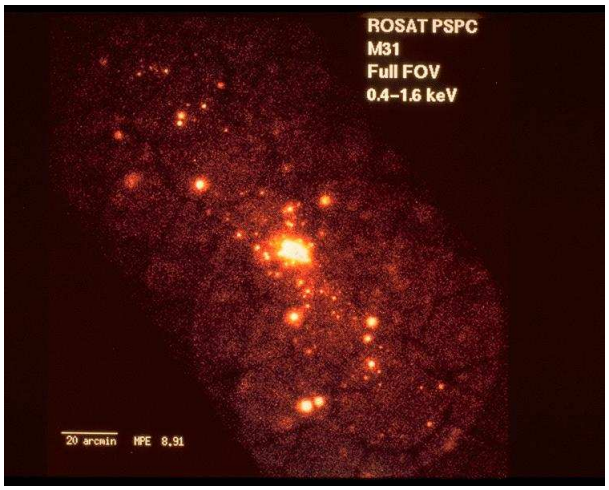


Figure 4.1: *A ROSAT map of M31 of 30 ks exposure (Supper et al. 1997). Most of the bright sources are located in the bulge, only a few are situated in the outer spiral arms.*

in the energy range 0.2-4.0 keV.

Making a $\sim$ 48 ks observation of the bulge region of M31 with ROSAT, Primini et al. (1993) found the three sources which may be transient, compared to the previous Einstein image.

Shortly after the launch of Chandra, Garcia et al. (2000) made the first ACIS observation of M31. Since then, M31 has been numerously observed with Chandra and XMM-Newton. X-ray transient sources hosted by M31 have been discovered and studied (Williams et al. 2005, 2006a; Trudolyubov et al. 2006; Voss et al. 2008).

The distribution of bright sources in M31 is different from those in the Milky way. Early surveys of the entire M31 galaxy with the ROSAT PSPC (Fig.4.1) showed that most of the bright sources are associated with the bulge (Supper et al. 1997) (Fields of view have been limited to 1°. The size of the inner bulge of M31 which is relatively circular bulge is $<\sim 50^{''}$ (Beaton et al. 2007)). These bright sources are thought to be accretion powered XRBs and belong to a population of old stars. The number of sources is more than expected and they are located closer to the nucleus, on average (Seward & Charles 2010, pg. 263). Therefore, regularly observing the bulge of M31 should allow us detect more bright XRBs.

Chandra is ideally suited to this study for example even though the field of view of XMM-Newton is much larger than that of Chandra, its resolution is lower. For comparison, Pietsch et al. (2005) with a 340 ks XMM-Newton exposure, found 896 sources with $L_x \geq 5 \times 10^{34} \mathrm{erg\,s^{-1}}$, while with a roughly 1/15 smaller field of view, using 8 ACIS observations of the central region of M31 ($17^{'} \times 17^{'}$), Kong et al. (2002) found 204 sources with $L_x \geq 2 \times 10^{35} \mathrm{erg\,s^{-1}}$ (1/4 of number of sources detected with XMM-Newton). Thus in order to find faint sources, observing the bulge of M31 with

Chandra is more useful than with XMM-Newton because of the higher resolution. In addition, an exposure of the entire bulge region of M31 is possible with a single Chandra observation.

The work which is the subject of this Chapter consists of Chandra and Hubble Space Telescope (HST) observations of M31. Since the bulge region of galaxies is very populated and luminous the detection of an optical counterpart to an XRT requires very high resolution imaging such as that provided by the HST.

Ideally, in order to identify the counterpart two HST observations are required. The first (hereafter this optical image is called "HST-on") is obtained as soon as possible after a luminous outburst is detected by Chandra: the second (hereafter called "HST-off") is obtained when the XRT has returned to quiescence. Subtracting the HST-off image from the HST-on image should reveal the optical counterpart (see Figure 4.3 for an example).

To identify the optical counterpart we obtain the most accurate position of the source from the X-ray image and compare the two optical images at this position. The method we use to find the most accurate position of the transient source will be explained in Section 4.1.

In the Milky Way, the orbital period of an XRT is usually found once the system has returned to quiescence from optical studies. Unfortunately, due to the large distance between us and M31, the faintness of the counterparts in quiescence and the crowded optical fields do not allow a direct measurement of the optical period. However van Paradijs & McClintock (1994) suggested an empirical relation between X-ray luminosity, optical magnitude and orbital period of LMXBs which can be used to constrain the orbital period instead. This is discussed in section 4.3.

4.1 Estimating the X-Ray Position of an XRT in M31

Since the bulge of a galaxy is a very populated area, finding the most accurate X-ray position of a source is a critical task, in order to allow the identification of a counterpart in other wave bands (e.g. in the optical). One way to achieve this is to use an image of high astrometric accuracy as the reference for the coordinates. For the work presented here, the image of M31 from the Local Group Survey images (LGS; Massey et al. (2006)) has been used.

The recipe used to astronomically calibrate our data is as follows:

- Firstly, using the Chandra image, the list of globular clusters (GCs) in M31 (Galleti et al. 2004) and the LGS image must be displayed and aligned in DS9 [1] (see Fig. 4.2; the positions

[1] http://hea-www.harvard.edu/RD/ds9/site/Home.html

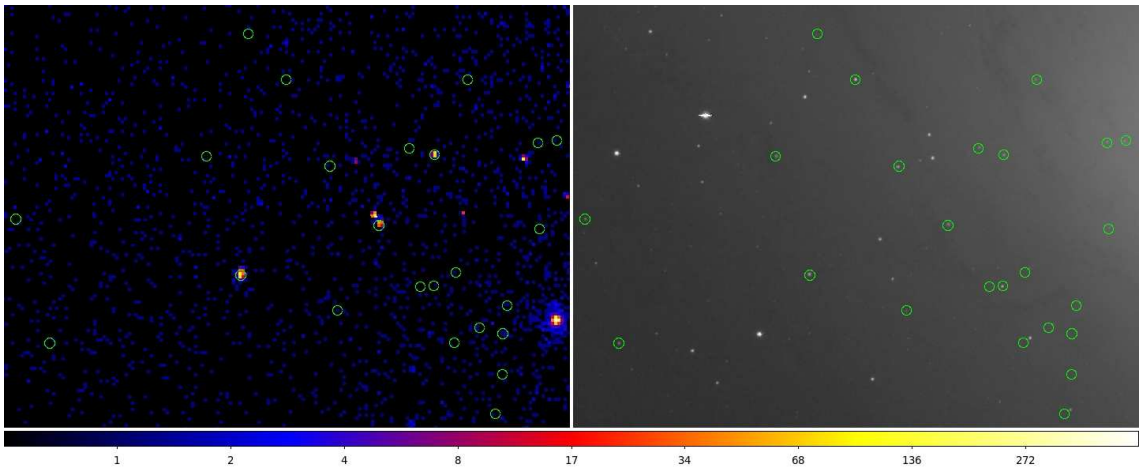


Figure 4.2: *The X-ray and LGS images are displayed in DS9. Position of the globular cluster sources are shown by green circles.*

of the GCs are shown by the green circles). The image coordinates of the GC sources which correspond to an X-ray and optical source must be saved in a text file. A task in IRAF, called **imcentroid** [2] is used to find the best center position of the sources in the images.

- For the next step, the coordinates of the sources in the list must be converted to the sky coordinates (Right Ascension (R.A.) and Declination (Dec.)). This is carried out by using **xy2sky** [3] available in WCStools.

- The output file of xy2sky has 4 columns, the first two are the image coordinates and the next two are the sky coordinates. The sky coordinates of the GC sources in the Chandra image must be replaced with the sky coordinates of the same GC sources in the LGS image. The new file which includes the revised sky coordinates is the input file for the IRAF task **ccmap**[4] which computes the plate solution for the Chandra image and updates the image with the more accurate positions.

The revised Chandra image can now be used to estimate the most accurate X-ray position of the new transient. Using **imcentriod** with the image coordinates of the X-ray transient source, the central position of the transient from the revised Chandra image is obtained. Using **xy2sky** converts the coordinates to R.A. and Dec. which is the updated X-ray position of the transient.

The two HST images (HST-on and HST-off) must also be corrected using the LGS image, following the above steps. A detailed discussion of the HST image analysis is given in the next

[2] http://stsdas.stsci.edu/cgi-bin/gethelp.cgi?imcentroid
[3] http://tdc-www.harvard.edu/wcstools/xy2sky/
[4] http://stsdas.stsci.edu/cgi-bin/gethelp.cgi?ccmap

section.

4.2 Optical Analysis

In this project, the HST images are taken in the B-band using the filter F435W of Advanced Camera for Surveys (ACS). Each observation set includes 4-8 flat-fielded (FLT) images and one drizzled (DRZ) image. The FLT images are corrected for the instrumental effects (dark, bias and flat). The DRZ in available in each dataset is performed by the pipeline but user can re-produce it using Multidrizzle[5]. The DRZ image is the final product of which combines the FLT images, subtracts the sky background, rejects the cosmic rays and finally scales the image by intensity (electron s^{-1}). Since the cosmic rays are rejected in producing the DRZ image, the DRZ image has better quality and is more appropriate for subtracting HST-on and HST-off images, but for accurate photometry (for example using **PHOT** [6] or **DAOPHOT**), using the FLT images is better since an accurate measurement of the sky is needed for photometry.

After correcting the two HST images, comparing HTS-on and HST-off at the position of the X-ray transient source may reveal a counterpart candidate. It is possible, for example, to subtract the two DRZ images (or FLT images), but they must first be aligned. Using **wcxymatch**[7], the user selects one of the HST images as the reference and then the task finds the common sources in the other image. The list of sources is recorded automatically in a file. Next, another task called **geomap**[8] computes the spatial transformation and on the last stage, **Geotran**[9] transforms the second image to match the reference image, while **imarith** [10] subtracts the two images arithmetically. I wrote a Python script to automate these steps (given in appendix C). The right panel in Fig. 4.3 has been produced using this script.

Next, I carried out photometry on the subtracted image. The counts number of the detected star can be converted to Vega B magnitude via

$$B = -2.5 \log[\text{counts/s}] + 25.76,$$

where, using the values of PHOTLAM and PHOTZPT stored in the headers of of the HST images,

[5] http://stsdas.stsci.edu/multidrizzle/
[6] http://stsdas.stsci.edu/cgi-bin/gethelp.cgi?phot
[7] http://stsdas.stsci.edu/cgi-bin/gethelp.cgi?wcsxymatch.hlp
[8] http://stsdas.stsci.edu/cgi-bin/gethelp.cgi?geomap
[9] http://stsdas.stsci.edu/cgi-bin/gethelp.cgi?geotran
[10] http://stsdas.stsci.edu/cgi-bin/gethelp.cgi?imarith

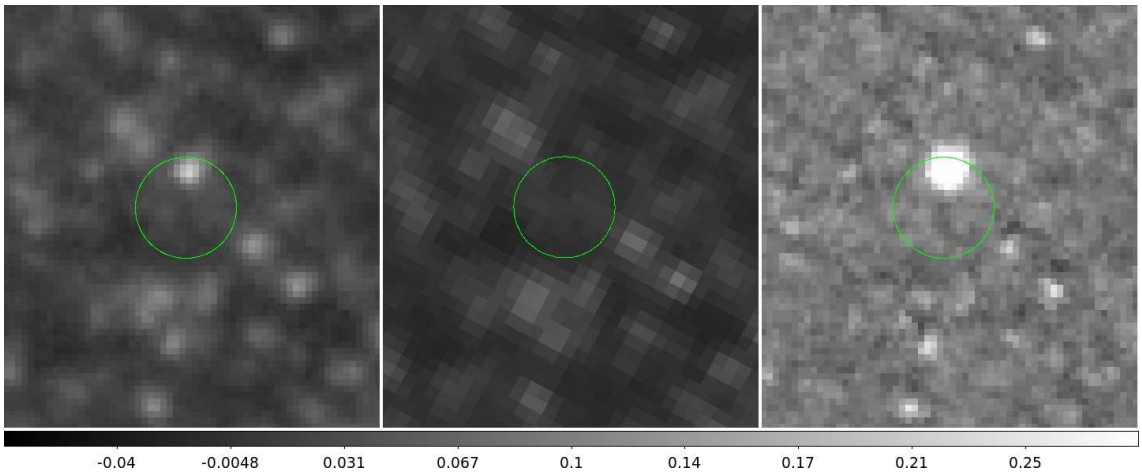


Figure 4.3: *From left to right: HST-on, HST-off and subtracted image using IRAF.*

the constant term in the equation above is calculate from [11]

$$-2.5\log(\text{PHOTFLAM}) + \text{PHOTZPT}.$$

In the case which no source is detected, we summed the counts within a circle of 2 pixel radius at position of X- ray source from the FLT images, yielding $C_{\rm tot}$ counts over T seconds, which can be converted to a B magnitude using the expression above.

In order to use the empirical relations to estimate the orbital period (explained in Sec. 4.3), the absolute magnitude in the V band will be needed. To calculate this, we assume that this source had a B-V of -0.09± 0.14, an average of the values to be found in the LMXB catalogue of Liu et al. (2001). We must next correct for the effect of optical extinction towards this source. This extinction is primarily due to the absorption and scattering of dust along the line of sight between the emitter and observer and steadily increases with decreasing wavelength (Cardelli et al. 1989). The effect of extinction on M31 is not severe. For example, the nucleus of M31 suffers $\leq$ 2 mag of visual extinction (Garcia et al. 2000) whereas the nucleus of Milky way (Sagittarius A*) is obscured by $\sim$ 30 mag (Morris & Serabyn 1996). Systematic studies of X-ray scattering halos around Galactic LMXBs have shown that $A_V \sim N_H/1.8 \times 10^{21}$ atom cm^2 (Predehl & Schmitt 1995) while $\frac{A_V}{E(B-A)} \sim 3$ (Cardelli et al. 1989); hence

$$A_B \sim N_H \times (1 + 1/3)/1.8 \times 10^{21}.$$

[11] http://www.stsci.edu/hst/acs/analysis/zeropoints

So, for $N_H = 6 \times 10^{20}$ atom cm^{-2} the calculated value for foreground extinction toward the source is $A_B \sim 0.44$. Accounting for the optical extinction and the distance modulus towards to M31 (24.47; Stanek & Garnavich (1998)), one can write

$$M_{\rm V} = B + 0.09 - A_{\rm B} - 24.47. \tag{4.1}$$

4.3 Estimating Orbital Period

Early studies suggested that the absolute visual magnitude of the optical counterpart to LMXBs, M_v, is proportional to the orbital period (Chevalier et al. 1985; Nieto et al. 1990; Anderson et al. 1993). Gathering the parameters of 18 Galactic LMXBs (soft X-ray transients and Z-sources), van Paradijs & McClintock (1994) (hereafter VPM94) suggested an empirical relation

$$M_{\rm V} = 1.57\,(\pm 0.24) - 2.27\,(\pm 0.32)\log\Sigma \tag{4.2}$$

where

$$\Sigma = (L_{\rm X}/L_{\rm Edd})^{1/2}\,(P/1\,{\rm hour})^{2/3}$$

and the Eddington luminosity is assumed $L_{\rm Edd} = 2.5 \times 10^{38}{\rm erg\,s^{-1}}$.

As only two of the sources used to derive VPM94 relation were black hole systems, Moss et al (2013, in preparation) next obtained data from a sample of transient Galactic black holes near the maximum of their outburst, for which optical observations were also available, supplemented by a smaller number of persistently bright systems. These data yield

$$M_{\rm V} = 0.84(\pm 0.30) - 2.36(\pm 0.30)\log\Sigma \tag{4.3}$$

This relationship was obtained for systems exclusively in the high soft (thermal) state, in the 2-10 keV energy range. In the next section, we use this relation to constrain the orbital period of a particularly bright transient source in M31.

ObsID	Date	Exposure (ks)
11276	08-Dec-2009 T20:52:03	3.9
00031518013	22-Dec-2009 T00:56:33	6.3
10719	27-Dec-2009 T19:54:35	4.1
11277	01-Jan-2010 T19:52:00	4.1
00031518014	27-Jan-2010 T01:06:21	4.6
00031518015	02-Feb-2010 T08:26:23	9.0
11278	04-Feb-2010 T06:22:55	3.9
11279	05-Mar-2010 T14:11:11	4.1
11838	27-May-2010 T14:06:45	3.9
11839	23-Jun-2010 T14:29:42	3.9
00031255012	06-Jun-2010 T10:31:04	3.9
00031255013	09-Jun-2010 T09:00:14	4.1
00031255014	12-Jun-2010 T00:55:19	3.9
00031255015	15-Jun-2010 T10:38:02	2.4
00031255016	18-Jun-2010 T01:27:35	4.1
00031255018	24-Jun-2010 T00:34:14	4.4
11840	20-Jul-2010 T20:41:29	4.9
11841	24-Aug-2010 T10:41:18	4.9

Table 4.1: *Details of our Chandra ACIS-I and SWIFT observations.*

4.4 Study of a Very Bright SXT in M31[12]

4.4.1 Discovery

As part of Chandra's long term monitoring of M31, a new source, CXOM31 J004253.1+411422, was discovered on 17 December 2009. We followed the criteria described by Kong et al. (2002) to give the source the short name r2-75. Initially observed with the Chandra High Resolution Camera (HRC-I), the source's luminosity of $(4.6 \pm 0.1) \times 10^{39} \mathrm{erg\,s^{-1}}$ was inferred by using a Swift spectrum obtained five days later, normalized to the HRC count rate (Henze et al. 2009).

We have obtained nine X-ray images of the source with the Chandra Advanced CCD Imaging Spectrometer (ACIS) camera. ObsIDs 10719, 11838, 11839,11840 and 11841 were guaranteed time observations (PI: S. Murray). Anticipating the possible detection of bright transients, an *alternating exposure mode* was used to reduce the effect of pileup. In this observation mode each sixth frame has 0.6 seconds of exposure instead of 3.2 seconds. Details of our Chandra observations are given in Table 4.1.

Our first task was to estimate the most accurate position for the new source, as explained in section 4.1. The final corrected position of r2-75 is R.A.= 00:42:53.2± 0.01, decl.= +41:14:22.6± 0.1 in J2000. This position is consistent with that found by Kaur et al. (2012) after including the errors in matching to the 2MASS coordinate system used there.

[12]The results of this section has been published in Nooraee et al. (2012).

ObsID	Count rate per frame	
	0.6 s frame time	3.2 s frame time
10719	0.55	0.29
11277	0.39	0.41
11278	0.25	0.56
11838	–	0.18
11839	–	0.07

Table 4.2: *The count rate per frame on the pileup map from each ACIS observation. A count rate equal to or greater than 0.2 indicates pileup.*

4.4.2 X-ray Observations with Chandra

Since the source is so bright, we immediately checked the ACIS-I data for the effects of pileup (see page 52). It is clear from these maps that three ACIS observations (ObsIDs 10719, 11277 and 11278) were piled up. In Table 4.2, we provide a summary of the count rate per frame on the pileup maps for the short (0.6s) and the longer (3.2s) frame times for each ACIS observation.

We extracted the X-ray spectrum of the source from each of the ACIS images using the CIAO task psextract. We binned each spectrum in energy so that each bin contained $\gtrsim$10 counts to allow for standard χ^2 statistics. Using XSPEC, we fitted absorbed power law and absorbed disk black body models, in addition to a pile-up model, where appropriate. We assumed the grade morphing parameter (denoted by α in the pileup model) is 0.5 , which is the value suggested in the CIAO documentation [13]. We fitted a pileup model with frozen $\alpha = 0.5$) and a disk black body model to the shorter exposure time data, taken with the alternating readout mode.

The pileup during ObsId 10719 was so severe that not even the spectrum constructed from 0.6s exposures was usable. Indeed, the count rate per frame for this observation is smaller for the 3.2 s exposures than the 0.6 s exposure; hence, the pileup was so severe that most photons were rejected. Furthermore, r2-75 fell between chips during observations 11279 and 11840. We removed all three observations from our sample.

4.4.3 X-ray Observations with Swift

Seven observations of r2-75 were made with Swift during 2010 June, taken at three-day intervals. Unfortunately, the 2010 June 21 observation had an exposure time of just 25 seconds, so this observation was ignored. Details of Swift observations are given in Table 4.1.

We expect significant pile-up at around 0.7 count s^{-1} for the XRT in pc mode (Moretti et al.

[13] http://cxc.harvard.edu/ciao/download/doc/pileup_abc.pdf

2005) (see page 53 for more explanation). We checked our Swift observations for pile-up. The radial profile of r2-75 was well described by the King function, with no sign of the under-luminous core that signifies pileup. We therefore conclude that r2-75 was free from significant pileup in all of the Swift observations.

The data were analyzed with **xselect** version 2.4a. We used the recommended source extraction radius of $47''$ as this contains around 90% of the source photons. We also extracted background data from a similarly sized, nearby region of blank sky. The light curves of each Swift observation were consistent with constant intensity. Spectra of bright observations were analyzed with XSPEC version 12.6, with a grouping that yielded a minimum of 20 photons per bin.

The angular resolution of a telescope is the smallest angle between nearby objects that can be clearly distinguished by the telescope. When the angular resolution is poor, source confusion happens when two or more close objects appear as one object in the image of a telescope. In other words, when the distance between objects is smaller than the telescope's angular resolution, the telescope cannot resolve those objects individually. Compared with the high angular resolution of Chandra ($0.5''$), Swift's poor angular resolution ($18''$) may result in confused sources. Checking the first Chandra image from r2-75 shows that the closest source to it is located at a radius of $\sim 85''$. Therefore, spectrum extracted within a radius of $47''$ in Swift images (as explained above) does not suffer from the source confusion effect.

4.4.4 Optical Observations with HST

As part of our program to find optical counterparts to bright M31 X-ray transients, we obtained HST/ACS data at the position of the new transient, during its outburst, on 21-Jan-2010, and once again when the source returned to quiescence on 20-Jul-2010. Our observations were taken using the standard ACS box 4-point dither pattern to recover the highest possible spatial resolution. Both of these observations were obtained with the F435W filter.

We used PyRAF task multidrizzle to generate our images, yielding an image of resolution $0.025''$ pixel^{-1}. The task also removes cosmic ray events and geometric distortions, whilst combining the dithered frames together into one final image.

We aligned all of the *HST* images to the LGS coordinate system with ccmap using stars common to both data sets. The resulting alignment had rms errors of $0.04''$ (less than 1 ACS pixel).

Date	ObsID	T	Model	$N_H/10^{20}\mathrm{cm}^{-2}$	Parameter	χ^2/dof	L_X
08-Dec-2009	11276		PL	6	Γ= 1.7	–	< 0.17
22-Dec-2009	00031518013	0	DBB	6.1±1.7	$T_{\rm in}$= 1.15±0.06 keV	124/125	175±7
01-Jan-2010	11277	10	Pileup × DBB	6	$T_{\rm in}$= 1.04 ± 0.17	14.3/12	110 ± 36
27-Jan-2010	00031518014	36	DBB	6	$T_{\rm in}$=0.82±0.06 keV	33/35	50±4
04-Feb-2010	11278	44	Pileup × DBB	6	$T_{\rm in}$= 0.72± 0.17	5.92/8	37.6 ± 8.7
22-Feb-2010	00031518015	62	DBB+PL	6	$T_{\rm in} = 0.52^{+0.14}_{-0.10}$ keV, $\Gamma = 2.1^{+1.0}_{-1.3}$	30/37	35±2
27-May-2010	11838	156	PL	6	Γ= 2.0 ± 0.14	34/28	8.7 ± 1.0
6-Jun-2010	00031255012	166	PL CF	6	Γ=2.5	NA	13±2
9-Jun-2010	00031255013	169	PL CF	6	Γ=2.5	NA	8.8±1.2
12-Jun-2010	00031255014	172	PL CF	6	Γ=2.5	NA	7.9±1.2
15-Jun-2010	00031255015	175	PL CF	6	Γ=2.5	NA	5.2±1.6
18-Jun-2010	00031255016	178	PL CF	6	Γ=2.5	NA	7.6±1.2
23-Jun-2010	11839	183	PL	6	Γ= 2.3±0.29	10.9/10	5.2 ± 1.3
24-Jun-2010	00031255018	184	PL CF	6	Γ=2.5	NA	7.2±1.2
24-Aug-2010	11841		PL	6	Γ= 1.7	–	< 0.16

Table 4.3: *Spectral fits and unabsorbed 0.2-10.0 keV luminosities of r2-75 in units of* $10^{37}\mathrm{erg\,s}^{-1}$. *Parameters which have been frozen are listed without uncertainties. T shows the time corresponding time to the horizontal axis in Figure 4.5.*

4.4.5 Results

The upper limit from our Chandra observation taken on 2009 Dec 08 (ObsID 11276) is $< 0.17 \times 10^{37}\mathrm{erg\,s^{-1}}$. We calculated the upper limits by assuming a power law spectrum of photon index 1.7 and a hydrogen column $N_H = 6 \times 10^{20}\mathrm{cm^{-2}}$. In addition, we combined 55 Chandra ACIS observations of this field yielding an image with a net ACIS exposure of 240 ks. The 3σ upper limit from this merged image is $9.6{\times}10^{-5}$ cts/s, corresponding to an intrinsic 0.2-10.0 keV luminosity of $1 \times 10^{35}\mathrm{erg\,s^{-1}}$, assuming the above values for the photon index and hydrogen column density. The column we have used for these fits, $6{\times}10^{20}\mathrm{cm^{-2}}$, is the Galactic foreground absorption value towards M31, consistent with our best estimate of the column towards r2-75 obtained on 2009 Dec 22. We fixed the column to this value for all the other spectral fits described in what follows.

The first two Swift observations after the outburst, in 2009 December (ObsID 00031518013) and 2010 January (ObsID 00031518014), are well described by a disk black body model, with $\chi^2/\mathrm{dof} < 1$.

For the two first Chandra observations (ObsIDs 11277 and 11278), freezing N_H and fitting the pileup model and a disk black body model on the shorter frame time observations gave more reasonable results than for the longer frame time observations.

The best disk black body fit to the 2010 February data (ObsID 00031518015) yields $\chi^2/dof = 51/39$; this is an acceptable fit, but it systematically underestimates the high energy spectrum. Therefore, we added a power law component to represent unsaturated inverse comptonization of cool photons on hot electrons in the accretion disk corona. The best fit yielded $\chi^2/\mathrm{dof} = 31/37$; F-testing [14] showed that this improvement was significant at the 99.99% level, hence we adopted this model. This evolution is expected for black hole transients going from the high state to the intermediate state during the decay of the outburst.

Fitting a power law model to our next ACIS observation (ObsIDs 11838) gave more reasonable result than a disk black body model. For the 2010 June Swift observations, there were too few photons for reliable spectral fitting; for these observations, we converted from intensity to source flux using an assumed model. Using this assumption, a wide range of changes in the luminosity is not expected, e.g. for a faint source assuming $\Gamma = 2.5$ leads to $L_X = 1.8 \times 10^{37}\mathrm{erg\,s^{-1}}$ whereas assuming $\Gamma = 2.3$ gives $L_X = 1.9 \times 10^{37}\mathrm{erg\,s^{-1}}$. We determined the best model to use by simul-

[14] F-test can be used to compare the fit results of two models when one of these models has only one extra model component, e.g. the result of fitting "diskbb+power law" and "diskbb" models to one data set are allowed to be compared using F-test. If the F-test probability is low, then the model with the extra component is the more suitable model.

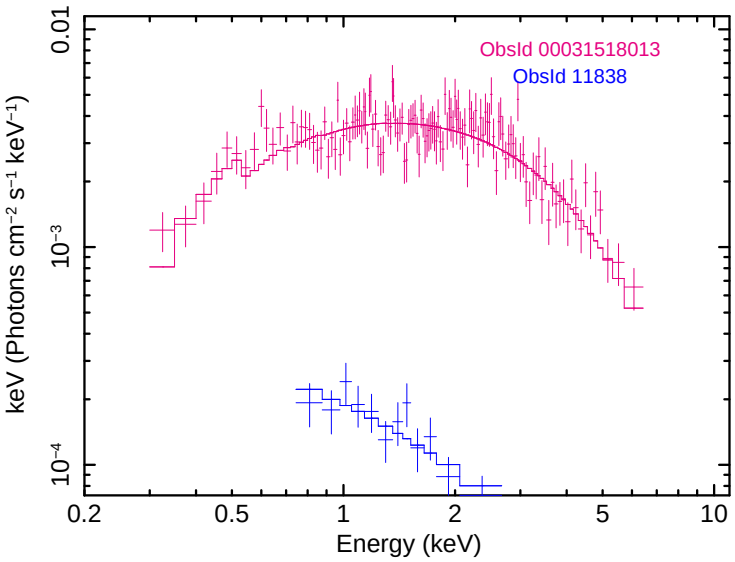


Figure 4.4: *The spectrum of r2-75 from the first Swift observation (ObsId 0031518013), compared to the Chandra observation obtained 150 days later (ObsId 11838). The best fit spectrum to the former is a disk black body model, whereas for the later, the preferred model is that of a power law.*

taneously fitting spectra from the 27 May 2010 Chandra (ObsID 11838) observation and the 6 June 2010 Swift observation (ObsID 00031255013). Results from this simultaneous fit had smaller uncertainties relative to those obtained from a fit to the Chandra spectrum alone. The best fit was an absorbed power law with N_H frozen at $6{\times}10^{20}$ cm^{-2} and $\Gamma = 2.5{\pm}0.2$, yielding χ^2/dof = 23/21; such a spectrum is consistent with a black hole transient entering the low/hard state as the outburst decays.

We fitted a power law model to our last Chandra observation (ObsId 11839).

To estimate the X-ray upper limit for r2-75 when it had returned to quiescence on 24-Aug-2010 (ObsID 11841), we used the CIAO task **aprat**[15], and set the conf parameter to 0.99. To convert this 3-σ upper limit to a flux, we assumed a power law spectrum with Γ=1.7 and $N_H = 6 \times 10^{20}$cm^{-2} to generate the limit reported in Table 4.3.

A summary of our Chandra and Swift spectroscopic results are given in Table 4.3. The change in the spectrum of r2-75, is also shown in Figure 4.4 by comparing our first Swift observation (ObsId 00031518013) and (ObsId 11838). To calculate the error bars for the unabsorbed luminosity, we assumed the percentage error is the same for the absorbed and unabsorbed flux.

4.4.6 X-ray Light curve

The outbursts of a typical dwarf nova (see page 11 for a short introduction) last for a few days and recur on timescales of weeks to months, whereas the outbursts of XRTs for one month or

[15] http://asc.harvard.edu/ciao/threads/upperlimit/

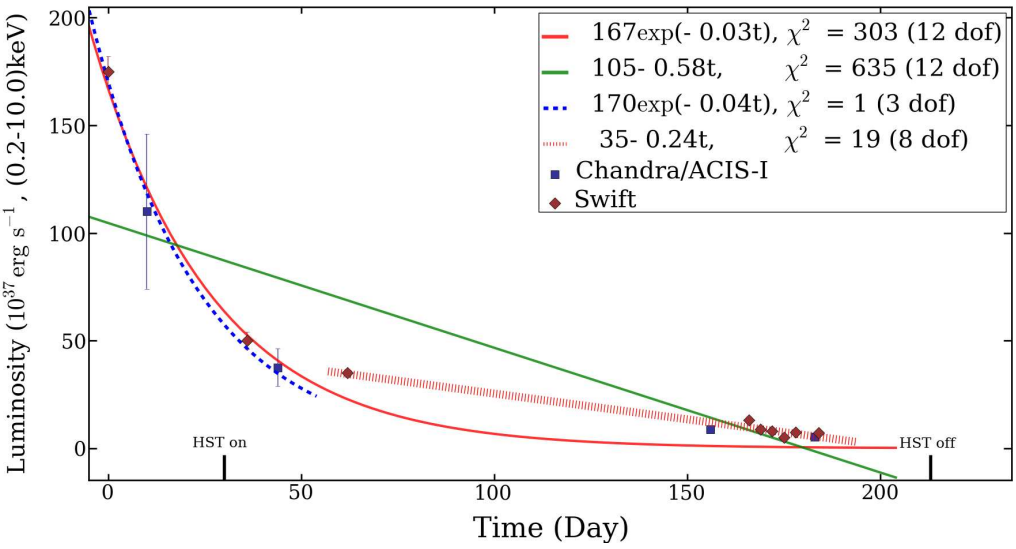


Figure 4.5: *The X-ray light curve of r2-75. Simple exponential or linear models do not fit the data (χ_ν are around 30 and 60 respectively). A better fit instead is a combined model consisting of an initially exponential decay followed by a longer, linear phase. These models are not only better fits, but are also consistent with the results of Shahbaz et al. (1998). The origin of the graph, in time, corresponds to first Swift observation.*

more, and the recurrence time-scale is years. King & Ritter (1998) (hereafter KR98) showed that this difference in time-scales may be explained by the X-ray irradiation occurring in XRTs; the X-ray radiation prevents the disk from returning to the cold state, meaning that more of the disk is emptied; hence the outbursts of XRTs are longer lasting and less frequent. KR98 showed that we may expect the XRT light curve to decay exponentially so long as the whole disk is irradiated; however, when the X-ray flux decreases sufficiently to allow the outer disk to cool (after several decay times), KR98 expect a linear decay. In fact, KR98 expect linear decay throughout the entire outburst for systems where the disk is so big that it is never fully irradiated. Indeed Shahbaz et al. (1998) were able to estimate binary sizes for several XRTs by using the exponential or linear nature of their decay.

Fig. 4.5 shows our derived 0.2-10 keV X-ray light curve. Unfortunately, we do not have points between 80 to 160 days after the outburst, so we assumed it to be a single-peaked light curve. Next we divided our data points into two groups, one consisting of data points fitted with a disk black body model and the other of data points fitted with a disk black body+power law or a power law model only. The best fit curve to the first group appears to be initially exponential, whereas a linear decay best fits the second. Such behavior is consistent with the expectations of KR98.

The results of KR98 suggest that the the decay constant should increase with orbital period,

but saturate at about 40 days for periods > 24 hours. Since the decay time for r2-75 looks to be about 25 days, we expect the orbital period to be significantly shorter than a day.

4.4.7 Orbital period Determination

Comparing the HST images obtained during and after the outburst revealed a candidate optical counterpart within the Chandra X-ray error circle. The observed images and the subtracted image are shown before in Fig. 4.3.

By using PHOT[16], we measured the magnitude of the optical counterpart to be 23.91 ± 0.08 in the B band. Using Equation 4.1, we obtain M_V=-0.91 ± 0.16, where the error has been calculated by combining the B-V error (the rms from the values in Liu et al. (2001)) and PHOT error, in quadrature. The July 2010 HST "off" observation yields an upper limit of $B > 24.2$.

To use VPM94 relation, we combine our HST observations with the Swift observation (ObsID 00031518014) obtained only 6 days afterwards. These two measurements yield $L_x = 50 \times 10^{37} \mathrm{erg\,s^{-1}}$, and M_V=-0.91 ± 0.16, from which we estimate $P_{\rm orb} = 1.07^{+0.3}_{-0.2}$ days (excluding the errors in the relation). Note, however, that although some of the X-ray fluxes used in the VPM94 relation were measured in the 2-10 keV range, rather than the 0.5-10 keV range of our measurement, we have not attempted to correct for this.

Our Swift spectroscopy (see Table 4.3) suggests that r2-75 was in high soft (thermal) state during our contemporaneous HST/Chandra measurements, therefore, using Eq. 4.3 (which was derived for systems in this state, as distinct from the VPM94 relation), and correcting our 0.5-10 keV flux for r2-75 to the 2-10 keV range, we derive a shorter orbital period of 15^{+6}_{-4} hours. The error includes those in Eq. 4.3 and that due to the uncertainty in $M_{\rm v}$.

Russell et al. (2006) have also investigated the relation between observed OIR fluxes, X-ray/radio emission and spectral state for a large sample of X-ray binaries. In their Fig 5, they relate the X-ray/optical flux and binary (semi-major) axis for 15 systems in the hard state. Using the Russell et al. (2006) analysis, we estimate a shorter orbital period for r2-75 of 1.75 hours. We favor a period about 15 hours over the shorter estimate of 1.75 hours for two reasons. Firstly, whilst the former is based on the M_v versus $\log(\Sigma)$ relation for sources in the soft state, the latter is strictly applicable to sources in the hard state only. As we have seen, r2-75 was in the soft state during our contiguous HST/Chandra measurements. Secondly, the structure of the secondary is

[16] http://stsdas.stsci.edu/cgi-bin/gethelp.cgi?phot

highly constrained under the assumption of Roche-lobe filling geometry, such that the average density is solely determined by the orbital period (ie, Eq. 4.8 of Frank et al. (1992)). The actual densities of known secondaries in Galactic black hole X-ray novae run from about 6.7 g/cm^3 to <1 g/cm^3 for the longer period systems (see Table 5.3 of Charles & Coe (2006)). Given the estimated primary mass of 14 $M_\odot$ (Kaur et al. 2012) a 1.75 hour period for r2-75 implies a density of 28 g/cm^3 for even the smallest secondary seen in the Galaxy (XTE J1118+480, at $M_2 = 0.25\ M_\odot$). Similarly, a period of 4 hours would imply a density of 7 g/cm^3, which while possibly reasonable implies a mass ratio of 56, which is out of line with what is seen in the Galaxy. For this reason too we favor our longer period over the 1.75 hr estimate.

Kaur et al. (2012) and Middleton et al. (2012) considered r2-75 as the first ultra-luminous X-ray source (ULX) detected in M31. Middleton et al. (2012) fitted the BHSPEC model to five subsequent XMM- Newton observations of r2-75. Assuming a black hole mass of 10 $M_\odot$, their fits yielded a best-fitting black hole spin a $\sim$ 0.4 during outburst whilst the luminosity declined from L/LEdd= 0.75 to 0.25. Middleton et al. (2012) also showed that systematic residuals to this fit remained in the spectra, which motivated them to try a "slim disk" model, combined with a low temperature Comptonized component (which could be related to a disk wind). Statistically, such a model appeared to be a better fit to the data than the BHSPEC model.

4.5 Period Distribution of SXTs in M31

Here I discuss an extension of the techniques described above to a sample of 12 M31 SXTs. The goal of this work (presented by Barnard et al. (2012)) is to constrain the orbital period distribution of LMXBs in the bulge of M31, and compare it to that of LMXBs in our Galaxy. For example, Voss & Gilfanov (2007) proposed that the bulge of M31 is sufficiently large and dense to allow the formation of a significant number of dynamically formed binaries. However, as the stellar velocities in the M31 bulge are $\sim$ 5-10 times higher than in globular clusters in our Galaxy, only short period binaries will survive. They concluded:" majority of the sources in M31 are short-period binaries, and in contrast to GCs many of them have BH accretors."

To see if the orbital period distribution is different between Galactic LMXBs and those in the bulge of M31, we list in Table 4.4 a summary of the properties of 12 M31 XRTs, along with the orbital period constraints (the location of these XRTs is also displayed in Fig 4.6) . Only four XRTs (T1, T2, T5 and T9) had more than 200 photons in the ACIS observations at the time of

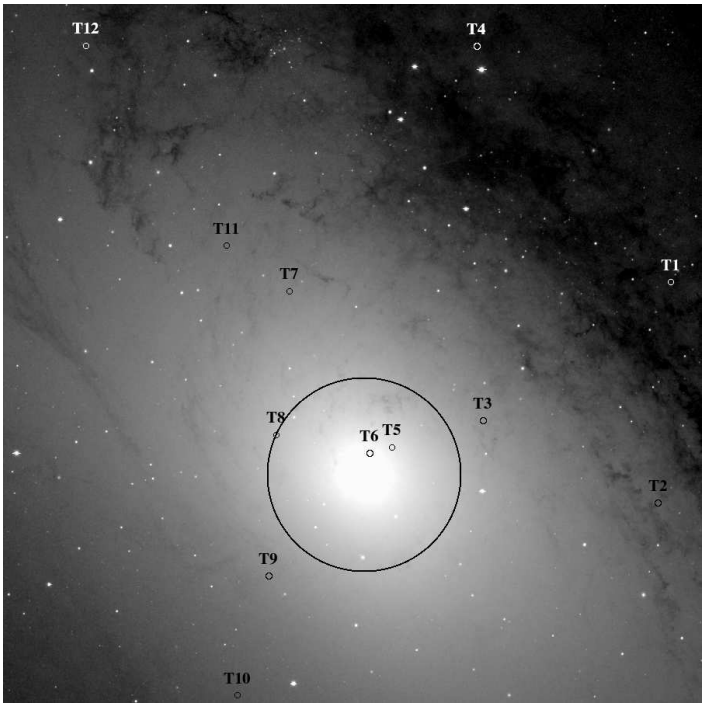


Figure 4.6: *Position of SXTs listed in table 4.4. Circle shows the area with radius* $100''$ *of the nucleus (Barnard et al. 2012).*

the optical exposures with HST. A diskbb model has been fitted to their spectra. The best fit results are also given in Table 4.4 (the third column). Note that, although I independently worked on the X-ray and optical data of sources T7, T8 and T11, most of the results that follow are from Barnard et al. (2012).

As discussed by Barnard et al. (2012), the results shown in Fig 4.7 suggest that indeed XRTs in the bulge of M31 may have systematically shorter periods than those in our Galaxy. Assuming that all 12 of the M31 XRTs host a black hole, then Barnard et al. (2012) find that the probability that the M31 XRT orbital period distribution is similar to that of black holes binaries in our Galaxy is < 0.08. This result is consistent with the prediction of Voss & Gilfanov (2007), although the observation of additional M31 XRTs is needed to increase the sample size and confirm this result.

In this Chapter, we have seen the importance of studying X-ray binaries in M31: the accurately known distance, relatively low line of sight extinction, and the ability to image the bulge in a single pointing all make M31 well suited for finding new X-ray transients, especially using Chandra.

We next discussed the steps involved in performing accurate astrometry for the Chandra images, using the positions of optically identified X-ray bright globular clusters.

No	R.A. [a]	Decl. [b]	fit parameters	$L_{\rm X}$ [c]	$L_{\rm Est}$ [d]	B [e]	$M_{\rm V}$	$P_{\rm VPM94}$ [g]	$P_{\rm M12}$ [h]
T1	00:42:16.106 ±0.015	+41:19:26.36 ±0.27	T_{in}= 1.5±0.3	8.9±2.3	0.3	>28.7	2.45	<10.6	<11.6
T2	00:42:17.330 ±0.012	+41:15:37.48 ±0.11	T_{in}= 0.54±0.04	12.8±1.2	2.89	24.7±0.3	−0.2	120±5	16^{+7}_{-5}
T3	00:42:33.426 ±0.012	+41:17:03.56 ±0.14	-	3.7±0.3	1.59	>27.2	2.3	<3.6	<4.5
T4	00:42:33.883 ±0.016	+41:23:31.49 ±0.19	-	2±0.2	0.88	>28.9	4	<0.4	<0.97
T5	00:42:41.805 ±0.010	+41:16:35.94 ±0.10	T_{in}= 1.1±0.2	5.8±0.8	2.52	>26.6	1.7	<6.0	<5.6
T6	00:42:43.834 ±0.011	+41:16:30.60 ±0.11	-	0.94±0.12	0.53	>26.3	1.4	<35	<31
T7	00:42:51.199 ±0.012	+41:19:17.81 ±0.13	-	0.51±0.1	0.35	>25	2.9	<380	<175
T8	00:42:52.433 ±0.010	+41:16:48.75 ±0.10	-	0.35±0.08	0.29	>23.9	−1	<2400	<1000
T9	00:42:53.181 ±0.010	+41:14:22.83 ±0.10	T_{in}= 0.8	38±9	18.62	23.91±0.08	−0.99	61±11	18^{+5}_{-6}
T10	00:42:56.049 ±0.012	+41:12:18.64 ±0.13	-	3±0.2	1.77	24.52±0.02	−0.38	163±8	9^{+5}_{-3}
T11	00:42:56.991 ±0.017	+41:20:05.35 ±0.31	-	0.39±0.10	0.2	24.87±0.09	−0.03	490±90	140^{+50}_{-40}
T12	00:43:09.963 ±0.030	+41:23:32.56 ±0.43	-	1.65±0.12	0.53	> 27.9	3	<2.8	<4.8

[a] Right ascension (R.A.) and 1σ uncertainty.

[b] Declination (Decl.) and 1σ uncertainty.

[c] The X-ray luminosity with the 0.3-10 keV during the nearest Chandra observation, normalized to 10^{37}erg s^{-1}.

[d] The estimated X-ray luminosity in 2-10 keV during the HST observation, normalized to 10^{37}erg s^{-1}.

[e] B magnitude (or 4σ upper limit) from HST-on observation.

[f] Absolute V-magnitude derived from Eq. 4.1.

[g] Orbital period estimated from Eq. 4.2.

[h] Orbital period estimated from Eq. 4.3.

Table 4.4: *Summary of the X-ray and the optical studies of SXTs in M31*

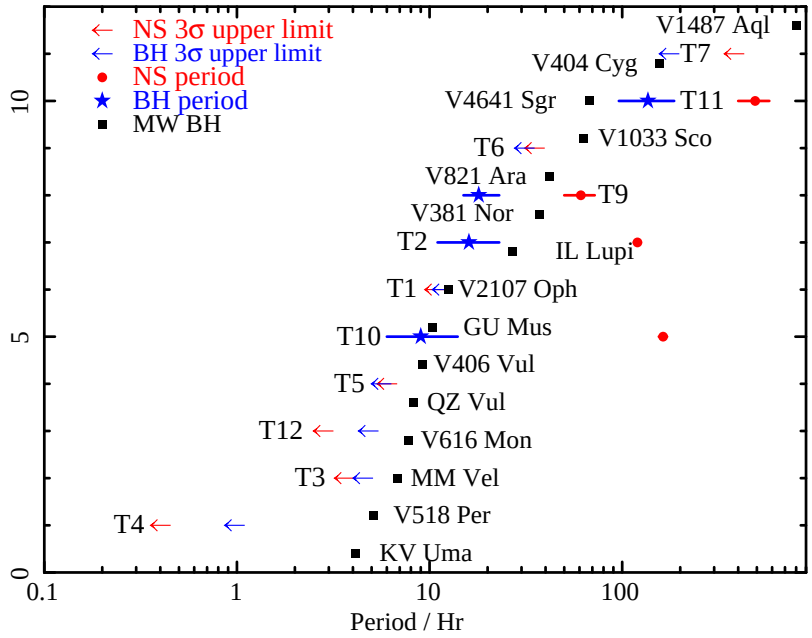


Figure 4.7: *Period distribution of 12 SXTs in M31, assuming the VPM94 and M12 for NS and BH XRBs, respectively. NS systems are shown by circles, BH systems with stars. The 3σ upper limits are indicated by arrows (Barnard et al. 2012).*

In order to find optical counterparts to bright XRTs, HST images are typically obtained in both the bright and quiescent state which are then subtracted: we outlined the astrometry and photometry required achieve this, and measure Mv. We then discussed the importance of the correlation found by van Paradijs & McClintock (1994) for M31 XRTs, and the use of Mv and the X-ray luminosity to constrain the orbital period (P).

We then implemented these techniques in the specific case of r2-75, a newly discovered, extremely bright, M31 XRT. We combined a series of Chandra and Swift observations of this source, allowing us monitor its luminosity and spectral evolution throughout the evolution of this particularly bright outburst. In addition, we identified a clear optical counterpart, which, when combined with the X-ray luminosity allowed us constrain P to 15^{+6}_{-4} hrs. To do this we used an updated version of the van Paradijs & McClintock (1994). Such a period, combined with the relatively high mass of the primary, suggests a mean density for the secondary star consist with those observed for other Galactic XRTs.

We concluded the Chapter with a discussion of the results presented by Barnard et al. (2012), in which measurements of a larger sample of M31 XRTs are used for the first time in an attempt to constrain the overall orbital period distribution of XRBs in M31. The results provide some support for the suggestion by Voss & Gilfanov (2007) that the period distribution of LMXBs in the bulge of M31 should be affected by dynamical interactions, and should be skewed to shorter

values (in comparison to the Galactic sample). However, the results of Barnard et al. (2012) would clearly benefit from a larger sample, particularly of optically identified M31 XRTs.

5

The Light Curves of X-Ray Transients in M31

When the effective temperature of an accretion disc in a LMXB is high enough to partially ionize the hydrogen in the disc, a thermal-viscous instability is triggered. The disc Instability Model (DIM) interprets the sudden increase in the luminosity (outburst) of the accretion disc as the result of this instability (Lasota 2001).

The DIM model is able to reproduce many observational properties of XRBs, provided that the effect of disc irradiation is taken into account (van Paradijs 1996a). In the irradiated disc model, the radius of irradiated disc (hot zone) is determined by the strength of the central X-ray emission. The outer layers of the accretion disc are heated by the central X-ray source: therefore, the surface temperature of the disc, $T_{\rm surf}$, is defined as

$$T_{\rm surf}^4 = T_{\rm eff}^4 + T_{\rm irr}^4, \tag{5.1}$$

where $T_{\rm eff}$ is the effective temperature in the absence of irradiation (Dubus et al. 1999). From the standard α-disc model (section 2.1), one can calculate $T_{\rm eff}$ as (see Eq. 2.17)

$$T_{\rm eff}^4(r) = \frac{3GM\dot{M}}{8\pi\sigma r^3}\Big[1-(\frac{R_{\rm in}}{r})^{1/2}\Big]$$

and $T_{\rm irr}$ is the irradiation temperature which is

$$T_{\rm irr}(R)^4 = \frac{\eta\dot{M}_c\, c^2(1-\beta)}{4\pi\sigma R^2}\Big(\frac{H}{R}\Big)^n\Big[\frac{d\ln H}{d\ln R}-1\Big], \tag{5.2}$$

where η is the efficiency of rest-mass energy conversion into X-ray heating, and $\dot{M}_c$ is the central accretion rate. H is the scale height at radius R and β is the albedo of the disc faces. The index n is 1 for NS and 2 for BH XRBs (van Paradijs 1996b). The ratio of H/R is roughly constant and the factor in the square brackets is between 1/8 and 2/7 (King & Ritter 1998; hereafter KR98), so one can write

$$T_{\rm irr}(R) \propto R^{-1/2}.$$

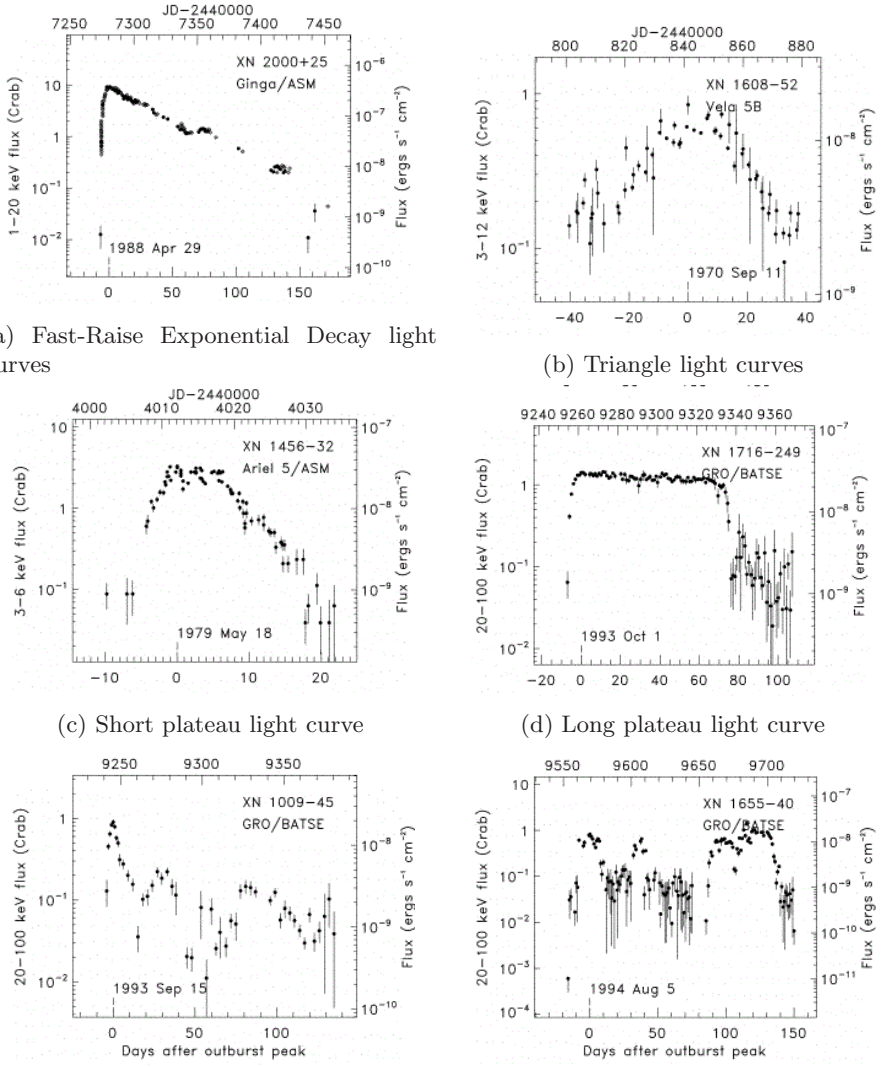
From Eq.2.17, the effective temperature from α-disc model is

$$T_{\rm eff}(R) \propto R^{-3/4}.$$

Therefore, the irradiation temperature becomes dominant for large R.

Using the irradiated disc model, van Paradijs (1996a) discriminated between persistent and transient XRBs depending on a critical mass transfer rate. If $\dot{M}_c > \dot{M}_{\rm crit}$, the central accretion rate is high enough so that the irradiation prevents the disc from cooling down and the XRB shows persistent X-ray emission from the accretion disc (so remains a persistently bright XRB). In the case of a lower accretion rate, the disc cools down and the X-ray emission switches off (i.e. the system reaches quiescence). Collecting a sample of the available LMXB data at the time, van Paradijs (1996a) showed that his model was consistent with the observations. Fifteen years later, Coriat et al. (2012) by gathering a sample consisting of 52 persistent and transient NH and BH LMXBs, found the data in very good agreement with the theoretical model.

Using the light curves of Galactic XRTs, Shahbaz et al. (1998) showed that they decay either exponentially or linearly depending on the strength of the central X-ray source, as KR98 has predicated theoretically.



(a) Fast-Raise Exponential Decay light curves

(b) Triangle light curves

(c) Short plateau light curve

(d) Long plateau light curve

(e) Variable light curve

(f) Multipeak light curve

Figure 5.1: *Different morphological light curves types (Chen et al. 1997).*

Chen et al. (1997) classified the morphology of the light curve of XRTs into 5 groups; a sample of each group is shown in Fig. 5.1 (the plateau class has been divided into short and long). The most frequent shape is known as Fast-Raise Exponential Decay (FRED) light curve. The other four groups are triangular, plateau (short and long), variable decay and multipeak. The KR98 model can not explain some complicated light curves morphologies e.g. variable decay and multipeak.

Despite the success of the irradiated disc model in explaining the global behavior of XRBs, some complex features of outburst light curves remain unexplained (see Truss et al. (2002) as an example). This model still depends on unknown physics of the efficiency of irradiation effect.

5.1 The Outburst of an Irradiated Disc

Assuming the accreting disc has quasi-steady surface density profile, the surface mass density in the hot stage can be written as

$$\Sigma(R) \simeq \frac{\dot{M}_c}{3\pi\nu}, \tag{5.3}$$

where $\dot{M}_c$ and ν are the central accretion rate and the average of the kinematic viscosity in the disc, respectively.

The total mass of the hot zone, M_h, can be calculated by integrating the surface density over the area of the hot zone of the accretion disc:

$$\begin{aligned} M_h &= \int \Sigma\, r\, dr\, d\phi = 2\pi \int_0^{R_h} \Sigma\, r\, dr \\ &\simeq \frac{\dot{M}_c}{3\nu} R_h^2 \end{aligned} \tag{5.4}$$

where R_h is the radius of the hot zone. The only changes in the mass of the hot zone can happen through the central accretion, therefore

$$\dot{M}_c = -\dot{M}_h.$$

So, Eq.5.4 can be rewritten as

$$M_h = \frac{R_h^2}{3\nu}(-\dot{M}_h) \tag{5.5}$$

Solving this differential equation gives the mass of the hot zone:

$$\begin{aligned} \frac{-1}{M_h}\frac{dM_h}{dt} &= \frac{3\nu}{R_h^2} \Longrightarrow \ln M_h \Big|_{M_0}^{M_h} = \frac{-3\nu t}{R_h^2} \\ M_h &= M_0 \exp(\frac{-3\nu t}{R_h^2}), \end{aligned} \tag{5.6}$$

where M_0 is the initial mass of the hot zone. The density of disc before the outburst must is $\Sigma_{\rm min} \simeq 3 \times 10^{-8}\,{\rm R\,g\,cm} < \Sigma({\rm R}) < \Sigma_{\rm max} \simeq 1 \times 10^{8}\,{\rm R\,g\,cm}$ (Cannizzo 1993). So, one can re-write $\Sigma_{\rm max}$ from the right hand side of the above equation as:

$$\Sigma_{\rm max}(R) \simeq \frac{\rho}{2\pi} R,$$

where $\rho \sim 3 \times 10^{-8} \mathrm{g\,cm^{-3}}$. So, to estimate the value of M_0,

$$M_0 = 2\pi \int_0^{R_h} \Sigma_{\max} R\, dR \Longrightarrow M_0 \simeq \frac{\rho R_h^3}{3} \tag{5.7}$$

Inserting the obtained value for the initial mass from Eq.5.7 in Eq.5.6 gives the mass of the hot zone as

$$M_h = \frac{\rho R_h^3}{3} \exp(\frac{-3\nu t}{R_h^2}), \tag{5.8}$$

and the rate of the accreting mass is

$$\dot{M}_c = -\dot{M}_h = R_h \nu \rho \exp(\frac{-3\nu t}{R_h^2}). \tag{5.9}$$

From Eq.5.9 one can see that the first part of the X-ray light curve should exhibit an **exponential decay**. It should be noticed that the result is only an approximation since the value of ν has been assumed constant, on average of its characteristic value in the outer disc.

When the irradiation is not strong enough to irradiate entire disc, the disc becomes partially irradiated only. The temperature of the irradiated zone, R_h, is defined as

$$T_{\mathrm{irr}}(R_h) = T_H.$$

From Eq. 11 in KR98 (see the references there for more information), one can write

$$R_h^2 = B_n \dot{M}_c \tag{5.10}$$

where the subscripts 1 ($B_1 \simeq 4 \times 10^5$ (cgs)) and 2 ($B_2 \simeq 5 \times 10^4$ (cgs)) are referring to NS and BH XRBs, respectively. The central accretion rate from Eq. 5.4, using Eq.5.10, is

$$\dot{M}_c = (\frac{3\nu}{B_n})^{1/2} M_h^{1/2}. \tag{5.11}$$

At this stage, the mass of the hot zone decreases because of two factors: the increasing the central accretion rate, and the shrinking of R_h as $\dot{M}$ drops, so one can formulate it as

$$\dot{M}_h = -\dot{M}_c + 2\pi \Sigma R_h \dot{R}_h \tag{5.12}$$

The second term in the right hand side of Eq. 5.12 can be rewritten by inserting the values of Σ from Eq.5.3. Also R_h and $\dot{R_h}$ must be substituted from Eq.5.10, so

$$\begin{aligned} 2\pi\Sigma R_h\dot{R}_h &= 2\pi\Big(\frac{\dot{M}_c}{3\pi\nu}\Big)\Big(B_n\dot{M}_c\Big)^{1/2}\Big[\frac{1}{2}B_n^{1/2}\dot{M}_c^{1/2}\ddot{M}_c\Big] \\ &= \frac{\dot{M}_c}{3\nu}B_n\ddot{M}_c \end{aligned} \tag{5.13}$$

therefore, Eq.5.12 can be rewritten as

$$\dot{M}_h = -\dot{M}_c + \frac{\dot{M}_c}{3\nu}B_n\ddot{M}_c \tag{5.14}$$

If one finds the value of $\dot{M}_h$ from Eq. 5.11 as

$$\dot{M}_h = \frac{2\ddot{M}_c}{(3\nu/B_n)^{1/2}M_h^{-1/2}},$$

and replaces it in Eq.5.14, one gets

$$\begin{aligned} \ddot{M}_c\Big[2(\frac{3\nu}{B_n})^{1/2}M_h^{1/2} - \frac{B_n}{3\nu}\dot{M}_c\Big] &= -\dot{M}_c \\ \ddot{M}_c\Big[2(\frac{3\nu}{B_n})^{-1} - \frac{B_n}{3\nu}\Big] &= -1 \Longrightarrow \frac{B_n}{3\nu}\ddot{M}_c = -1 \end{aligned} \tag{5.15}$$

By replacing Eq. 5.15 in Eq. 5.14, one can simply write

$$\dot{M}_h = -2\dot{M}_c.$$

Inserting the value of $\dot{M}_c$ from Eq. 5.11:

$$\dot{M}_h + 2(\frac{3\nu}{B_n})^{1/2}M_h^{1/2} = 0, \tag{5.16}$$

and solving the differential equation gives,

$$M_h = \Big[M_h^{1/2}(T) - (\frac{3\nu}{B_n})^{1/2}(t-T)\Big] \tag{5.17}$$

where $M_h(T)$ is the mass of hot disc when the phase starts at time T.Eq. 5.17 predicts a **linear decay** of the X-ray light curve, in the case of an accretion disc is not strongly irradiated.

5.2 Light Curve of Bright Transients in M31

As we have seen the light curve of brighter transients should show a transition from an exponential decay to a linear one as the outburst continues, and the disc becomes progressively less irradiated.

To examine this prediction, I decided to acquire archival X-ray data from very bright XRTs in M31 whose peak luminosities satisfied

$$L_{\rm peak} \geq 10^{38} {\rm erg\,s^{-1}}.$$

In order to have the maximum possible light curves, publicly available X-ray data of the bright M31 XRTs observed with Chandra (ACIS), XMM-Newton (PN) and Swift (XRT) were retrieved from **HEASARC** web site[1]. To have a sample only consisting of XRTs, other types of transients were excluded from the study as described below.

As discussed on page 64, poor angular resolution of XMM and SWIFT, compared to the Chandra's, may cause source confusion. Therefore, the Chandra image of each source has been checked for presence of a nearby source. The sources in this study do not suffer from source confusion.

Hard X-ray transients are expected to be observed in high mass X-ray binaries, where accretion is driven by stellar winds. The spectrum of these transients are significantly harder than soft X-ray transients. Thus, studying their spectrum reveals their nature. This group of transient sources, even the very bright ones, are not included in this study, e.g. a very bright hard transient CXO J004242.0+411608 (Garcia et al. 2000; Trudolyubov et al. 2001) with luminosity $(1.4\pm0.08)\times10^{38}{\rm erg\,s^{-1}}$ is a hard X-ray transient and therefore excluded from the study list.

A large subgroup of transient sources are the Super Soft X-ray Sources (SSSs). It is believed that SSSs occur when matter accretes from the companion onto white dwarf, after filling the Roche lobe. SSSs exhibit bright point sources in the X-ray sky with the luminosity $10^{37} - 10^{39}{\rm erg\,s^{-1}}$, even though the maximum energy of their emission is no more 1.5 keV. Therefore displaying the spectrum of these sources in XSPEC proves their super soft characteristic. For instance XMMU J004319.4+411759 (designated name r3-126 Williams et al. (2006b)) exhibits a luminosity $\sim 1.3\times 10^{38}{\rm erg\,s^{-1}}$ in 0.3-1.5 keV (Trudolyubov et al. 2001). (For more information see Di Stefano et al. (2004)).

[1] http://heasarc.gsfc.nasa.gov/docs/archive.html

Table 5.1: *List of the bright sources*

Coordinate	Name	Outburst (days)[a]
00:42:16.1 +41:19:26.7	XMMU J004215.8+411924	32 - 71 [b]
		22 - 110 [c]
00:42:17.3 +41:15:37.2	SWIFT J004217.4+411532	137 - 180
00:42:53.2 +41:14:22.6	CXOM31 J004253.1+411422	184 - 259
00:43:05.6 +41:17:03.3	CXOM31 J004305.7+411703	132 - 222
00:43:20.56 +41:15:28.8	SWIFT J004320.5+411528	61 - 132

[a] The minimum duration of any outburst is determined by the interval between the first and the last X-ray detections. The upper limit is, then, given by the time interval between the previous and next observations from the first and last detections.

[b] First outburst in 2006.

[c] Re-outburst in 2010.

To estimate an accurate X-ray luminosity, spectral fits are required. However due to the lack of spectral information in the Chandra HRC data, the count rate of the source must be converted to flux by assuming a model obtained from some other observation. Because of this limitation all M31 HRC-I observations have been excluded from this study.

The final list of the bright sources is given in table 5.1.

Spectral analysis of the sources listed in table 5.1 are presented individually here. The best fit parameters are summarized in table 5.2. For most sources, the value of hydrogen column density is determined from the best fit result which provides a value consistent with the hydrogen column density towards M31. For those observations which did not have enough count number to fit a model, N_H was frozen to the values according to the previous observations.

- **XMMU J004215.8+411924**

  Checking for source confusion, the Chandra image shows that the closest X-ray source is located at radius of $60''$ from this source. Therefore none of XMM and Swift images suffer from source confusion.

  For the spectrum of the first detection of XMMU J004215.8+411924 (Haberl et al. 2006; Galache et al. 2006), both a power law model and a disc black body model gave an acceptable fit but the obtained value for $T_{in}$is higher than the expected temperature for an accretion

disc, so a power law model fit was preferred.

Due to the low count number in the last observation (ObsId 00030802001) the parameters were frozen to the values of previous observation fit obtained using the Cash statistic.

The second outburst of the source was detected 4 years later (Noorraee et al. 2010; Barnard et al. 2011) in an ACIS observation (ObsId 11838). Fitting a power law model gives a better fit when compared to a disc black body model. The following XRT observation data did not have enough counts to fit the spectrum, so the parameters were frozen to the best fit parameters for the ACIS data.

Barnard et al. (2011) noted that the position of the source (during the second outburst) is just $1.6''$ from the position of source number 17 of Crampton et al. (1984) observed with the *Einstein* HRI and hence concluded that this source had a detected outburst over 30 years ago. Optical studies during the 2006 outburst (Voss et al. 2008) and 2010 outburst (Barnard et al. 2011) could not rule out a Be companion star, therefore the host binary system of this X-ray transient is most likely to be a LMXB. So, this was categorized as an XRT in the present study.

The X-ray light curves of the first outburst and re-outburst are shown in figures (5.2a) and (5.2b), respectively.

- **SWIFT J004217.4+411532**

  The first Chandra image shows the nearest X-ray source is located at radius of $65''$ from this source. Therefore SWIFT and XMM data can be used.

  Detected firstly by a Swift observation on September 2006 (Haberl et al. 2006; Voss et al. 2008), SWIFT J004217.4+411532 appeared in seven X-ray observations during its $\sim$ 140 days outburst. A disc black body model, in all of the seven observations, gives the best fit result. The photon numbers in ObsId 8183 are not enough to carry out a fit. Thus, the data are binned to 1 count per bin and fit parameters frozen to the values of the XMM observation taken two days earlier. The light curve is plotted in figure (5.2c).

- **CXOM31 J004253.1+411422**

  The Chandra, Swift and HST studies of this source was presented in the previous Chapter (section 4.4). Here the XMM observations have been added to the X-ray study; The first four

XMM observations (ObsIds 0600660201,0600660301, 0600660401 and 0600660501) showed pileup, but they could be fitted by a disk black body model using spectrum extracted from an annulus centered on the source. The source spectrum of the Swift/XRT observation (ObsId 00031518014) is not piled up and a disk black body fits the data reasonably. Due to pile up, the next XMM spectrum (ObsId 0600660601) was extracted using an annulus. Fitting a disk black body and a power law model to these data gives a reliable fit. The result of this fit and a disk black body only is compared with *Ftest* [2]. The small value of F-test shows the combination of a power law model and a disk black body model is gives an acceptable fit. The light curve is shown in figure (5.2d).

- **CXOM31 J004305.7+411703**

  Checking the first Chandra image for source confusion, shows the closest X-ray source is located at radius of $65''$ from this source. Therefore this source cannot be confused in Swift and XMM images.

  Discovered first in a Chandra/ACIS-I observation in August 2001 (Kong et al. 2001), the source has been observed in six X-ray observations throughout the outburst which lasted for approximately 140 days.

  In the first four Chandra/ACIS observations (ObsIds 1577, 1575, 1585 and 2895) the source spectrum is piled up. A pileup model and a disc black body were fitted to all the spectra except ObsId 1575. The severity of pileup in the spectrum of the source in ObsId 1575, which was taken 35 days after the first discovery, could not be fixed by fitting a pileup model and the fit result was unacceptable, so this observation has been removed from the study. The values obtained from fitting a pileup and a disc black body model to the other three ACIS observations were acceptable.

  Fitting a disc black body and a power law model to the next observation (ObsId 0112570101) gives a very good fit result, whereas a disc black body could not fit the data.

  To the last observation (ObsId 2897), a power law model fits the data perfectly. The light curve of the source is shown in figure (5.2e).

- **SWIFT J004320.5+411528**

[2] https://heasarc.gsfc.nasa.gov/xanadu/xspec/manual/XSftest.html

Checking for source confusion, the Chandra image shows the closest X-ray source is located at radius of $120^{''}$ for this source. Therefore this source cannot be confused in Swift and XMM images.

Seven days after its first detection as a new transient in an XRT observation (Pietsch et al. 2008), SWIFT J004320.5+411528 showed an increase in the luminosity from 1.82 $\times 10^{38}$erg s^{-1} to 2.62 $\times 10^{38}$erg s^{-1}. Fitting a disc black body model to the spectrum for both observations, gives an acceptable result. Therefore, the first detection was obtained before the transient reached its maximum luminosity.

The photons in three XRT observations (ObsIds 00031255003, 00031255008 and 00031255010) were binned to 10 counts per bin. Due to the short exposure time (2 ks) in ObsId 00031255009, the data were binned to 1 count per bin and the Cash statistic used.

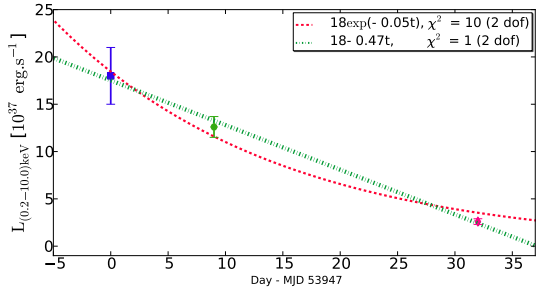
Fitting a disc black body model to all of the spectra, throughout the outburst, gives the best fit result. The light curve of SWIFT J004320.5+411528 is shown in figure (5.2f).

5.3 Discussion

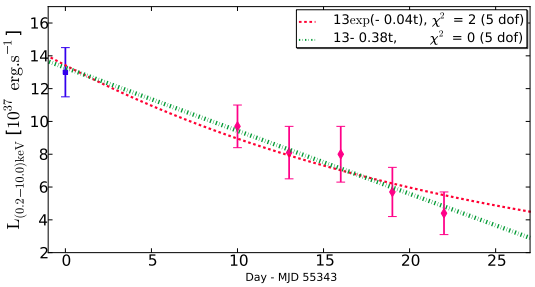
Outburst Lightcurves

The X-ray spectra of neutron star binary systems are composed of a black body component, consistent with the neutron star surface, and a softer component, most probably emitted from the multicolor accretion disc. Due to the absence of a physical surface, the X-ray spectrum of a black hole binary consists of a soft component and a hard power law tail. The characteristic temperature of the soft component in a neutron star binary system is $\sim$ 1.5 keV (when $L_x \sim 10^{38}$erg s^{-1}), while an upper temperature limit ($\leq$ 1.2 keV) has been observed for the black hole binary systems (Tanaka & Shibazaki 1996). The values of T_{in} in table 1 suggest that the XRTs in this study are black hole binary systems, even though it should noted that the X-ray spectrum of a binary system alone cannot provide definitive evidence for the presence or absence of a black hole in the system.

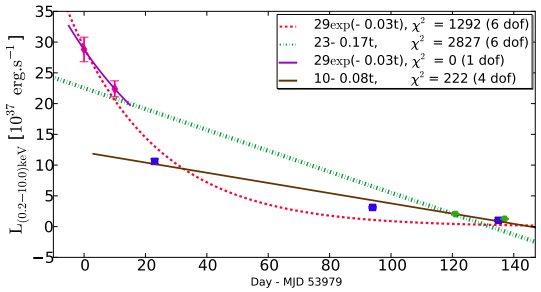
As mentioned before, Chen et al. (1997) showed that FRED is the most frequent morphology. The result of our study is consistent with their result; five out of the six light curves show FRED morphology. CXOM31 J004305.7+41170 is an exception, that Chen et al. (1997) classified this morphology as plateau shaped light curve (see figure5.1c&d). Due to the plateau shaped light



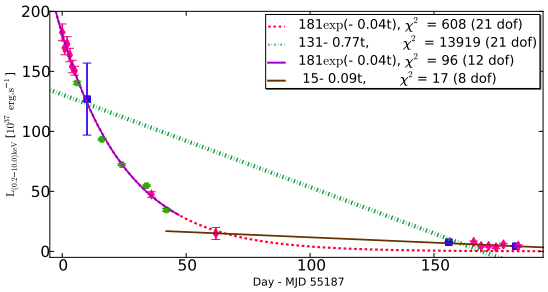
(a) XMMU J004215.8+411924, outburst I (2006)



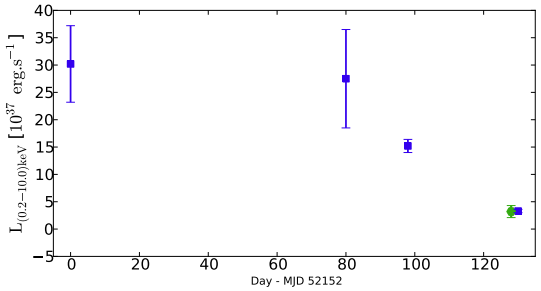
(b) XMMU J004215.8+411924, outburst II (2010)



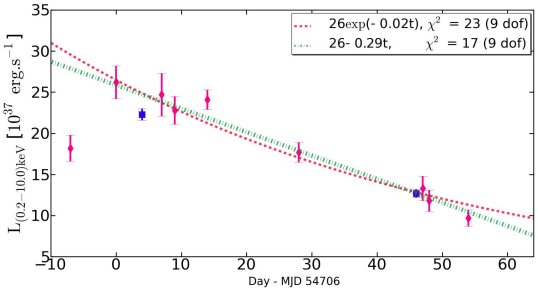
(c) SWIFT J004217.4+411532



(d) CXOM31 J004253.1+411422



(e) CXOM31 J004305.7+411703



(f) SWIFT J004320.5+411528

Figure 5.2: *X-ray unabsorbed light curve of the sources. Details of best fit parameters are given in table symbols: blue square is Chandra/ACIS, green hexagonal is XMM/EPIC-PN and red diamond is Swift/XRT.*

curve, the light curve of CXOM31 J004305.7+411703 (Fig. 5.2e) can neither be fitted to an exponential nor linear function.

A linear function rather than an exponential provides a better fit to three light curves in this sample: both outbursts of XMMU J004215.8+411924 (figures 5.2a and 5.2b) and SWIFT J004320.5+411528 (fig 5.2f). To fit a function to the light curve of SWIFT J004320.5+411528, the first data point which is not the maximum luminosity is assumed as pre-maximum point and excluded from the fit.

The best fit for the two X-ray light curves in this sample, SWIFT J004217.4+411532 (Fig. 5.2c) and CXOM31 J004253.1+411422 (fig 5.2d), is an exponential fit followed by a linear function.

Comparison with Theory

In the KR98 model, the decay constant in the exponential decay represents the viscous time of the outer accretion disc. Comparing the decay constant time of the exponential fit to the light curves in Fig. 5.2 (20, 25, 33, 25 and 50 days) with the Galactic XRTs with exponential decays i.e. A0620-00 ($\tau \sim 24$ days), J 0422+32 ($\tau \sim 40$ days) and 2000+251 ($\tau \sim 30$ days) (Tanaka & Shibazaki 1996) shows consistency.

In the disc irradiation model, the amount of irradiation is an important parameter (see section 5.1). If the central X-ray source is strong enough to irradiate the disc entirely, then the size of the irradiated disc can be estimated from Kepler's law and Roche geometry. Therefore, one can derive scaling laws between the orbital period and the evolutionary state of the binary system. Binary systems with longer orbital periods are assumed to have longer outburst decay constants. However, KR98 predicted that the decay constant of the binary systems with orbital periods of longer than a day, saturate at $\sim$ 40 days. They also noted that for longer orbital period systems (therefore bigger accretion discs) one should expect a linear decline (e.g. GRO J1744-28, the binary system with the longest orbital period among Galactic XRTs (12 days) showed a light curve with an entire linear decline). Unfortunately, due to the large distance, optical follow up of XRTs in M31 is not possible. However, as shown in Chapter 4, using optical observations with the Hubble Space Telescope and the empirical relationship between X-ray luminosity and optical magnitude, Barnard et al. (2012) constrained the orbital period for twelve XRTs in M31 which include estimates for the orbital period of three binary systems in this paper (here the orbital period estimated by the M12 method in table 2 of Barnard et al. (2012) is used. The estimated orbital period for the XRTs

of M31 in this study (P= 11.6 hours for XMMU J004215.8+411924, P= 16^{+7}_{-5} hours for SWIFT J004217.4+411532 and P = 18^{+5}_{-6} hours for CXOM31 J004253.1+411422) are not longer than a day. Thus, it is not possible to compare these system with the above KR98 predictions or the Galactic XRTs.

The light curves of the six bright sources in this study, suggest that the X-ray luminosity may not be the only determining factor for the shape of decline function of the light curve. Even though all the sources in this study can be classified in the group of brighter sources in M31, just 2 out of 6 light curves show an exponential followed by a linear fit.

This study does not indicate any systematic correlation between the spectral evolution and the shape of light curve, e.g. despite having similar light curve shape, SWIFT J004217.4+411532 (Fig. 5.2c) does not show any spectral change throughout its outburst while CXOM31 J004253.1+411422 (figure 5.2d), clearly shows two different spectral changes. Also, the spectral model of the data points can not predict the shape of light curve, e.g. all data points of SWIFT J004217.4+411532 and SWIFT J004320.5+411528 are fitted with the disk black body model, the light curve of the first one is fitted by an exponential function followed by a linear while the light curve of the later shows a linear decline is the best fit.

We have seen that, depending on the X-ray irradiation of the accretion disk in XRTs, the resulting light curves are expected to be exponential or linear King & Ritter (1998): indeed, as the X-ray luminosity decreases during an outburst, some light curves are expected to transition between an exponential and linear phase.

To test this prediction, I attempt a systematic study of the light curves of bright transient sources in M31. Setting a lower limit for maximum X-ray luminosity of $10^{38}\mathrm{erg\,s^{-1}}$ and gathering the available data from three X-ray telescopes (Chandra, XMM-Newton and Swift), a sample of 6 light curve was produced.

In contrast to the predictions of King & Ritter (1998), I found that only two light curves in this sample show the exponential decay predicted by this model. This suggests that the X-ray luminosity may not be the only determining factor for the shape of the outburst light curve. Furthermore, our study did not indicate any systematic correlation between the spectral evolution and the shape of light curve.

XMMU J004215.8+411924						
Date (ObsId)	Inst.[a]	T[b]	$N_H(10^{21})$	fit parameters[c]	χ^2/dof	L[d] ($\times10^{37}$)
2006 - 07 - 02 (0405320501)	PN	-	3.4	Γ= 1.5	–	< 0.30
2006 - 07 - 31 (7139)	ACIS	0	5.3 ±1.5	Γ= 1.9 ±0.2	16.2/15	18.5 ±3.1
2006 - 08 - 09 (0405320601)	PN	9	3.4 ±0.07	Γ= 1.6 ±0.1	18.9/18	12.6 ±1.1
2006 - 09 - 01 (00030802001)	XRT	32	3.4	Γ= 1.6	21.6/27	2.63 ±0.6
2006 - 09 - 11 (00030804001)	XRT	-	3.4	Γ= 1.6	–	< 0.41
2010 - 03 - 05 (11279)	ACIS	-	4.1	Γ= 1.5	–	< 0.14
2010 - 05 - 27 (11838)	ACIS	0	4.1±2.2	Γ= 1.5 ±0.2	7.1/10	12.9 ±1.5
2010 - 06 - 06 (00031255012)	XRT	10	4.1	Γ= 1.5	36.2/50	9.7 ±1.3
2010 - 06 - 09 (00031255013)	XRT	13	4.1	Γ= 1.5	34.2/42	8.1 ±1.6
2010 - 06 - 12 (00031255014)	XRT	16	4.1	Γ= 1.5	45.9/37	8.0 ±1.7
2010 - 06 - 15 (00031255015)	XRT	19	4.1	Γ= 1.5	24.2/23	5.7 ±1.5
2010 - 06 - 18 (00031255016)	XRT	22	4.1	Γ= 1.5	19.1/19	4.4 ±1.3
2010 - 06 - 23 (11839)	ACIS	-	4.1	Γ= 1.5	–	< 0.10
SWIFT J004217.4+411532						
Date (ObsId)	Inst.[a]	T[b]	$N_H(10^{20})$	fit parameters[c]	χ^2/dof	L[d] ($\times10^{37}$)
2006 - 08 - 09 (0405320601)	PN	-	6		–	< 0.07
2006 - 09 - 01 (00030802001)	XRT	0	5.8±1.9	T_{in}= 0.63±0.04	29.7/71	28.8 ±2.0
2006 - 09 - 11 (00030804001)	XRT	10	6	T_{in}= 0.51±0.03	14.4/15	22.4 ±1.3
2006 - 09 - 24 (7140)	ACIS	23	6	T_{in}= 0.55±0.03	24.2/25	10.6 ±0.4
2006 - 12 - 04 (7064)	ACIS	94	6	T_{in}= 0.34±0.01	18.3/21	3.12 ±0.1
2006 - 12 - 31 (0405320701)	PN	121	6	T_{in}= 0.31±0.01	101.9/58	2.04 ±0.07
2007 - 01 - 14 (8183)	ACIS	135	6	T_{in}= 0.27	46.8/38	1.02 ±0.16
2007 - 01 - 16 (0405320801)	PN	137	6	T_{in}= 0.27±0.01	30.6/25	1.26 ±0.06
2007 - 02 - 05 (0405320901)	PN	-	6		–	< 0.03
CXOM31 J004253.1+411422						
Date (ObsId)	Inst.[a]	T[b]	$N_H(10^{20})$	fit parameters[c]	χ^2/dof	L[d] ($\times10^{37}$)
2009 - 12 - 08 (11276)	ACIS	-	5	Γ= 1.7	–	< 0.10
2009 - 12 - 22 (00031518013)	XRT	0	5.1 ±1.7	T_{in}= 1.17 ±0.06	65.8/61	182.5 ±7.0
2009 - 12 - 23 (00035336016)	XRT	1	5.6 ±1.4	T_{in}= 1.09 ±0.05	67.5/78	169.5 ±5.7
2009 - 12 - 24 (00035336017)	XRT	2	5	T_{in}= 1.23 ±0.05	63.4/64	172.7 ±6.2
2009 - 12 - 25 (00035336018)	XRT	3	5.1 ±1.4	T_{in}= 1.14 ±0.05	66.6/67	163.6 ±5.6
2009 - 12 - 26 (00035336019)	XRT	4	5	T_{in}= 1.06 ±0.04	67.2/62	154.0 ±5.2
2009 - 12 - 27 (00035336020)	XRT	5	5	T_{in}= 1.21 ±0.04	90.7/114	150.5 ±3.7
2009 - 12 - 28 (0600660201)	PN	6	5	T_{in}= 0.90 ±0.01	698.6/535	140.4 ±1.4
2010 - 01 - 01 (11277)	ACIS	10	5	α= 0.5	12.9/12	126.9 ±30
				T_{in}= 0.98 ±0.1		
2010 - 01 - 07 (0600660301)	PN	16	5	T_{in}= 0.85 ±0.01	628.6/476	93.3 ±0.9
2010 - 01 - 15 (0600660401)	PN	24	5	T_{in}= 0.79 ±0.01	555.5/402	72.3±0.8
2010 - 01 - 25 (0600660501)	PN	34	5	T_{in}= 0.73 ±0.01	318.82/307	54.7 ±0.7
2010 - 01 - 27 (00031518014)	XRT	36	4.4 ±1.8	T_{in}= 0.86 ±0.05	22.6/33	47.4±2.3
2010 - 02 - 02 (0600660601)	PN	42	5	T_{in}= 0.64 ±0.02	464.7/379	34.5 ±1.3
				Γ= 1.86 ±0.09		
2010 - 02 - 22 (00031518015)	XRT	62	5.0	T_{in}=0.48 ±0.08	36.2/36	14.9 ±5
				Γ= 1.49 ±0.5		
2010 - 05 - 27 (11838)	ACIS	156	5	Γ= 2.2 ±0.1	20.5/22	7.7 ±0.5
2010 - 06 - 06 (00031255012)	XRT	166	5	Γ= 2.5 ±0.2	55.0/68	7.7 ±1.0
2010 - 06 - 09 (00031255013)	XRT	169	5	Γ= 2.2 ±0.3	36.0/49	4.3 ±0.6
2010 - 06 - 12 (00031255014)	XRT	172	5	Γ= 2.2 ±0.3	21.6/42	4.4 ±0.7
2010 - 06 - 15 (00031255015)	XRT	175	5	Γ= 2.2	–	3.3 ±1.0
2010 - 06 - 18 (00031255016)	XRT	178	5	Γ= 2.2	–	5.7 ±1.0
2010 - 06 - 23 (11839)	ACIS	183	5	Γ= 2.2	13.8/9	4.3 ±0.4
2010 - 06 - 24 (00031255018)	XRT	184	5	Γ= 2.2	–	4.5 ±0.9
2010 - 08 - 24 (11841)	ACIS	-	5	Γ= 1.7	–	< 0.1

CXOM31 J004305.7+411703						
Date (ObsId)	Inst.[a]	T[b]	$N_H(10^{20})$	fit parameters	χ^2/dof	L[c] ($\times 10^{37}$)
2001 - 06 - 10 (1583)	ACIS	-	6.7	Γ= 1.7	–	< 0.23
2001 - 08 - 31 (1577)	ACIS	0	6.7	α= 0.5	36.0/38	30.2 $\pm$7.0
				T_{in}= 0.66$\pm$0.08		
2001 - 11 - 19 (1585)	ACIS	80	6.7$\pm$5.9	α= 0.5	39.7/37	27.5 $\pm$9.0
				T_{in}= 0.47 $\pm$0.07		
2001 - 12 - 07 (2895)	ACIS	98	6.7	α= 0.5,	33/30	15.2 $\pm$1.2
				T_{in}= 0.57 $\pm$0.03		
2002 - 01 - 06 (0112570101)	PN	130	6.7	Γ= 1.8 $\pm$0.1	316/309	3.2 $\pm$1.1
				T_{in}= 0.24 $\pm$0.004		
2002 - 01 - 08 (2897)	ACIS	132	6.7	Γ= 2.57$\pm$0.19	13.3/13	3.3 $\pm$0.3
2002 - 02 - 06 (2896)	ACIS	-	6.7	Γ= 1.7	–	< 0.06
SWIFT J004320.5+411528						
Date (ObsId)	Inst.[a]	T[b]	$N_H(10^{20})$	fit parameters	χ^2/dof	L[c] ($\times 10^{37}$)
2008 - 07 - 18 (0560180101)	PN	-	6.8		–	$<$0.08
2008 - 08 - 21 (00031255001)	XRT	-7	6.8 $\pm$2.8	T_{in}= 0.57 $\pm$0.05	18.1/18	18.2 $\pm$1.6
2008 - 08 - 28 (00031255002)	XRT	0	6.8	T_{in}= 0.59 $\pm$0.06	13.8/10	26.2 $\pm$2.0
2008 - 09 - 01 (9523)	ACIS	4	6.8	T_{in}= 0.69 $\pm$0.02	51.7/47	22.3 $\pm$0.7
2008 - 09 - 04 (00031255003)	XRT	7	6.7 $\pm$4.1	T_{in}= 0.72 $\pm$0.09	13.9/19	24.7 $\pm$2.6
2008 - 09 - 06 (00031255004)	XRT	9	6.8	T_{in}= 0.69 $\pm$0.04	15.1/17	22.8 $\pm$1.7
2008 - 09 - 11 (00031255005)	XRT	14	6.8	T_{in}= 0.68 $\pm$0.04	13.6/22	24.1 $\pm$1.2
2008 - 09 - 25 (00031255006)	XRT	28	6.8	T_{in}= 0.64 $\pm$0.06	9.14/11	17.7 $\pm$1.2
2008 - 10 - 13 (9524)	ACIS	46	6.8	T_{in}= 0.54 $\pm$0.02	29.7/28	12.7 $\pm$0.5
2008 - 10 - 14 (00031255008)	XRT	47	6.8	T_{in}= 0.50 $\pm$0.05	5.3/9	13.3 $\pm$1.5
2008 - 10 - 15 (0031255009)	XRT	48	6.8	T_{in}= 0.44 $\pm$0.04	11.7/9	11.8 $\pm$1.3
2008 - 10 - 21 (0003125010)	XRT	54	6.8	T_{in}= 0.48 $\pm$0.05	21/20	9.7 $\pm$1.0
2008 - 11 - 27 (9521)	ACIS	-	6.8	Γ= 1.7	–	< 0.22

[a] X-ray detector.

[b] Time according to X-axis in the light curves shown Fig. 5.2.

[c] Best fit parameters from XSPEC. Γ and T_{in}(in KeV) are for power index from a power law model and the temperature at the inner disc radius in the **diskbb** model, respectively. α is the grade morphing parameter in **pileup** model.

[d] Unabsorbed luminosity in energy band 0.2-10.0 keV. Assumed distance is 780 kpc.

Table 5.2: *Best spectral fit results. Parameters without uncertainty are frozen.*

6

Conclusion & Future Work

In the first part of this thesis, we traced the early history of X-ray astronomy, and discussed how it led to several discoveries, particularly accreting compact objects in our Galaxy. We discussed the basic Physics involved in this process, followed by the details of the three X-ray observatories whose data were used in this thesis (Chandra, XMM-Newton and Swift) and the data analysis involved.

The second part of this thesis presents our new scientific results:

Chapter 4: Summary and Outlook

We started this Chapter with a discussion of the detection of X-ray Binaries (XRBs) in extragalactic systems, focusing on transients in M31. The advantages of studying such binaries include the fact that the bulge of M31 can be observed in a single pointing, the column towards M31 is relatively low, and that M31 has a well known distance: the last two points facilitate an accurate determination of the X-ray luminosity down to the lowest energies.

The monthly monitoring of M31 carried out by Chandra over the last 10 years has revealed many bright X-ray transients, most of which are likely to harbor black holes (based on the population of similar transients in our own Galaxy). In addition to quantifying this population of extra-galactic XRB, we also discussed the usefulness of constraining their orbital period distribution. For example, Voss & Gilfanov (2007) has suggested that dynamical interactions in the bulge of M31 should result in a population of XRBs with orbital periods systematically shorter than those observed in our Galaxy: such an effect has already been observed in Galactic globular clusters, for example. However, the direct measurement of orbital periods for source in M31 is difficult, due to the relatively low fluxes of these systems: we discussed instead an indirect technique, first proposed by van Paradijs & McClintock (1994), which combines simultaneous measurements in the optical and X-ray to constrain the orbital period (Porb).

We applied this technique to the brightest known M31 X-ray transient, r2-75. We monitored the X-ray light curve of the outburst using Chandra and Swift, and performed the astrometry required to allow optical follow up of the field using HST: this resulted in the detection of an optical counterpart. Using an updated version of the van Paradijs & McClintock (1994) relation (specific to black hole XRBs in the high soft state: Moss et al 2013 submitted) we constrained Porb to be 15^{+6}_{-4} hrs. The X-ray light curve consists of an exponential, followed by a linear decay: this is consistent with an accretion disk transitioning from a strongly irradiated, to weakly irradiated regime. Finally, we discussed the results of Barnard et al. (2012) who carried out this analysis on a sample of M31 transients. Their results provide some support for the prediction of van Paradijs & McClintock (1994), although with limited significance due to the relatively small sample size. Clearly, an improved orbital period distribution measurement will require a significantly increased sample: this may be feasible if Chandra continues its monitoring program over the next 10 years or more. We note that, with a 5-10 ks exposure per observation, this program is not particularly costly in overall exposure time.

A significant problem we encountered, however, was the effect of pileup during the early, bright, stages of the outburst of r2-75. This is particularly frustrating, as these data have the potential to give us the highest S/N. There appears to be little that can be done to mitigate against this for future observations: we saw how that, even using the reduced ACIS exposure time, pileup will still be a problem for sources as luminous as r2-75.

More frequent observations, if possible, would better sample the X-ray light curves of M31 tran-

sients: this would minimize the time difference between the L_x and M_v measurements, and hence reduce the possibility of significant source variability between the HST and Chandra observations: this would result in a more reliable estimate of Porb.

Most of the HST observations discussed in Barnard et al. (2012) yielded upper limits only to the optical counterparts in outburst, which in turn yielded only upper limits to Porb. Clearly, deeper HST observations would, at the very least, reduce the M_v upper limit even further, and help differentiate between the M31 vs Galactic orbital period distribution. We note too that more work needs to be done in refining the van Paradijs & McClintock (1994) relation. For example, Moss et al (2013, submitted) has performed this analysis for black holes in the hard soft state in the 0.5-10 keV band (which is more appropriate for X-ray imaging observations).

In the more distant future, work similar to that discussed here may be done with the successors to the current orbiting X-ray and optical observatories e.g. Athena (assuming eventual launch) and the James Webb Space Telescope (JWST). Athena is expected to have an angular resolution some ∼10 times that of Chandra, which will significantly limit its usefulness for carrying out the kind of accurate astrometry required for follow up observations of new M31 transients. On the other hand, if Athena has a high countrate capability, then pileup should be much less of an issue for the brighter transients. JWST will work in the IR, but reach considerably fainter fluxes than HST. Nonetheless, using the NIRCAM imaging Exposure Time Calculator[1], it is clear that even the JWST will struggle to match the current upper limits given in, for example, Barnard et al. (2012). This is because we expect a typical V-K colour (where K is the magnitude at a wavelength of 2.2 microns) of ∼-1.0 for luminous XRBs. It is possible that the JWST could detect the transients in their quiescent state, which could provide an alternative route to measuring Porb. For example, for a Sun-like star in an XRB, MK∼3.3, K∼28, which is quite feasible with the JWST. However, the angular resolution of the JWST is comparable to the HST, so the field will be very crowded, hindering accurate photometry.

We conclude that the present combination of Chandra and HST is optimum for the discovery of more M31 XRB transients, and is unlikely to be surpassed by the capabilities of upcoming missions.

Chapter 5: Summary and Outlook

In this Chapter we expanded on the X-ray analysis given in Chapter 4, and presented the light

[1] http://jwstetc.stsci.edu/etc/input/nircam/imaging/

curves of a sample of bright XRBs in M31. The purpose of this work was specifically to text the model of King and Ritter (1998: hereafter KR98) for the evolution of the X-ray light curves of X-ray transients. The model predicts either an exponential or linear decay for the light curves, depending on the degree of irradiation of the accretion disk. An important advantage of testing this model for the M31 sources is that their X-ray luminosity is accurately known, in contrast to many similar transients in our own Galaxy.

This Chapter started with a theoretical discussion of the expected light curve behavior, and followed with the observational data (obtained from Chandra, XMM-Newton and Swift) for comparison.

The transients used in the sample were selected on the basis of their bright outburst luminosity, and hence were each expected to show an initial exponential decay on the basis of the KR98 model. However, only two showed such an effect: the others were more consistent with a linear decay, suggesting a relatively weakly irradiated disk, in contrast to the observed X-ray luminosity. This suggests that the KR98 result (based on an α-accretion disk model) is too simple, and should be expanded to incorporate, for example, an ADAF. Clearly, however, the dataset should be expanded. This would involve increasing both the number of sources, and the sampling of their light curves. The latter is important because sparse sampling may result in important behavior being overlooked (such as an exponential early phase). In addition, greater sampling will allow us place better constraints on where the state changes occur (e.g. high-soft to low-hard), as a function of L_x. All of these issues will be gradually addressed over time as M31 continues to be monitored by Chandra, XMM-Newton and Swift.

We note too that combining these light curves with optical observations will again allow us constrain Porb, and from this the size of the accretion disk, which will be useful for comparison with models: this has already been discussed by Barnard et al. (2012). Finally, it would be timely to update the work of Chen et al. (1997) on Galactic transients, for comparison with the increasing extragalactic sample. In the more distant future, observations with a mission such as Athena will offer dramatic improvements over what is achievable today. Athena would allow us monitor the spectral and temporal evolution of the light curve with much greater accuracy than current missions (e.g. monitor the day to fluxes < 10 times fainter than currently possible). This would allow a much more detailed comparison with Galactic transients.

Appendices

A

Python Scripts for Analysing X-Ray Data

A.1 Python - CIAO Script to Extract Spectrum

This script is written to work with **CIAO 4.4** and **CALDB 4.4.7.**. It asks the user to enter the full path directory of the data. Using **specextract** [1] task in CIAO, the script extracts spectrum of a point source.

```
#! /usr/bin/env python
import os
from ciao_contrib.runtool  import *

if (os.path.exists('acis_evt2.fits') == False):
    indir = raw_input("Entre the full folder address  of data= ")
```

[1] http://cxc.harvard.edu/ciao/ahelp/specextract.html

```
    os.system('cp  ' + indir+'/*_evt2.fits  . ')
    os.system('mv *_evt2.fits  acis_evt2.fits' )
    os.system('cp  ' + indir+'/*_msk1.fits  . ')
    os.system('mv *_msk1.fits acis_msk1.fits'  )
    os.system('cp  ' + indir+'/*_asol1.fits  .')
    os.system('mv *_asol1.fits pcad_asol1.fits')
    os.system('cp  ' + indir+'/*_bpix1.fits  .')
    os.system('mv *_bpix1.fits  acis_bpix1.fits')
    os.system('cp  ' + indir+'/*_pbk0.fits   .')
    os.system('mv *_pbk0.fits acis_pbk0.fits ')



if (os.path.exists('source.reg') == False):
    print "Select the source."
    os.system('ds9 acis_evt2.fits -log -minmax  ')

if (os.path.exists('back.reg') == False):
    print "Select the background region."
    os.system('ds9 acis_evt2.fits -log -minmax ')
#- Run psectract -
specextract.punlearn()
specextract.infile = "acis_evt2.fits[sky=region(source.reg)]"
specextract.outroot = 'spec'
specextract.bkgfile = "acis_evt2.fits[sky=region(back.reg)]"
specextract.weight  = False
specextract.correct = True
specextract.asp     = "pcad_asol1.fits"
specextract.mskfile = "acis_msk1.fits"
specextract.badpixfile = "acis_bpix1.fits"
specextract.pbkfile = "acis_pbk0.fits"
specextract.grouptype = 'NUM_CTS'
```

```
specextract.binspec = 20
specextract(verbose = 2 )
```

A.2 Python - SAS Script

This script is written to work with **SAS 11.0.0**. After starting SAS with the following commands

```
> setenv SAS_DIR /some_dir/xmmsas_20100423_1801
> source '/usr/local/xmmsas11/xmmsas_20110223_1801/setsas.csh'
```

user can run the below script to reduce XMM-newton data.

```
#!/usr/bin/env python
import os
import glob
#- Setting the calibration files -
os.environ['SAS_CCFPATH'] = '/usr/local/ccf'
#- The Observation Data Files -
os.environ['SAS_ODF'] = os.getcwd()
#- execute cifbuild -
if (os.path.exists('ccf.cif')== False):
  os.system('cifbuild')
#
os.environ['SAS_CCF'] = 'ccf.cif'
datafile = glob.glob("*.SAS")
if (len(datafile) ==0 ):
     os.system('odfingest')
datafile = glob.glob("*.SAS")
os.environ['SAS_ODF'] = datafile[0]
#- Generate calibrated and concatenated EPIC events list -
dsFiles = glob.glob("*_ImagingEvts.ds")
if (len(dsFiles)== 0 ):
    os.system('emproc >& PN.log ')
    os.system('epproc >& MOS.log')
```

```
#- Filter EPIC event list for flaring partile background -
#***  EPIC-MOS1 ***
if (os.path.exists('rateMOS1.fits') and os.path.exists('EPICgti_MOS1.fits') and\
    os.path.exists('EPICclean_MOS1.fits')):
    print "Script message(1a) : Cleaned data exist, EPICclean_MOS1.fits is ready"

TableDs_MOS1 = glob.glob('*_EMOS1_*_ImagingEvts.ds')
ExpMOS_1  = "'#XMMEA_EM && (PI>10000) && (PATTERN==0)'"
ExpTab    = "'RATE<=0.35'"
ExpMOS1_2 = "'#XMMEA_EM && gti(EPICgti_MOS1.fits,TIME) && (PI>150)'"
if (os.path.exists ('rateMOS1.fits') == False):
    os.system('evselect table='+TableDs_MOS1[0]+' withrateset=Y\
               rateset=rateMOS1.fits  maketimecolumn=Y timebinsize=100\
               makeratecolumn=Y expression='+ExpMOS_1)
if (os.path.exists ('EPICgti_MOS1.fits') == False):
    os.system('tabgtigen table=rateMOS1.fits expression='+ExpTab +\
              ' gtiset=EPICgti_MOS1.fits')
if (os.path.exists ('EPICclean_MOS1.fits') == False):
    os.system('evselect table='+TableDs_MOS1[0]+' withrateset=Y\
               filteredset=EPICclean_MOS1.fits  destruct=Y keepfilteroutput=T\
                expression='+ExpMOS1_2)
#*** EPIC-MOS2 ***
if (os.path.exists('rateMOS2.fits') and os.path.exists('EPICgti_MOS2.fits') and\
    os.path.exists('EPICclean_MOS2.fits')):
    print "Script message(1b) : Cleaned data exist, EPICclean_MOS2.fits is ready"

TableDs_MOS2 = glob.glob('*_EMOS2_*_ImagingEvts.ds')
ExpMOS2_2 = "'#XMMEA_EM && gti(EPICgti_MOS2.fits,TIME) && (PI>150)'"
if (os.path.exists('rateMOS2.fits') == False):
    os.system('evselect table='+TableDs_MOS2[0]+' withrateset=Y \
               rateset=rateMOS2.fits  maketimecolumn=Y\
```

```
                timebinsize=100 makeratecolumn=Y  expression='+ExpMOS_1)
if (os.path.exists('EPICgti_MOS2.fits') == False) :
    os.system('tabgtigen table=rateMOS2.fits expression='+ExpTab\
              +'  gtiset=EPICgti_MOS2.fits')
if (os.path.exists('EPICclean_MOS2.fits') == False) :
    os.system('evselect table='+TableDs_MOS2[0]+' withrateset=Y\
                filteredset=EPICclean_MOS2.fits  destruct=Y\
                keepfilteroutput=T  expression='+ExpMOS2_2)
##**** EPIC-PN ***
if (os.path.exists('ratePN.fits') and os.path.exists('EPICgti_PN.fits') and\
    os.path.exists('EPICclean_PN.fits')):
    print "Script message(1c) : Cleaned data exist, EPICclean_MOS1.fits is ready"

TableDs_PN = glob.glob('*_EPN_*_ImagingEvts.ds')
ExpPn_1    = "'#XMMEA_EP && (PI>10000&&PI<12000) && (PATTERN==0)'"
ExpTab_PN = "'RATE<=0.4'"
ExpPn_2    = "'#XMMEA_EP && gti(EPICgti_PN.fits,TIME) && (PI>150)'"
if (os.path.exists('ratePN.fits') == False) :
    os.system('evselect table='+TableDs_PN[0]+' withrateset=Y\
                rateset=ratePN.fits maketimecolumn=Y timebinsize=100\
                makeratecolumn=Y expression='+ExpPn_1)
if (os.path.exists('EPICgti_PN.fits') == False ):
    os.system('tabgtigen table=ratePN.fits expression='+ExpTab_PN+\
              ' gtiset=EPICgti_PN.fits')
if (os.path.exists('EPICclean_PN.fits') == False):
    os.system('evselect table='+TableDs_PN[0]+' withrateset=Y\
              filteredset=EPICclean_PN.fits  destruct=Y\
              keepfilteroutput=T expression='+ExpPn_2)
```

A.2.1 Extract the Spectrum from PN Data

This script extracts spectrum of a point source in PN.

```
#!/usr/bin/env python
import os
import glob    # use to ls
#- Extract MOS point-like source spectrum  -
if (os.path.exists('PN_image.fits') == False):
    os.system('evselect table=EPICclean_PN.fits imagebinning=binSize\
               imageset=PN_image.fits withimageset=yes xcolumn=X\
               ycolumn=Y ximagebinsize=80 yimagebinsize=80')
#- extract source spectrum -
if (os.path.exists('source_PN.reg')==False or os.path.exists('back_PN.reg')==False):
    os.system('ds9 PN_image.fits -scale log')

FIN   = open('source_PN.reg', 'r')
lines = FIN.readlines()
for line in lines:
    if (line.find('circle') >= 0):
        reg = line.strip()
ExpPN = "'(FLAG==0) && (PATTERN<=4) && ((X,Y) IN "+reg+")'"
if (os.path.exists('PN_source_spectrum.fits')== False):
    os.system('evselect table=EPICclean_PN.fits withspectrumset=yes\
               spectrumset=PN_source_spectrum.fits energycolumn=PI\
               spectralbinsize=5 withspecranges=yes specchannelmin=0\
               specchannelmax=20479 expression='+ExpPN)
#- extract background spectrum -
FIN   = open('back_PN.reg', 'r')
lines = FIN.readlines()
for line in lines:
     if (line.find('circle') >= 0):
        reg_back = line.strip()
ExpPN2 = "'(FLAG==0) && (PATTERN<=4) && ((X,Y) IN "+reg_back+")'"
if (os.path.exists('PN_background_spectrum.fits') == False):
```

```
    os.system('evselect table=EPICclean_PN.fits withspectrumset=yes\
               spectrumset=PN_background_spectrum.fits energycolumn=PI\
               spectralbinsize=5 withspecranges=yes specchannelmin=0\
               specchannelmax=20479 expression='+ExpPN2)
#-Calculate the area of source and background region -
os.system('backscale spectrumset=PN_source_spectrum.fits\
          badpixlocation=EPICclean_PN.fits')
os.system('backscale spectrumset=PN_background_spectrum.fits\
          badpixlocation=EPICclean_PN.fits')
#- Generate rmf file-
if (os.path.exists('PN.rmf')== False):
    os.system('rmfgen spectrumset=PN_source_spectrum.fits rmfset=PN.rmf')
#- Generate arf file
if (os.path.exists('PN.arf')== False):
    os.system('arfgen spectrumset=PN_source_spectrum.fits arfset=PN.arf\
               withrmfset=yes rmfset=PN.rmf badpixlocation=EPICclean_PN.fits\
               detmaptype=psf')
#- Rebin the spectrum -
if (os.path.exists('spectrum_PN.pi') == False):
    os.system('grppha  infile=PN_source_spectrum.fits  outfile=spectrum_PN.pi\
                       comm ="\
                       chkey backfile PN_background_spectrum.fits &\
                       chkey ancrfile PN.arf &\
                       chkey respfile PN.rmf &\
                       group min 20 &\
                       show grouping &\
                       exit" ')
```

A.3 Python Script for SWIFT Data

Using **HEASOFT 6.11**, these scripts can be used to reduce SWIFT data. To use the latest CALDB Swift files, all data was reprocessed with **xrtpipeline v0.12.6** along with producing

exposure maps. Using **XSELECT 2.4b**, spectra of the sources and backgrounds were extracted from a circle using the radius recommended by the Swift team, 20 pixel (=47 arcsec, 1 XRT pixel = 2.36 arcsec) for the source and 30 pixel (=70 arcsec) for the background. The appropriate RMF for each source is selected from the calibration data base and the ARFs were generated with xrtmkarf.

A.3.1 Extract an Image

To generate an image from XRT data, the commands in the box below must be saved in a text file named **image.xco**.

```
image
read event
out-xrt/
sw00031518013xpcw3po_cl.evt
yes
extract image
save image image_tot.im
filter pha_cutoff 20 100
extract image
save image 0.2-1keV.im
clear pha_cutoff
filter pha_cutoff 100 200
extract image
save image 1-2keV.im
clear pha_cutoff
filter pha_cutoff 200 1000
extract image
save im 2-10keV.im
quit
no
```

Then, running the python script below generates images in three different wavebands: 0.2-1 keV, 1-2 keV and 2-10 keV.

```
#!/usr/bin/env python
import os
import glob
#
os.chdir('out-xrt/')
obs_evt = glob.glob('*po_cl.evt')
obs_evt = obs_evt[0]
#
os.chdir('../')
fin = open("image.xco", 'r')
img_lines = fin.readlines()
fin.close()

img_lines.pop(3)
img_lines.insert(3, obs_evt + '\n')

fout = open("image_source.xco", 'w')
for i in range(len(img_lines)):
  print >>fout, img_lines[i],
fout.close()
# extract a total image and three images in three wavebands -
if (os.path.exists ('image_tot.im') == False):
    os.system('xselect @image_source.xco')
```

A.3.2 Extract Spectrum

To extract the spectrum of a point source, this script needs a **spectrum.xco** and the below script:

```
spectrum
read event
out-xrt/
sw00031518013xpcw3po_cl.evt
yes
```

```
filter region source.reg
extract spectrum
save spectrum source.pi
clear region
filter region back.reg
extract spectrum
save spectrum source-back.pi
quit
no
```

Then, running this script extracts spectrum of a point source from the XRT image.

```
#!/usr/bin/env python

import os
import glob

os.chdir('out-xrt/')
obs_evt = glob.glob('*po_cl.evt')
obs_evt = obs_evt[0]
exp = glob.glob('*pc*_ex.img')
exp = exp[0]
os.system('cp  ' + exp  +' ../')
os.chdir('../')
#-extracting spectrum ----------------------------------------------------
# Chose the source region, (recommended radius = 47'')-
if (os.path.exists ('source.reg') == False):
    print "Choose the source region."
    os.system ('ds9  image_tot.im -log -minmax ')
# Choose the back region
if (os.path.exists ('back.reg') == False):
    print "Choose the background region."
```

```
    os.system ('ds9  image_tot.im -log -minmax ')
#
fin = open("spectrum.xco", 'r')
img_lines = fin.readlines()
fin.close()

img_lines.pop(3)
img_lines.insert(3, obs_evt + '\n')

fout = open("spectrum_source.xco", 'w')
for i in range(len(img_lines)):
  print >>fout, img_lines[i],
fout.close()

if( os.path.exists('source.pi') == False ):
    os.system('xselect @spectrum_source.xco')
#- producing arf file-
if (os.path.exists ('source.arf') == False):
    os.system('xrtmkarf expofile='+exp +' PSF correction= yes  phafile = source.pi\
                outfile = source.arf  srcx=-1 srcy=-1 psfflag=yes')
    # psfflag: 'yes', correct for the PSF for point-like sources.
#-copying  rmf file-
rmf = glob.glob('*.rmf')
if (len(rmf) == 0):
  RmfLink = raw_input('Copy the link of rmf here ==')
  os.system('cp '+ RmfLink + ' .')
rmf= glob.glob('*.rmf')
rmf= rmf[0]
#-Using grppha to group -
if (os.path.exists('source_grp.pi') == False):
    os.system('grppha  infile=source.pi  outfile=source_grp.pi\
```

```
comm =" \
bad 0-29 && group min 20 &&\
chkey backfile source-back.pi &&\
chkey ancrfile source.arf &&\
chkey respfile ' + rmf+ ' &&\
exit" clobber=yes')
```

B

PyXspec script

Using **XSPEC 12.7.0.**, this sample script loads pi, RMF and ARF files and fit disk black body model to the data. Using **cflux**[1] in the script, provides user the unabsorbed flux. The script calculates luminosity of a source in M31 (assumed distance is 780 kpc) and prints on the screen.

```
#!/usr/bin/python

from xspec import *
import math
#
#- Loading data-
AllData += "spec_grp.pi"
```

[1] http://heasarc.gsfc.nasa.gov/xanadu/xspec/manual/XSmodelCflux.html

```
#- Defining a model -
m = Model("phabs*cflux*diskbb")          # absorbed disk blackbody model
m.phabs.nH = 0.06
m.phabs.nH.frozen = True
#
m.cflux.Emin = 0.2
m.cflux.Emax = 10.0
#
m.diskbb.norm.frozen = True
#- Fitting a model -
AllData.ignore("bad")
AllData.ignore("**-0.2 10.0-**")
#
Fit.statMethod = "chi"
Fit.nIterations = 100
Fit.renorm()
Fit.perform()
#-Results -
Tin     = m.diskbb.Tin.values[0]
Tin_err = m.diskbb.Tin.sigma
print "Tin= ", '%0.2f'%Tin, "+-", '%0.2f'%Tin_err
#
F_log10_unabs = m.cflux.lg10Flux.values[0]
F_unabs       = math.pow(10, F_log10_unabs)
#
F_log10_up    = m.cflux.lg10Flux.sigma + F_log10_unabs
F_unabs_up    = math.pow(10, F_log10_up)
#- Converting flux to luminosity-
def L(f):
  pi = 3.1415
  d = 780       # kpc, distance to M31
```

```
  kpc_to_cm = 3.08E+21
  L = 4 * pi* math.pow(d * kpc_to_cm, 2.0) * f
  return L
print "L_unabsorbed =", '%0.3e'%L(F_unabs) , " (erg/s)"
```

C

Python-IRAF script

This script subtract two images arithmetically (see page 59 for explanation). The first panel from right in Fig. 4.3 has been produced using this script.

```
#! /usr/bin/env python
from pyraf import iraf
import pyfits              # load FITS module.
import os                  # load linux commands in python.
#
image1 = 'on-HST.fits'
image2 = 'off-HST.fits'
# load IRAF packages -
iraf.images(_doprint=0)
```

```
iraf.immatch(_doprint=0)
iraf.imutil
#- Run  wcxymatch
f1  = pyfits.open(image1)
scidata1 = f1['SCI'].data

f2 = pyfits.open(image2)
scidata2 = f2['SCI'].data

if( os.path.exists('list.txt') ): os.remove('list.txt')
iraf.unlearn(iraf.wcsxymatch)
iraf.wcsxymatch(input=image1+'[1]', reference= image2+'[1]', output='list.txt'\
                , verbose = 'no' )
#- Running  geomap-
x_m = f2[1].header['NAXIS1']
y_m = f2[1].header['NAXIS2']

iraf.unlearn(iraf.geomap)
if( os.path.exists('data') ):
    os.remove('data')
iraf.geomap(input='list.txt',database='data', xmin= 1, xmax= x_m, ymin= 1\
            ymax= y_m, verbose = 'no')
#- Run Geotran -
iraf.unlearn(iraf.geotran)
if( os.path.exists('shift.fits') ):
    os.remove('shift.fits')
iraf.geotran(input= image1+'[1]',  output='shift.fits', database='data',\
             transforms ='list.txt' )
# subtraction -
iraf.unlearn(iraf.imarith)
if( os.path.exists('resid.fits') ):
```

```
    os.remove('resid.fits')
iraf.imarith(operand1=image2+'[1]', op='-', operand2='shift.fits'\
             , result='resid.fits')
```

Bibliography

Abramowicz, M. A., Czerny, B., Lasota, J. P., & Szuszkiewicz, E. 1988, ApJ, 332, 646

Anderson, S. F., Margon, B., Deutsch, E. W., & Downes, R. A. 1993, AJ, 106, 1049

Arnaud, K. A. 1996, in Astronomical Society of the Pacific Conference Series, Vol. 101, Astronomical Data Analysis Software and Systems V, ed. G. H. Jacoby & J. Barnes, 17

Barnard, R., Galache, J. L., Garcia, M. R., et al. 2012, ApJ, 756, 32

Barnard, R., Garcia, M., Murray, S., Nooraee, N., & Pietsch, W. 2011, A&A, 526, A50+

Beaton, R. L., Majewski, S. R., Guhathakurta, P., et al. 2007, ApJ, 658, L91

Begelman, M. C. 1979, MNRAS, 187, 237

Bolton, C. T. 1972, Nature, 235, 271

Bowyer, S., Margon, B., Lampton, M., & Cruddace, R. 1974, ApJ, 190, 285

Cannizzo, J. K. 1993, The Limit Cycle Instability in Dwarf Nova Accretion Disks, ed. J. C. Wheeler, 6

Cardelli, J. A., Clayton, G. C., & Mathis, J. S. 1989, ApJ, 345, 245

Cash, W. 1979, ApJ, 228, 939

Charles, P. A. & Coe, M. J. 2006, Optical, ultraviolet and infrared observations of X-ray binaries, ed. Lewin, W. H. G. & van der Klis, M., 215–265

Chen, W., Shrader, C. R., & Livio, M. 1997, ApJ, 491, 312

Chevalier, C., Ilovaisky, S. A., & Charles, P. A. 1985, A&A, 147, L3

Coe, M. J., Engel, A. R., & Quenby, J. J. 1976, Nature, 259, 544

Corbel, S., Fender, R. P., Tzioumis, A. K., et al. 2000, A&A, 359, 251

Coriat, M., Fender, R. P., & Dubus, G. 2012, ArXiv e-prints

Crampton, D., Hutchings, J. B., Cowley, A. P., Schade, D. J., & van Speybroeck, L. P. 1984, ApJ, 284, 663

Davis, J. E. 2001, ApJ, 562, 575

Davis, S. W. & Hubeny, I. 2006, ApJS, 164, 530

Di Stefano, R., Kong, A. K. H., Greiner, J., et al. 2004, ApJ, 610, 247

Dubus, G., Lasota, J.-P., Hameury, J.-M., & Charles, P. 1999, MNRAS, 303, 139

Eardley, D. M. & Lightman, A. P. 1975, ApJ, 200, 187

Elvis, M., Page, C. G., Pounds, K. A., Ricketts, M. J., & Turner, M. J. L. 1975, Nature, 257, 656

Esin, A. A., McClintock, J. E., Drake, J. J., et al. 2001, ApJ, 555, 483

Esin, A. A., McClintock, J. E., & Narayan, R. 1997, ApJ, 489, 865

Evans, W. D., Belian, R. D., & Conner, J. P. 1970, ApJ, 159, L57

Fender, R. & Belloni, T. 2004, ARA&A, 42, 317

Fender, R. P. 2001, MNRAS, 322, 31

Fender, R. P., Belloni, T. M., & Gallo, E. 2004, MNRAS, 355, 1105

Francey, R. J. & Fenton, A. G. 1967, Nature, 216, 773

Frank, J., King, A., & Raine, D. 1992, Accretion power in astrophysics., ed. Frank, J., King, A., & Raine, D.

Frontera, F., Zdziarski, A. A., Amati, L., et al. 2001, ApJ, 561, 1006

Fruscione, A., McDowell, J. C., Allen, G. E., et al. 2006, in Society of Photo-Optical Instrumentation Engineers (SPIE) Conference Series, Vol. 6270, Society of Photo-Optical Instrumentation Engineers (SPIE) Conference Series

Galache, J. L., Garcia, M. R., Torres, M. A. P., et al. 2006, The Astronomer's Telegram, 969, 1

Galleti, S., Federici, L., Bellazzini, M., Fusi Pecci, F., & Macrina, S. 2004, A&A, 416, 917

Gallo, E., Fender, R. P., & Hynes, R. I. 2005, MNRAS, 356, 1017

Gallo, E., Fender, R. P., Miller-Jones, J. C. A., et al. 2006, MNRAS, 370, 1351

Garcia, M. R., Murray, S. S., Primini, F. A., et al. 2000, ApJ, 537, L23

Giacconi, R., Gursky, H., Kellogg, E., Schreier, E., & Tananbaum, H. 1971, ApJ, 167, L67

Giacconi, R., Gursky, H., Paolini, F. R., & Rossi, B. B. 1962, Physical Review Letters, 9, 439

Giacconi, R., Murray, S., Gursky, H., et al. 1974, ApJS, 27, 37

Gierliński, M., Zdziarski, A. A., Poutanen, J., et al. 1999, MNRAS, 309, 496

Grimm, H., Gilfanov, M., & Sunyaev, R. 2002, A&A, 391, 923

Grove, J. E., Johnson, W. N., Kroeger, R. A., et al. 1998, ApJ, 500, 899

Haberl, F., Pietsch, W., Greiner, J., & Ajello, M. 2006, The Astronomer's Telegram, 881, 1

Harries, J. R. & McCracken, K. G. 1967, Nature, 215, 38

Hasinger, G. & van der Klis, M. 1989, A&A, 225, 79

Hellier, C. 2001, Cataclysmic Variable Stars, ed. Hellier, C.

Henze, M., Pietsch, W., Haberl, F., & Greiner, J. 2009, The Astronomer's Telegram, 2356, 1

Hirano, A., Kitamoto, S., Yamada, T. T., Mineshige, S., & Fukue, J. 1995, ApJ, 446, 350

Holland, S. 1998, AJ, 115, 1916

Igumenshchev, I. V. & Abramowicz, M. A. 2000, ApJS, 130, 463

Igumenshchev, I. V., Abramowicz, M. A., & Narayan, R. 2000, ApJ, 537, L27

Kaur, A., Henze, M., Haberl, F., et al. 2012, A&A, 538, A49

King, A. R., Pringle, J. E., & Livio, M. 2007, MNRAS, 376, 1740

King, A. R. & Ritter, H. 1998, MNRAS, 293, L42

Kippenhahn, R. & Weigert, A. 1967, ZAp, 65, 251

Kolb, U. 2010, Extreme Environment Astrophysics

Kong, A., Garcia, M., Murray, S., et al. 2001, The Astronomer's Telegram, 76, 1

Kong, A. K. H., Garcia, M. R., Primini, F. A., et al. 2002, ApJ, 577, 738

Kubota, A., Ebisawa, K., Makishima, K., & Nakazawa, K. 2005, ApJ, 631, 1062

Kubota, A. & Makishima, K. 2004, ApJ, 601, 428

Lasota, J.-P. 2001, New A Rev., 45, 449

Lasota, J.-P. & Hameury, J.-M. 1998, in American Institute of Physics Conference Series, Vol. 431, American Institute of Physics Conference Series, ed. S. S. Holt & T. R. Kallman, 351–360

Li, L.-X., Zimmerman, E. R., Narayan, R., & McClintock, J. E. 2005, ApJS, 157, 335

Liu, Q. Z., van Paradijs, J., & van den Heuvel, E. P. J. 2001, A&A, 368, 1021

Lüst, R. 1952, Zeitschrift Naturforschung Teil A, 7, 87

Lynden-Bell, D. & Pringle, J. E. 1974, MNRAS, 168, 603

Makishima, K., Maejima, Y., Mitsuda, K., et al. 1986, ApJ, 308, 635

Markoff, S., Falcke, H., & Fender, R. 2001, A&A, 372, L25

Massey, P., Olsen, K. A. G., Hodge, P. W., et al. 2006, AJ, 131, 2478

Mattei, J. A., Saladyga, M., & Waagen, E. O. 1985, SS Cygni light curves 1896-1985

McClintock, J. E., Haswell, C. A., Garcia, M. R., et al. 2001, ApJ, 555, 477

McClintock, J. E. & Remillard, R. A. 1986, ApJ, 308, 110

McClintock, J. E. & Remillard, R. A. 2006, Black hole binaries, ed. W. H. G. Lewin & M. van der Klis, 157–213

Middleton, M. J., Sutton, A. D., Roberts, T. P., Jackson, F. E., & Done, C. 2012, MNRAS, 420, 2969

Miller, J. M., Homan, J., & Miniutti, G. 2006, ApJ, 652, L113

Mineshige, S., Hirano, A., Kitamoto, S., Yamada, T. T., & Fukue, J. 1994, ApJ, 426, 308

Mitsuda, K., Inoue, H., Koyama, K., et al. 1984, PASJ, 36, 741

Moretti, A., Campana, S., Mineo, T., et al. 2005, in Presented at the Society of Photo-Optical Instrumentation Engineers (SPIE) Conference, Vol. 5898, Society of Photo-Optical Instrumentation Engineers (SPIE) Conference Series, ed. O. H. W. Siegmund, 360–368

Morris, M. & Serabyn, E. 1996, ARA&A, 34, 645

Narayan, R. 1996, ApJ, 462, 136

Narayan, R., Barret, D., & McClintock, J. E. 1997a, ApJ, 482, 448

Narayan, R., Garcia, M. R., & McClintock, J. E. 1997b, ApJ, 478, L79

Narayan, R. & McClintock, J. E. 2008, New A Rev., 51, 733

Narayan, R. & Yi, I. 1994, ApJ, 428, L13

Narayan, R. & Yi, I. 1995, ApJ, 444, 231

Nieto, J.-L., Auriere, M., Sebag, J., et al. 1990, A&A, 239, 155

Nooraee, N., Callanan, P. J., Barnard, R., et al. 2012, A&A, 542, A120

Noorraee, N., Barnard, R., Pietsch, W., Callanan, P., & Garcia, M. 2010, The Astronomer's Telegram, 2682, 1

Novikov, I. D. & Thorne, K. S. 1973, in Black Holes (Les Astres Occlus), ed. C. Dewitt & B. S. Dewitt, 343–450

Paczyńsky, B. & Wiita, P. J. 1980, A&A, 88, 23

Patterson, J. & Raymond, J. C. 1985, ApJ, 292, 535

Pietsch, W., Burwitz, V., Greiner, J., Henze, M., & Stiele, H. 2008, The Astronomer's Telegram, 1674, 1

Pietsch, W., Freyberg, M., & Haberl, F. 2005, A&A, 434, 483

Predehl, P. & Schmitt, J. H. M. M. 1995, A&A, 293, 889

Primini, F. A., Forman, W., & Jones, C. 1993, ApJ, 410, 615

Pringle, J. E. & Rees, M. J. 1972, A&A, 21, 1

Reig, P. 2011, Ap&SS, 332, 1

Reis, R. C., Fabian, A. C., & Miller, J. M. 2010, MNRAS, 402, 836

Reis, R. C., Miller, J. M., & Fabian, A. C. 2009, MNRAS, 395, L52

Remillard, R. A. & McClintock, J. E. 2006a, Compact stellar X-ray Sources (Cambridge University Press)

Remillard, R. A. & McClintock, J. E. 2006b, ARA&A, 44, 49

Russell, D. M., Fender, R. P., Hynes, R. I., et al. 2006, MNRAS, 371, 1334

Rykoff, E. S., Miller, J. M., Steeghs, D., & Torres, M. A. P. 2007, ApJ, 666, 1129

Samimi, J., Share, G. H., Wood, K., et al. 1979, Nature, 278, 434

Schreier, E., Levinson, R., Gursky, H., et al. 1972, ApJ, 172, L79

Seward, F. D. & Charles, P. A. 2010, Exploring the X-ray Universe, ed. Seward, F. D. & Charles, P. A.

Shahbaz, T., Charles, P. A., & King, A. R. 1998, MNRAS, 301, 382

Shakura, N. I. & Sunyaev, R. A. 1973, A&A, 24, 337

Stanek, K. Z. & Garnavich, P. M. 1998, ApJ, 503, L131

Stella, L., White, N. E., Davelaar, J., et al. 1985, ApJ, 288, L45

Stone, J. M., Pringle, J. E., & Begelman, M. C. 1999, MNRAS, 310, 1002

Supper, R., Hasinger, G., Pietsch, W., et al. 1997, A&A, 317, 328

Takahashi, K., Inoue, H., & Dotani, T. 2001, PASJ, 53, 1171

Tanaka, Y. & Lewin, W. H. G. 1995, in X-ray Binaries, ed. W. H. G. Lewin, J. van Paradijs, & E. P. J. van den Heuvel, 126–174

Tanaka, Y. & Shibazaki, N. 1996, ARA&A, 34, 607

Tananbaum, H., Gursky, H., Kellogg, E., Giacconi, R., & Jones, C. 1972, ApJ, 177, L5

Tauris, T. M. & van den Heuvel, E. P. J. 2006, Formation and evolution of compact stellar X-ray sources, ed. W. H. G. Lewin & M. van der Klis, 623–665

Tennant, A. F., Fabian, A. C., & Shafer, R. A. 1986, MNRAS, 219, 871

Terrell, J., Priedhorsky, W. C., Davelaar, J., et al. 1983, IAU Circ., 3893, 1

Tomsick, J. A., Kalemci, E., Kaaret, P., et al. 2008, ApJ, 680, 593

Tomsick, J. A., Yamaoka, K., Corbel, S., et al. 2009, ApJ, 707, L87

Trinchieri, G. & Fabbiano, G. 1991, ApJ, 382, 82

Trudolyubov, S., Priedhorsky, W., & Cordova, F. 2006, ApJ, 645, 277

Trudolyubov, S. P., Borozdin, K. N., & Priedhorsky, W. C. 2001, ApJ, 563, L119

Truss, M. R., Wynn, G. A., Murray, J. R., & King, A. R. 2002, MNRAS, 337, 1329

van den Heuvel, E. P. J., Bhattacharya, D., Nomoto, K., & Rappaport, S. A. 1992, A&A, 262, 97

van der Klis, M., Jansen, F., van Paradijs, J., et al. 1985, Nature, 316, 225

van Paradijs, J. 1996a, ApJ, 464, L139

van Paradijs, J. 1996b, ApJ, 464, L139

van Paradijs, J. & McClintock, J. E. 1994, A&A, 290, 133

van Speybroeck, L., Epstein, A., Forman, W., et al. 1979, ApJ, 234, L45

von Weizsäcker, C. F. 1951, ApJ, 114, 165

Voss, R. & Gilfanov, M. 2007, MNRAS, 380, 1685

Voss, R., Pietsch, W., Haberl, F., et al. 2008, A&A, 489, 707

Webster, B. L. & Murdin, P. 1972, Nature, 235, 37

Wilkinson, T. & Uttley, P. 2009, MNRAS, 397, 666

Williams, B. F., Garcia, M. R., McClintock, J. E., Primini, F. A., & Murray, S. S. 2005, ApJ, 632, 1086

Williams, B. F., Naik, S., Garcia, M. R., & Callanan, P. J. 2006a, ApJ, 643, 356

Williams, B. F., Naik, S., Garcia, M. R., & Callanan, P. J. 2006b, ApJ, 643, 356

Wilms, J., Nowak, M. A., Dove, J. B., Fender, R. P., & Di Matteo, T. 1999, ApJ, 522, 460

Zimmerman, E. R., Narayan, R., McClintock, J. E., & Miller, J. M. 2005, ApJ, 618, 832